

# **Force and Conductance Spectroscopy of Single Molecule Junctions**

Michael Frei

Submitted in partial fulfillment of the  
requirements for the degree of  
Doctor of Philosophy

in the Graduate School of Arts and Sciences

COLUMBIA UNIVERSITY

2012

© 2012  
Michael Frei  
All rights reserved

## **ABSTRACT**

# **Force and Conductance Spectroscopy of Single Molecule Junctions**

Michael Frei

Investigation of mechanical properties of single molecule junctions is crucial to develop an understanding and enable control of single molecular junctions. This work presents an experimental and analytical approach that enables the statistical evaluation of force and simultaneous conductance data of metallic atomic point contacts and molecular junctions. A conductive atomic force microscope based break junction technique is developed to form single molecular junctions and collect conductance and force data simultaneously. Improvements of the optical components have been achieved through the use of a super-luminescent diode, enabling tremendous increases in force resolution. An experimental procedure to collect data for various molecular junctions has been developed and includes deposition, calibration, and analysis methods. For the statistical analysis of force, novel approaches based on two dimensional histograms and a direct force identification method are presented. The two dimensional method allows for an unbiased evaluation of force events that are identified using corresponding conductance signatures. This is not always possible however, and in these situations, the force based identification of junction rearrangement events is an attractive alternative method. This combined experimental and analytical approach is then applied to three studies: First, the impact

of molecular backbones to the mechanical behavior of single molecule junctions is investigated and it is found that junctions formed with identical linkers but different backbone structure result in junctions with varying breaking forces. All molecules used show a clear molecular signature and force data can be evaluated using the 2D method. Second, the effects of the linker group used to attach molecules to gold electrodes are investigated. A study of four alkane molecules with different linkers finds a drastic difference in the evolution of donor-acceptor and covalently bonded molecules respectively. In fact, the covalent bond is found to significantly distort the metal electrode rearrangement such that junction rearrangement events can no longer be identified with a clean and well defined conductance signature. For this case, the force based identification process is used. Third, results for break junction measurements with different metals are presented. It is found that silver and palladium junctions rupture with forces different from those of gold contacts. In the case of silver experiments in ambient conditions, we can also identify oxygen impurities in the silver contact formation process, leading to force and conductance measurements of silver-oxygen structures.

For the future, this work provides an experimental and analytical foundation that will enable insights into single molecule systems not previously accessible.

# Contents

<b>ABSTRACT.....</b>	<b>iii</b>
<b>Table of Figures.....</b>	<b>iv</b>
<b>Acknowledgments .....</b>	<b>xiii</b>
<b>Dedication .....</b>	<b>xv</b>
<b>Chapter 1 Introduction to Single Molecule Force and Conductance Measurements.....</b>	<b>1</b>
1.1 Motivation: Why Single Molecule Measurements.....	1
1.2 Theoretical Considerations: Conductance on the Single Atom Scale .....	2
1.3 Theoretical Considerations: Mechanics on the Single Atom Scale .....	4
1.4 Overview of Electrical Molecule Measurements .....	6
1.5 Atomic Force Measurement Techniques.....	7
1.6 Outlook.....	10
<b>Chapter 2 Experimental Setup .....</b>	<b>12</b>
2.1 Single Molecule Conductance Measurements using STM Break Junctions.....	12
2.2 Force and Conductance Measurement Setup .....	18
2.2a Hardware Components.....	18
2.2b Software for Experimental Control.....	21
2.3 Noise Sources and Limitations.....	23
2.4 System Upgrades.....	24
2.5 Cantilever Selection and Calibration.....	27
2.5a Cantilever Selection .....	27
2.5b Cantilever Calibration.....	29
2.6 Substrates Preparation and Molecule Deposition.....	33

2.7	Summary .....	34
<b>Chapter 3</b>	<b>Force and Conductance Data Analysis for a Gold Point Contact .....</b>	<b>36</b>
3.1	Gold Point-Contact Force and Conductance Data .....	36
3.2	Analysis of Force and Conductance.....	39
3.2a	Conductance Step Recognition and Histograms.....	39
3.2b	2D Force Analysis.....	43
3.2c	Trace-by-Trace Force Analysis.....	45
3.2d	Direct Force Event Identification.....	49
3.3	Accurate Measurements of Single Gold-Gold Bond Breaking Forces .....	50
3.4	Summary .....	52
<b>Chapter 4</b>	<b>Single Molecule Bond Rupture Forces: Influence of Molecular Backbone....</b>	<b>53</b>
4.1	Introduction and Motivation.....	53
4.2	Experimental Details .....	53
4.3	Amine and Pyridine Linked Molecules: Force and Conductance Data .....	55
4.4	Theoretical Calculations of Bond Rupture Forces .....	60
4.5	Conclusion.....	64
<b>Chapter 5</b>	<b>Linker Dependent Bond Rupture Force Measurements in Single - Molecule Junctions .....</b>	<b>66</b>
5.1	Introduction and Motivation.....	66
5.2	Experimental Details .....	67
5.3	Junction Evolution of Molecules with Different Linkers.....	68
5.4	Statistical Evaluation of Lone-Pair Coupled Alkanes.....	70
5.5	Statistical Evaluation of Covalently Coupled Alkanes .....	74

5.6	Conclusion.....	78
<b>Chapter 6 Mechanical Properties of Silver and Palladium Atomic Contacts .....</b>		<b>79</b>
6.1	Introduction .....	79
6.2	Experimental Methods .....	80
6.3	Analysis Methods .....	82
6.4	Results and Discussions .....	83
6.5	Summary .....	93
<b>Chapter 7 Outlook.....</b>		<b>95</b>

## Table of Figures

Figure 1.1 Hydrogen Ion Molecule energy (red) and force (blue) as a function of nuclear separation. All distance units are scaled by the Bohr Radius a .....	4
Figure 1.2 Illustration of the STM break junction approach. A solid gold contact is elongated until atomically sharp contacts are formed. Upon breaking, a single molecule is contacted and measured.....	6
Figure 1.3 Scanning Tunneling Microscope images of a sharp (left) and plateau (right) AFM cantilever.....	9
Figure 2.1 Schematic of a laser detection based atomic force microscope (AFM). ....	12
Figure 2.2 Example conductance versus displacement traces for the molecule 1,4-diaminobutane (C4A). The traces are offset for clarity. Both gold and molecular signatures are clearly identifiable. ....	14
Figure 2.3 1D conductance histogram for 1,4-diaminobutane (C4A) constructed from 4000 consecutive traces. The histogram is presented on a log scale and demonstrates the clear conductance signature for C4A. The inset shows the gold features of the same traces on a linear scale. ....	14
Figure 2.4 1D histogram for 2000 traces of the molecule 4,4'-bipyridine showing two distinct conductance peaks. Inset shows the gold features on a linear scale. ....	15
Figure 2.5 Schematic drawing of the hardware components of the experimental setup. ....	17
Figure 2.6 Image of the CAFM setup suspended with bungee cords inside an acoustically and electrically insulated wooden box. ....	17
Figure 2.7 Schematic of experimental junction formation procedure .....	21

Figure 2.8 shows a comparison of a typical force trace before (red) and after (blue) the upgrade of the optical system. The blue trace is offset for clarity.....	22
Figure 2.9 The modified AFM head showing the fiber coupled, collimated, and focused super luminescent diode mounted on the AFM.....	25
Figure 2.10 Comparison of experimental spectral noise before (red) and after (green with 25mm lens and blue with 75 mm lens) the upgrades to the optical components. The inset highlights the resonance peak of the cantilever for the curves on a linear scale.....	25
Figure 2.11 Shows the standard deviations for 2500 force waves to indicate calibrated noise levels in units of nN for the old (red) and new (blue) laser setup. The improvement is almost a factor of ten. ....	27
Figure 2.12 Typical Force Spectroscopy signal used to calibrate the quadrant detector response.	29
Figure 2.13 Frequency dependent detector gain. The blue fit is used to correct the power spectrum when calibrating AFM cantilevers. ....	32
Figure 3.1 Typical force (blue) and conductance (red) measurements displayed as a function of piezo displacement. (A) Force and conductance evolution of an entire junction breaking process from loading of a thick gold contact to breaking of the final Au-Au contact. The lack of additional force events after the gold breaking event indicates that physical contact no longer exists. (B) Another example of a gold contact evolution. (C) Zoom in on a junction evolution just before the single atomic gold contact breaks and reveals force events indicating mechanical junction rearrangements even within the $1G_0$ plateau. ....	37

Figure 3.2 (Black) Sample accepted conductance trace showing both a  $G_0$  and molecular plateau.

(Red) Sample rejected conductance trace lacking the  $G_0$  plateau. (Blue) Rejected conductance trace lacking a molecular plateau. ..... 40

Figure 3.3 (A) Two-dimensional conductance histogram constructed from over 38 000 traces. All

traces are aligned such that the end of the plateau at  $G_0$  is at zero along the displacement axis. A large number of counts is visible at integer multiples of  $G_0$ .

Inset: Sample conductance trace aligned to zero displacement at the end of the  $G_0$  plateau. (B) Two-dimensional force histogram constructed from simultaneously

acquired force traces. The force profile (red curve) is overlaid and shows a clear jump at zero displacement. The rupture force of 1.4 nN for a single atomic contact is determined by extrapolating the fit of the force profile (dotted line). Inset: Force trace acquired simultaneously with conductance trace shown in the inset to panel A, aligned after the  $G_0$  break. The light blue trace is the raw signal and the dark blue is smoothed force data. .... 42

Figure 3.4 (A) Schematic illustrating how bond rupture force is determined on a trace-by-trace

basis for the traditional force analysis method. (B) Histogram of  $G_0$  bond-rupture force determined for 22000 traces selected from 49500 traces. A Gaussian fit is shown, and force peak is at 1.5nN. .... 46

Figure 3.5 Illustration of the force based event recognition procedure in combination with a

trace-by-trace force evaluation as applied to a typical gold junction evolution, including the breaking of a single atomic gold contact. The black trace is a manipulated force trace used to identify the force features. The green markers

indicate the determined force values before (squares) and after (diamonds) the breaking event..... 46

Figure 3.6 A schematic of the iterative fitting procedure. 400 three-line-segment curves (1,2,3) are fit to the force event by varying X1 and X2 incrementally. The best fit is chosen by selecting the minimal fitting error. ..... 47

Figure 3.7 Junction stiffness measurements for 1,2,3G<sub>0</sub> obtained with the multi-line fit approach. 1441, 944, and 325 traces have been selected from a set of 2000 gold junctions. A correction to account for the cantilever stiffness in series has been applied. ..... 48

Figure 3.8 2D force histogram with an averaged force profile indicating the effects of capacitive forces at high applied biases. This plot consist of about 1000 individual traces taking at an applied voltage between 500 and 750 mV. ..... 52

Figure 4.1 (A) (a) Two-dimensional conductance histogram of 1,4-butanediamine data constructed from over 10000 traces with a molecular conductance step. The conductance data is presented on a log scale. Features representing a sequence of gold contacts clearly appear at integer multiples of G<sub>0</sub>. A molecular signature can be clearly seen at  $1 \times 10^{-3}$  G<sub>0</sub>. Inset: A sample conductance trace showing a G<sub>0</sub> and molecular plateau with zero displacement set to the end of the molecular plateau. (b) The two-dimensional force histogram for 1,4-diaminobutane is constructed from the set of simultaneously acquired force traces used to construct the conductance histogram. The average force profile (black curve) shows a clear drop at zero-displacement, which gives a statistically determined breaking force for the N-Au bond of 0.69 nN. Inset: The simultaneously acquired force trace aligned after the molecular step is shown both unsmoothed (light blue) and smoothed (dark blue).

Force events corresponding to a G0 rupture and molecular breaking are clearly visible..... 56

Figure 4.2 (A) Two-dimensional conductance and (B) force histograms for 1,4 benzenediamine.  
Histograms are for 7345 traces selected from 58000 traces. The insets show a typical molecular conductance and force trace respectively aligned after the molecular plateau. The red trace in (B) indicates the average force profile..... 57

Figure 4.3 (A) Two-dimensional conductance and (B) force histograms for 1,6 hexanediamine.  
Histograms are for 6431 traces selected from 34000 traces. The insets show a typical molecular conductance and force trace respectively aligned after the molecular plateau. The red trace in (B) indicates the average force profile..... 58

Figure 4.4 (A) Two-dimensional conductance and (B) force histograms for 4,4' bipyridine for one tip/sample pair. Histograms are for 3423 traces selected from 11000 traces. The insets show a typical molecular conductance and force trace respectively aligned after the molecular plateau. The red trace in (B) indicates the average force profile.58

Figure 4.5 (a) Calculated total energy curves from adiabatic trajectories for 1,4-benzenediamine (red), 1,4-butanediamine (blue), and 4,4' bipyridine (green) shown as a function of displacement. Bars shown at right indicate the asymptotic values. (b) Calculated applied force curves for the same molecules shown against displacement display the same trend as the experimental results. (c) Junction structure showing a 1,4-benzenediamine junction at 0.1 nm elongation relative to the local energy minimum. (d) Zoom in of the Au-N bond indicating bond angle with respect to pulling direction. (e) Sample structure used to investigate a single Au-N bond force profile

for 1,4-benzenediamine bound to a gold electrode with bond aligned to the pulling direction ..... 62

Figure 4.6 (A) Calculated total energy and (B) force curves from adiabatic trajectories for a well-aligned model structure for 1,4-benzenediamine (red), 1,4-butanediamine (blue), and 4,4' bipyridine (green) shown as a function of displacement. Initial geometry as illustrated in Figure 4E in the text, with the N-Au bond aligned to vertical. Displacement controlled by fixing the position of the back plane of Au atoms in the cluster modeling the electrode and the N atom bonded to the Au tip atom..... 64

Figure 5.1 Sample conductance (red) and force (blue) traces for gold only (left), C4SMe (middle), and C4SH (right). All three traces exhibit characteristic gold features above  $1G_0$  and molecular signatures below for the case of C4SMe and C4SH..... 67

Figure 5.2 (A), 2D conductance histogram (15542 traces) for clean gold traces showing quantized steps above  $1G_0$  and a clean break to experimental noise. (B) 2D force histogram for the same traces as (A) with the average force profile in black indicating a most probable breaking force for the gold-gold bond of 1.4 nN. .... 69

Figure 5.3 (A) 2D conductance histogram for C4SMe constructed from 9774 traces, showing quantized conductance features of the gold breaking and the molecular signature at a conductance value of  $1.4 \times 10^{-3} G_0$ . The inset shows a sample conductance trace. (B) 2D force histogram for the simultaneously acquired force traces with the average force profile in black indicating an average breaking force of 0.66 nN. The inset shows the corresponding force data for the same sample trace. .... 70

Figure 5.4 (A), 2D conductance histogram (3544 traces) for C4A showing quantized steps above  $1G_0$  and a typical molecular signature at around  $10^{-3} G_0$ . (B) 2D force histogram for

the same traces as (A). The average force profile indicates a breaking force of 0.62 nN..... 72

Figure 5.5 (A), 2D conductance histogram (1694 traces) for DPPP showing quantized steps above  $1G_0$  and a typical molecular signature for DPPP at around  $6.6 \times 10^{-4} G_0$ . (B) 2D force histogram for the same traces as (A). The average force profile indicates a breaking force of 0.77 nN..... 72

Figure 5.6 One dimensional conductance histograms for C4SMe (green, 10000 traces) and C4SH (blue, 14000 traces). The lack of a clear peak for C4SH is evident and the higher overall counts in the molecular region indicate conductance features ranging from below gold to experimental noise. The dashed lines represent log binned histograms of the respective sets and are plotted against the right axis..... 73

Figure 5.7 (A), 2D histogram showing all identified force events versus conductance right before the force event for C4SMe (top) and C4SH (bottom). The histograms include 51000 and 121000 individual force events respectively. The conductance bin size is 30 bins per decade, and the force bin size is 0.04 nN. (B) Histogram of force events for C4SMe (green) and C4SH (blue) with associated conductance values ranging from  $10^{-2}$  to  $10^{-3} G_0$  composed of multiple data sets..... 75

Figure 5.8 Histograms of largest force events per trace with conductance values consistent with molecular features for C4SMe (green, 10092 events) and C4SH (blue, 22888 events).  
..... 78

Figure 6.1 Schematic of the conductive atomic force microscope break-junction technique. .... 80

Figure 6.2(A) Example silver conductance and force trace. (B) Normalized 1D conductance histograms for gold (6000 traces), silver (10000 traces), and palladium (8000 traces).

Compared to gold, silver and palladium do not form long single atomic gold chains  
and also show significant conductance features below the single atomic contact as  
indicated by the high counts. .... 81

Figure 6.3 Correlation plot for 25000 Ag conductance traces along with a vertical profile at 0.9  
 $G_0$ . The plot supports the anti-correlation of .4  $G_0$  steps with 1 $G_0$  and 2.5  $G_0$  steps. It  
also shows the positive correlation of 0.4  $G_0$  with 1.3  $G_0$ , both of which are attributed  
to O impurities in the Ag point-contact. The negative spots just below .4  $G_0$  indicate  
the presence of plateaus at around 0.4  $G_0$ ..... 85

Figure 6.4 Correlation plot for 6000 Au conductance traces. The distinct step features observed  
for silver at around 0.4  $G_0$  are not observed for gold. .... 85

Figure 6.5 Conductance histogram for the three selected cases of clean silver (blue, 878 traces),  
silver and oxygen in parallel (red, 1864 traces), and silver and oxygen in series  
(green, 1138 traces). .... 86

Figure 6.6 (A) Two-dimensional conductance and (B) force histograms aligned at the break from  
1  $G_0$  for Silver. Histograms are for 878 traces selected from 22000 traces. The red  
trace indicates the averaged force profile. .... 88

Figure 6.7 (A) Two-dimensional conductance and (B) force histograms aligned at the break from  
1  $G_0$  for Palladium. Histograms are for 1054 traces selected from 13000 traces. The  
red trace indicates the averaged force profile. .... 88

Figure 6.8 (A) Two-dimensional conductance and (B) force histograms aligned at the break from  
0.4  $G_0$  for Silver. Histograms are for 1138 traces selected from 22000 traces. The red  
trace indicates the averaged force profile. .... 89

Figure 6.9 (A) Two-dimensional conductance and (B) force histograms aligned at the break from 1.3 G <sub>0</sub> for Silver. Histograms are for 1864 traces selected from 22000 traces. The red trace indicates the averaged force profile. ....	89
Figure 6.10 Averaged force profiles for silver, silver-gold, and silver with oxygen in series and parallel. ....	90
Figure 6.11 (A) Conductance histogram for Gold, Palladium, and Gold/Palladium. (B) Conductance histogram for Gold, Silver , and Gold/Silver.....	91
Figure 6.12 (A) Two-dimensional conductance and (B) force histograms aligned at the break from 1 G <sub>0</sub> for Silver/Gold junctions. Histograms are for 530 traces selected from 3000 traces. The red trace indicates the averaged force profile. ....	91
Figure 6.13 (A) Two-dimensional conductance and (B) force histograms aligned at the break from 1 G <sub>0</sub> for Palladium/Gold junction. Histograms are for 1315 traces selected from 5000 traces. The red trace indicates the averaged force profile. ....	92
Figure 6.14 Force profiles for silver, silver-gold, palladium, and palladium-gold.....	93

## Acknowledgments

The completion of this thesis is the cumulation of curiosity and years of dedication. It would not have been possible without a tremendous amount of help from colleagues, friends, family, or even an unknown admissions officer at Berkeley. They provided a vision, academic advice, emotional support, love, and a chance, all of which I desperately needed at some stage of this journey.

I would like to express my gratitude to my advisor Latha Venkataraman. I vividly remember our first meeting about a possible project in her emerging research group. The passion for her work and her vision left no doubt this is what I wanted to do. I benefited from her expertise and patience in the early and her trust and freedom in the later stages of my work. Her demands for high quality and attention to detail have set an exceptional standard. I much appreciated her compassion and understanding throughout the years but especially during my two knee surgeries.

I thank our collaborator Dr. Mark S. Hybertsen for many stimulating theoretical insights and extensive contributions in the form of DFT calculations. Many thanks go out to every past and present member of our research group. Sriharsha Aradhya has made significant contributions to the AFM setup, particularly his part in the upgrade process has led to outstanding results. I am happy to leave my work and the force division of our group in his dedicated and knowledgeable hands. I was fortunate to share my entire graduate career with Masha Kamenetska. It started while studying for qualifying exams and will end with a near simultaneous defense. In between, I learned to admire her strength and intelligence and without her open ears to the occasional rant my graduate studies would surely have ended differently.

I was lucky to make a great group of friends. The many parties, soccer tours, camping trips, mario-cart sessions, and family dinners provided an essential escape and made the years in New York a time I will always remember. Daisuke and Paul and all the magic of 5B along with Teresa and her cookies will be sorely missed.

My brother Stefan, my mom Marlies, and my dad Erwin, deserve credit for my work. Their love, support, and sometimes criticism have built a foundation for a lifetime of possibilities. For all the time, emotional support, and also financial resources they have contributed, I share this achievement with them. Finally, my deepest gratitude to my love Adriana. For eight years she has supported me, often compromising on her own goals. The love, excitement, and happiness she instills in my life are beyond words.

Thank You

Michael Frei

## **Dedication**

This thesis is dedicated to  
Adriana and my Family

# Chapter 1 Introduction to Single Molecule Force and Conductance Measurements

## 1.1 Motivation: Why Single Molecule Measurements

The focus of this thesis is the experimental characterization of single molecules junctions by simultaneous measurements of force and conductance. The question arises why this study is pursued. The answer is simple: Single molecule junctions provide a unique system to probe physical and chemical concepts that lay experimentally inaccessible only a few years ago. Technological advances in a variety of microscopy tools and nanofabrication techniques enable unprecedented control over nano-scale objects such that experimental realization of theoretical predictions dating back to 1974 promising a single molecule rectifier are suddenly within the realm of the possible.<sup>1-2</sup> As such, we desire to understand, control, and utilize these systems, and electrical measurements represent a successful first step. Conductance measurements of single molecules have been enabled through a variety of techniques including the break-junction technique and have yielded results investigating transport properties of systems as small as a hydrogen atom.<sup>3</sup> While the potential of conductance studies is far from exhausted, they often cannot explain or quantify the various system parameters that prove to be influential in the behavior of single molecules in an electro-mechanical system. This presents the motivation to develop an experimental technique providing information that refines our understanding of these systems. The choice of force as a complimentary probe allows for simultaneous probing of mechanical and electronic properties. In fact how do mechanics and electronics even relate on a single bond level? We understand the bond between two atoms as an energetically favorable sharing of electrons and with this picture in mind, the manifestations of the electrical and

mechanical properties of these systems must inherently be linked. Hence, the goal is to characterize the electrical and mechanical behavior and to gain a deeper understanding of their individual and combined roles in a single molecule system.

The remainder of this chapter lays a theoretical foundation, describes the state of conductance measurements in more detail, and provides an overview of single molecule conductance measurement techniques and experimental approaches to force characterization.

## 1.2 Theoretical Considerations: Conductance on the Single Atom Scale

What follows is a highlight of theoretical results relevant to this thesis and details can be found in the references.<sup>4-8</sup> In the macroscopic world the concept of conductance and mechanics evoke immediate citation of Ohm's Law and Newton's Second Law. For single atomic wires and molecular junctions however, Ohm's law is simply not applicable and the rupture of a single bond consisting of the overlap of shared electron distributions is ill explained by Newton's Law. Ohm's law, applicable in the diffusive regime, breaks down when the mean free path of an electron in a metal, such as gold, becomes comparable to the dimensions of the conductor. For gold this happens at about 40 nm at 273K,<sup>7,9</sup> well above the critical dimension sizes of the gold and molecular structures considered here and so the electron behaves in a ballistic manner. Consider the transport for a one dimensional (z-direction) conductor contacted by macroscopic leads on each side with a potential energy difference of eV. The net total current between the left and right lead can then be calculated as the product of number of electrons times their charge and velocity,  $I=n*e*v$ . In the x and y direction, the electrons are confined, leading to a set of transverse modes or conductance channels, enumerated by N that electrons with wavevector k can occupy. The occupancy of each energy level by an electron is determined by the Fermi

distribution function  $f(\varepsilon) = \frac{1}{\exp\left[\frac{\varepsilon-\mu}{kT}\right]+1}$ . If we consider, for simplicity, the zero temperature case and

also assume that the number of modes,  $M$ , is constant over the energy range defined by the applied bias, the expression for the net current simplifies and the conductance of the 1D channel can be written as

$$G = \frac{2e^2}{h} M \quad \text{Equation 1. 1}$$

So far we have assumed that each incident electron is transmitted through the one dimensional conductor. But not every channel is fully transmitting. Instead, for each mode and energy the electron has a finite transmission probability  $T_N$ . If  $T_N$  is assumed constant over energy the total current can be described as the summation of the transmission probabilities for each electron over all available conductance channels and we obtain the Landauer equation:

$$G = \frac{2e^2}{h} \sum_N T_N \quad \text{Equation 1. 2}$$

For the case of a gold single atom contact this result simplifies beautifully as only one mode is active with a transmission probability equal to one. We would therefore expect a single atomic gold chain to have a conductance of exactly one quantum of conductance:

$$G_0 = \frac{2e^2}{h} \approx 77.5 \mu S \quad \text{Equation 1. 3}$$

This is observed experimentally and will be used frequently in our experimental approach as a clear fingerprint of the formation of a single atomic gold contact.<sup>10</sup>

The approach for the calculation of conductance for a molecular junction is analogous: A transmission function is typically calculated using a density functional approach and it provides information on the available conductance channels and their respective transmission probabilities

as a function of energy. Integration of this function over the energy range defined by the applied bias will yield the total current flow through the junction. Further details about the density functional approach to molecular transport can be found in the above cited references.

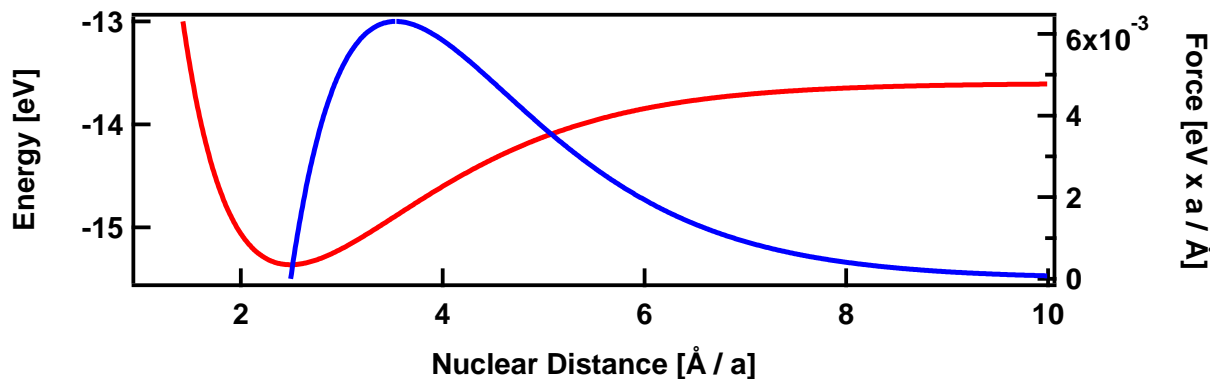


Figure 1.1 Hydrogen Ion Molecule energy (red) and force (blue) as a function of nuclear separation. All distance units are scaled by the Bohr Radius  $a$ .

### 1.3 Theoretical Considerations: Mechanics on the Single Atom Scale

The character of the mechanical bond between two atoms is determined by the specific electronic interactions of the atoms. In order to calculate the bond strength of a diatomic molecule for example, we would like to solve the Schrödinger Equation for the combined system.<sup>11-13</sup> From the resulting wavefunctions and energy profile as a function of nuclei separation, we can see that the bond is an energetically favorable arrangement that results from the overlap and hybridization of atomic orbitals. Hence, the underlying mechanisms for both conductance and force are the same. But even the simplest case of the hydrogen molecule ion can only be solved under the Born-Oppenheimer approximation. As a result, no simply analytical model exists and all theoretical bond breaking calculations presented as part of this paper were

obtained through DFT simulations. However, it is instructive to highlight typical results with the example of an approximate approach to the Hydrogen Ion case. Figure 1.1 shows the energy profile (red) for the bonding state as a function of the proton separation R for the Hydrogen Ion Molecule as obtained with the variational approach and a simple hydrogen atom ground state wavefunction.<sup>13</sup> The features of this energy landscape are typical of a bond breaking potential and analytically a Morse Potential<sup>14</sup> is used frequently as a simple equation describing the shape. Measured breaking forces can be compared to theoretical results by considering the maximally sustained force of a junction as obtained by differentiating the calculated energy profile with respect to the distance. Again, for illustrative purposes, the force versus extension curve (blue) obtained from the Hydrogen Ion molecule is indicated in Figure 1. 1 and the maximally sustained breaking force is evident. This is the procedure used to compare experimental breaking forces to forces calculated by DFT based approaches. In these comparisons, it is understood that the experimental measurements show a variety of possible junction evolution pathways, whereas the theoretical calculations are for a particular junction geometry. Ideally our force measurements would yield conclusive information about the underlying energy potential of the bond under consideration. We may be able to categorize individual bond breaking events and use that knowledge to definitely assign an event to a known bond. In experiment we do not probe the bond energy landscape directly however. Instead we measure quantities such as breaking force and junction stiffness. Due to underlying assumptions of various models, it is unclear how exactly these measured quantities can be used to reconstruct the energy profile but the development of an applicable model is an ongoing effort in our lab.<sup>15-23</sup>

## 1.4 Overview of Electrical Molecule Measurements

Forming electrical contact to a molecule that may only be about a nanometer in size is a challenge. Atomically sharp electrodes and reliable ways to attach molecules to such electrodes are needed. Nonetheless, an impressive array of experimental procedures exists that allows the investigation of electrical properties of single molecules or self-assembled monolayers (SAM) of molecules.<sup>24</sup> To form electrodes we use a Scanning Tunneling Microscope Break Junction (STM-BJ) technique<sup>25</sup> which is a variation of the Mechanically Controlled Break Junction (MCBJ).<sup>26</sup> The STM-BJ forms atomically sharp pairs of electrodes with angstrom sized gaps by stretching of a thin but solid metal wire until it eventually ruptures as illustrated in Figure 1.2. The conductance evolution of these metal nanowires during the breaking process has been studied extensively for varies metals and a comprehensive review of these systems is given in the references.<sup>27,28-29</sup> For gold, it is well established that these junctions reliably form a single atomic contact before the final rupture which is easily identifiable as the break from one quantum of conductance ( $1G_0$ ) to tunneling noiseconductance. Not only does this system offer reliable formation of atomically sharp electrodes, but the clear conductance signature of the thinning metal contact also provides an ideal fingerprint, allowing the identification or at least a narrowing of possible junction arrangements. The advantages of this are evident in comparison to alternative methods. For example, while Atomic

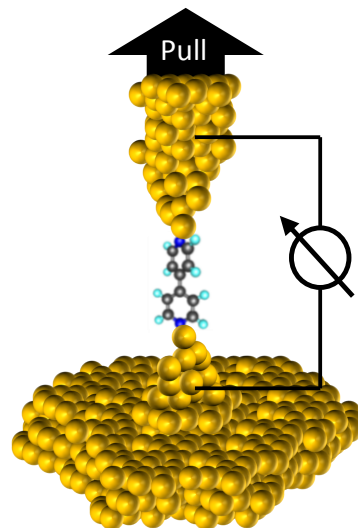


Figure 1.2 Illustration of the STM break junction approach. A solid gold contact is elongated until atomically sharp contacts are formed. Upon breaking, a single molecule is contacted and measured.

Force Microscope cantilevers have been used to study molecular systems, their typical tip radius is on the order of a few nanometers, a distance comparatively large if the goal is to contact a single diaminobutane molecule for example.<sup>30-31</sup> An alternative approach is the use of an atomically sharp scanning tunneling microscope (STM) tip that can be used in a combination of constant current or constant height mode. But as the reference<sup>24</sup> points out, it is possible to interpret changes in the observed current as either a change in the substrate and tip separation or a change in the medium between the tip and substrate.

Contacting of the molecules is achieved through physisorption or chemisorptions of specific chemical groups on the molecule to the electrodes. If the metallic contacts are broken in the presence of molecules terminated with chemical linkers that bind to the metal, then a single molecule junction can be formed frequently.<sup>25,32-38</sup> A conductance feature after the break from  $1G_0$  that occurs with statistical significance can then be attributed to a molecular junction. Furthermore, the atomically sharp tips geometrically limit the number of molecules in the junction. While they cannot be ruled out completely, junctions with two can be identified from conductance and hence single molecule junctions can be identified and studied unambiguously. Experimental and analytical details along with examples of STM-BJ conductance measurements are discussed further in chapter 2.

## 1.5 Atomic Force Measurement Techniques

Experimental determination of forces on the atomic scale has been realized with the invention of the atomic force microscope (AFM) in 1986.<sup>39</sup> The AFM offers a decisive advantage over scanning tunneling microscopy (STM) as it provides and imaging tool with atomic resolution applicable even for insulating samples.<sup>40</sup> As a result, its use is widespread and

diverse, including applications in biological systems<sup>41-44</sup> and imaging and characterization of nanometer-sized structures.<sup>45</sup> To give a few examples, protein folding and unfolding reactions have been studied with an AFM and allow for reaction rate analysis based on single molecule measurements.<sup>46</sup> Recently, the chemical structure of a single pentacene molecule has been resolved using an AFM based imaging technique probing the short-range chemical forces and the successful identification of single organic molecules in similar fashion has been demonstrated.<sup>47-48</sup> AFM techniques have proven invaluable in the mechanical and electrical characterization and manipulation of nanometer sized structures such as carbon nanotubes<sup>49-58</sup> where a pulsed CAFM can even be used to create defects in carbon nanotubes.<sup>59</sup> Given the wide variety of applications, it is not surprising that characteristic parameters such as length scales and force magnitude typical in these applications vary by orders of magnitude. This results in a number of variations and evolutions of the AFM mechanism demonstrated in 1986 but also in entirely different force application and detection concepts.<sup>60</sup> The following briefly highlights some of these experimental approaches and describes their respective capabilities and limitations.

An AFM relies on the detection of force through the physical reaction of a probe, typically by monitoring its deflection using a variety of different techniques. A common probe is a passive cantilever that is brought into contact or into close proximity with the sample to be evaluated. These cantilevers often feature sharp tips (diameter of a few nanometers) that are fabricated on soft micrometer-sized springboards, the deflection of which can be measured with different methods. A wide variety of spring and tip combination are available commercially. Figure 1.3 shows scanning electron microscope images for two typical cantilevers with a sharp tip and a plateau tip respectively.

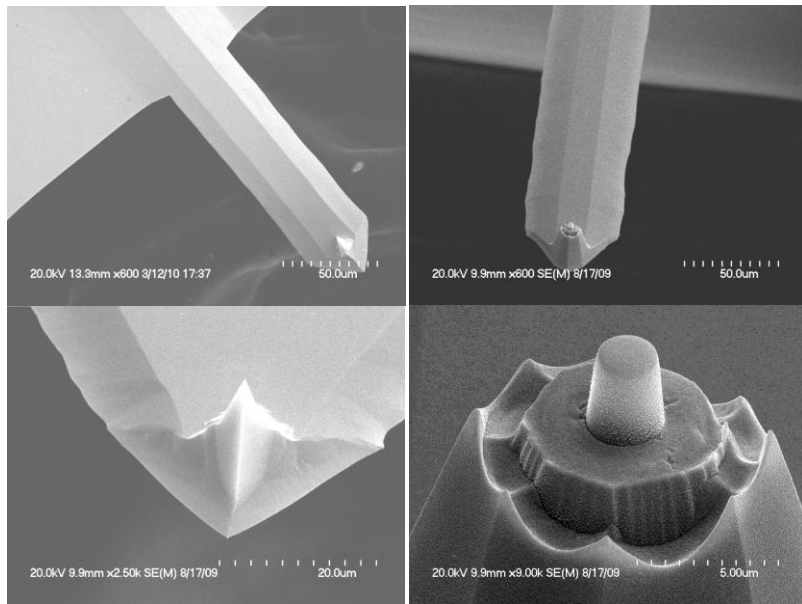


Figure 1.3 Scanning Tunneling Microscope images of a sharp (left) and plateau (right) AFM cantilever.

Important parameters of the cantilevers are the resonance frequency and stiffness  $k$ , which is defined as the linear coefficient relating the applied force  $F$  to the resulting cantilever deflection  $\Delta x$  under the assumption of linearity given small displacements. The most prevalent method to determine the deflection of the cantilever under applied force measures the deflection of a laser reflected off the backside of the cantilever. A split photodiode or quadrant detector is used to determine the corresponding angle changes in the reflected laser light. This method is most common particularly in commercial imaging applications and is the method of choice for the single molecule studies presented here. Other methods to determine the deflection of the cantilever include sensing techniques based on tunneling currents, changes in capacity, and fiber-optical interference.<sup>39,61-68</sup> In order to convert the measured deflection to applied force, a careful calibration is necessary and possible approaches to achieve this are discussed chapter 2. As cantilever stiffness vary from a few pN/nm to tens of nN/nm, a wide variety of experimental forces can be detected with this method.

Besides passive cantilevers, numerous alternative experimental techniques to apply and measure force on the atomic scale exist. Active cantilevers are a field of recent development that focuses on the elimination of an external detection system for deflection measurements. In these, changes in the resonance frequency of quartz tuning forks or the changes in the resistivity due to deflections of piezoresistive cantilevers are measured.<sup>69-70</sup> While the elimination of an external deflection detection system may be beneficial in vacuum and variable temperature experiments, the active oscillations of these cantilevers is often a major concern if control over length scales of fractions of an Angstrom is required. The stiffness of these force sensor are often much higher than for common cantilevers and range around a few thousand N/m. Optical and magnetic tweezers are another approach used frequently particularly in biological systems. Reference [71] provides an excellent overview and comparison of AFM and tweezer based approaches and highlights the differing parameter spaces for these three approaches. Finally, massive parallel single-molecule manipulation has been realized using centrifugal force setup.<sup>72</sup>

## 1.6 Outlook

This chapter motivated the need for simultaneous force and conductance data for the study of single molecule circuits and the following chapters will focus on developing and applying such experimental capabilities. Chapter 2 details the experimental setup and existing analytical methods for the evaluation of conductance data. Details of data analysis and statistical methods to evaluate force measurements will be presented in Chapter 3. We will test these methods using the single gold-gold bond as a standard before investigating the influence of the molecular backbone on the mechanical properties of junctions in Chapter 4. These results have been published in Nano Letters.<sup>73</sup> In addition to the influence of the varying backbone, we also

expect the nature of the chemical linker groups to affect mechanical evolution of the junction and we investigate this topic in Chapter 5 (This work is in preparation for publication). Finally, in Chapter 6 results from bond rupture measurements of silver and palladium are presented and contrasted with the properties of gold. Silver also offers interesting insight into junction formation in the presence of oxygen molecules. The combined work presented in these chapters not only presents insight into specific mechanical and electric phenomena in single molecular circuits, but also provides a novel experimental and analytical framework that enables future investigations of such systems.

## Chapter 2 Experimental Setup

As highlighted in Chapter 1, a common approach to single molecule conductance measurements is the Scanning Tunneling Microscopy Break-Junction (STM-BJ) technique and we will discuss this approach and results further. To move to simultaneous force and conductance measurements, we can then replace the tip wire electrode with a gold coated cantilever and a laser deflection detection system to form a conductive AFM (CAFM) as schematically shown in Figure 2.1. The CAFM approach also provides the appropriate cantilever stiffness and promises the force range and resolution needed to form and measure single metal-molecule-metal junctions. We utilized a commercially available AFM head (Veeco Multimode) as a convenient starting point to combine the STM approach with force measurement capabilities. After promising initial results, we undertook significant changes to the optical components of the AFM head; the motivation, execution, and results of which are discussed in detail later in this chapter.

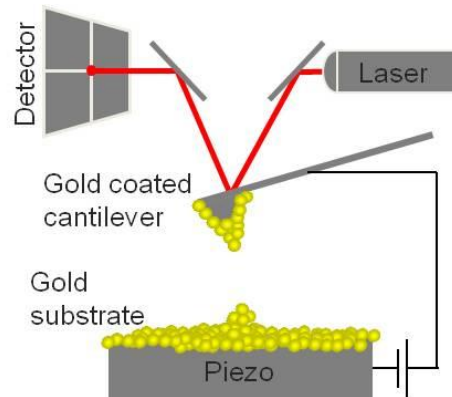


Figure 2.1 Schematic of a laser detection based atomic force microscope (AFM).

### 2.1 Single Molecule Conductance Measurements using STM Break Junctions

In chapter 1 we showed a schematic of a scanning tunneling microscope based break junction set up. Details about equipment components and substrate preparation are discussed

later in this chapter where a list of components for the CAFM version can be found, but the operating principle is simple: we smash a gold tip into a gold coated substrate and subsequently elongate the junction with an sub-Angstrom resolution piezoelectric positioner while reading current under an applied bias. The junction thins out and exhibits typical quantization of conductance until it forms a single atomic gold contact which breaks and allows for the potential formation of a molecular junction. Figure 2.2 shows typical traces of conductance on a log scale versus piezo displacement for the molecule 1,4-diaminobutane (C4A) and the gold features above  $1 G_0$  and molecular plateaus below  $1 G_0$  can clearly be identified. The formation and breaking of the junction takes about a second so that thousands of individual traces can be collected and statistically meaningful data sets can be recorded. Given that the formation of a junction starts with a thick gold contact, the subsequent molecular junctions formed are all structurally different. Any junction property including conductance and rupture force must be carried out using statistical significant data sets and with unbiased evaluation methods. A common method is to create one-dimensional histograms of thousands of traces without data selection by binning the conductance data.<sup>74-75</sup> If a conductance plateau at a particular value occurs with frequently, we expect a peak at in the histogram at the corresponding conductance value. Figure 2.3 shows a 1D conductance histogram for 4000 traces of C4A molecular junctions and we can clearly identify the quantized steps characteristic of gold (inset) and an additional peak below  $1G_0$  providing the molecular conductance signature. To highlight this approach further, we provide two examples of conductance studies that illustrate both the wealth of information conductance provides but also the need for mechanical information. Figure 2.4

shows a conductance histogram for the molecule 4,4'-bipyridine. We can see a

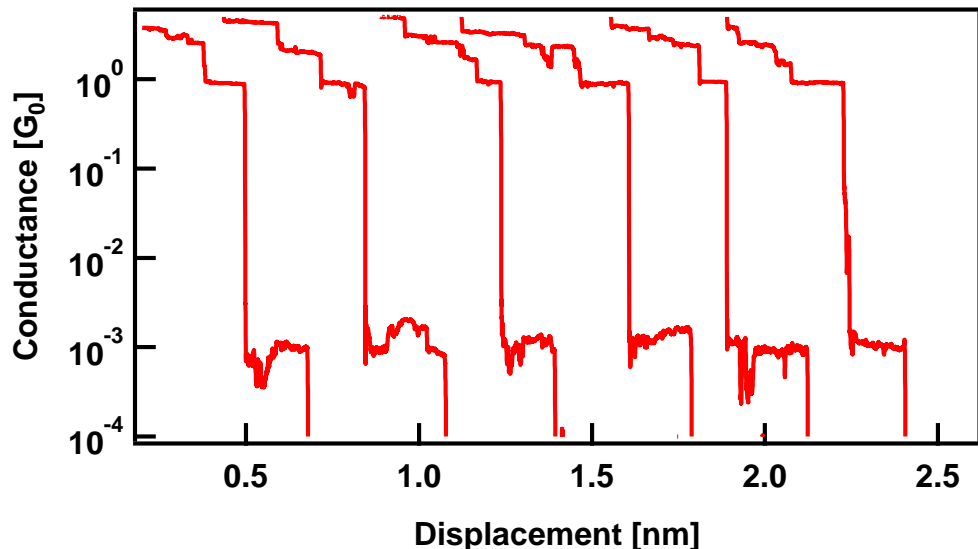


Figure 2.2 Example conductance versus displacement traces for the molecule 1,4-diaminobutane (C4A). The traces are offset for clarity. Both gold and molecular signatures are clearly identifiable.

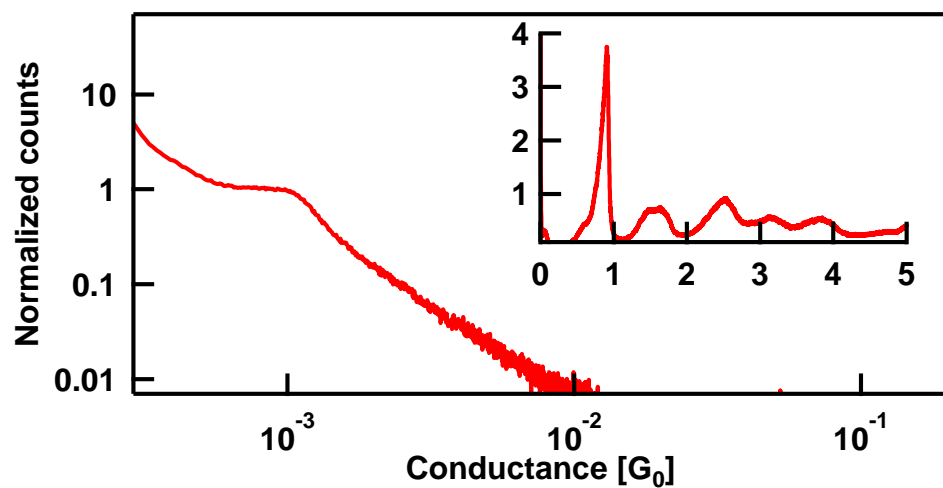


Figure 2.3 1D conductance histogram for 1,4-diaminobutane (C4A) constructed from 4000 consecutive traces. The histogram is presented on a log scale and demonstrates the clear conductance signature for C4A. The inset shows the gold features of the same traces on a linear scale.

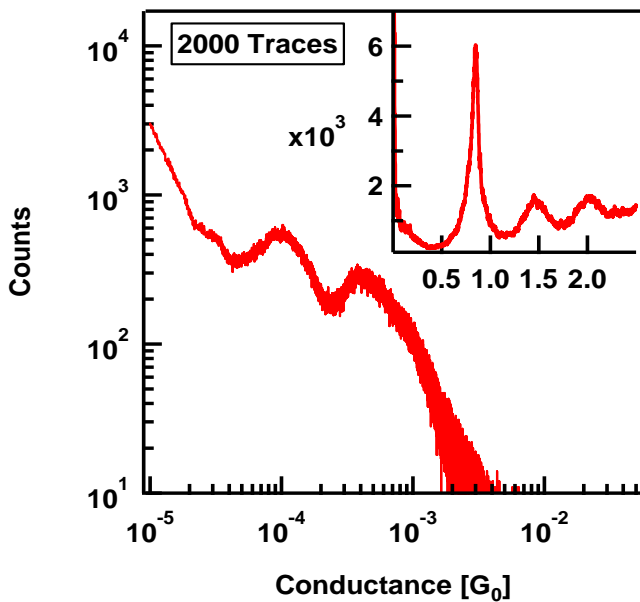


Figure 2.4 1D histogram for 2000 traces of the molecule 4,4'-bipyridine showing two distinct conductance peaks. Inset shows the gold features on a linear scale.

clear molecular signature. However, it has a pronounced double peak. The conductance data for this molecule has been investigated in detail<sup>76-77</sup> and the high and low conductance peaks correspond to two separate molecular junction orientations with distinguishable conductance values.

Based on displacement dependent conductance analysis, step-length analysis, and theoretical calculations we know that the low conductance state corresponds to the vertical binding of the molecule between the gold contacts through the nitrogen lone pairs. The high conducting state is attributed to a tilted molecule orientation that exhibits additional coupling of the gold electrode to the delocalized pi system of the molecule. This system perfectly illustrates our motivation to experimentally study force data to address the mechanical details of molecular junctions that have multiple conformations. Junction rupture force measurements and stiffness measurements could yield definite answers to questions relating to bond formation and rupture and to the contribution of pi-coupling to the junction stability. In the example with

4,4' bipyridine, it was also demonstrated that the conductance of a single molecule junction could be switched between the two peak values observed in the histogram. Using force measurements, one could address quantitatively the mechanical force that would be needed to switch a junction from one conductance state to the other. Thus a detailed understanding of this system could be achieved with additional information from force-based measurements. While not a topic of this thesis, it is indeed found that force offers valuable insight into the evolution of molecular junctions formed with 4,4'-bipyridine.

Molecular conductance measurements with molecules bound to metallic contacts through a thiol (SH) linker group are common and offer another example where force data could provide additional insight.<sup>78</sup> Single molecule junctions formed with thiol linkers show a wide range of conductance values when compared with alternative linker groups such as amines (NH<sub>2</sub>) or methylsulfides (SMe) that we have used widely. Specifically, amine linkers form molecular bridges with conductance features that are highly reproducible and with a narrowly defined conductance range when compared with molecules with thiol linkers.<sup>25,79</sup> This is concluded from observations on individual traces but also from statistical data sets evaluated using the 1D conductance histogram method. It has been shown theoretically that the difference between thiol and amine linkers is their different binding mechanism with gold. Sulfur-gold bonds are strong, covalent, and nonselective, properties that may lead them to bind in multiple geometries and potentially even disturb the gold electrodes significantly hence complicating the molecular junction conductance signatures.<sup>80-82</sup> Amines on the other hand, bind selectively to undercoordinated gold atoms through the N-lone pair forming a donor-acceptor bond. This bond is expected to be much weaker and, in addition to its selectivity, may not disturb the gold electrodes significantly enough to cause molecular conductance variation of several orders of

magnitude as seen in the thiols. Force rupture forces could help our understanding of the origin of these differences. We will show that amines do indeed form weaker bonds to gold when compared with thiols and also show that thiols can cause significant rearrangements to the electrodes during a molecular junction evolution.

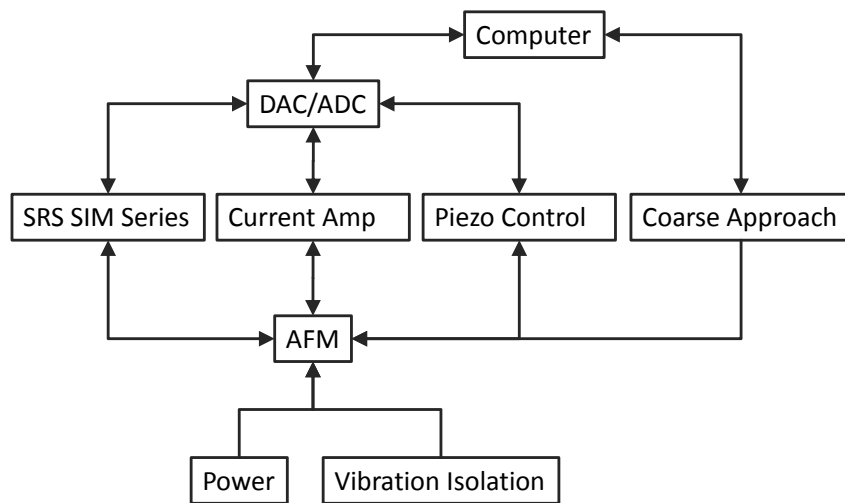


Figure 2.5 Schematic drawing of the hardware components of the experimental setup.

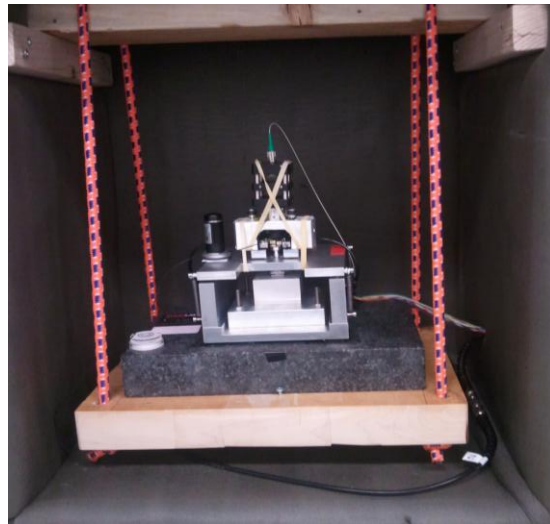


Figure 2.6 Image of the CAFM setup suspended with bungee cords inside an acoustically and electrically insulated wooden box.

## 2.2 Force and Conductance Measurement Setup

### 2.2a Hardware Components

Figure 2.5 shows a schematic of all hardware components of our simultaneous force and conductance experiment, while Figure 2.6 shows a picture of the AFM head, substrate holder, piezo positioner, and coarse approach mechanism suspended on bungee cords inside an insulated wooden crate for vibration isolation. A List of all component manufacturers, model numbers, and approximate prices can be found in Table 2. 1. All components of the experiment are controlled through a custom written software within the program IGOR.<sup>83</sup> This program directly controls settings and reads data from all hardware through serial and GPIB ports. The  $\pm 10V$  24 bit and 16 bit data acquisition cards (DAQ) which are typically operated at 100 kHz are also read using the custom software written in IGOR. These cards have both voltage input and output channels that function as digital to analog and analog to digital converters. Conductance is measured by reading the current between the two electrodes consisting of the metal substrate (usually gold) and the conductive AFM cantilever (usually gold coated) under an applied bias voltage. Both the substrate and AFM tip are electrically contacted directly by a thin magnetically shielded wire to minimize electrical noise and vibrations. The current is amplified and converted to a voltage signal by a current amplifier (Keithley 428-PROG) and finally read by the DAQ. The substrate is mounted on top of a single axis piezoelectric positioner, which controls the electrode separation with sub-Angstrom resolution and has a maximal travel range of about 1.5  $\mu\text{m}$ . The piezo controller has a built in resistive sensor to monitor the actual piezo displacement. The piezo is operated under open loop conditions, so no corrective adjustments are made based on the sensor information. In the experiments discussed here, it is sufficient to know precisely how much we have moved as opposed to moving exactly the programmed distance. The piezo positioner

Description	Company	Part #	Price
AFM Head	Veeco	Multimode	~14,000
Air table	TMC	63-563	4,085
Current Amplifier	Keithley	428-PROG	4,995
Z-Piezo	MadCity Labs	Nano-HSZ	8,900
Z-Piezo Controller	MadCity Labs	Nano-Drive™	-
AFM Cantilever Holder	Veeco	MMEFCH	1,600
SIM Mainframe w/GPIB	SRS	SIM900	1,495
Analog Summing Amplifier, 2x	SRS	SIM980	1,350
Analog Filter, 2x	SRS	SIM965	1,990
PXI Chassis, w/integrated controller	National Instruments	NI PXI-1033	1,099
24-Bit 2 Channel In/Out DAQ	National Instruments	NI PXI-4461	3,999
16-Bit 16/2 Channel In/Out DAG	National Instruments	NI PXI-6251	1,229
BNC Breakout box	National Instruments	NI BNC-2090A	439
PCI GPIB Interface	National Instruments	778032-51	599
IGOR Pro 6	Wavemetrics	11-500	395
Laser Temp. Controller	Arroyo	TECSource 3.5 A/ 7 V	995
LaserMount	Arroyo	212 DIL	345
Fiber Coupled 2mW 980 nm SLD with FC/APC	QPhotonics	QSSL-980-2	790
Ultra Low Noise Laser Diode Driver	ILX Lightwave	LDX-3620	2993
Near IR Achromatic lens	Thorlabs	AC254-060-B	83
Collimator	Thorlabs	CFC-11X-B-APC FC/APC	290
Misc. cage Components to align Optics	Thorlabs		200
		TOTAL	51,871

Table 2. 1, Hardware component list

has been accurately calibrated by the manufacturer and independently in our lab using the interference pattern of the total laser intensity as a function of the substrate and tip separation. The integral force detection components of the CAFM consist of a laser diode, quadrant detector,

and cantilever holder. The modified Veeco Multimode AFM head used in our experiment conveniently bundles a laser diode, quadrant detector, cantilever holder, and required mirrors and translation stages. Laser and detector power and voltage signals corresponding to cantilever deflection, and hence force, are interfaced through the 15 pin Min-E-Con cable. Originally the laser diode and detector were powered with a 6V and two 12V batteries respectively which allowed for continuous operation for about 24 hours. While the 15 pin connector also provides electrical contact to the cantilever, it has been found to be extremely noisy so that the cantilever is contacted directly instead. The voltage outputs from pins corresponding to each detector quadrant are added and subtracted using Stanford Research Systems (SRS) Summing Amplifiers to yield total laser intensity and vertical deflection data respectively. The vertical deflection data is also multiplied by a factor of ten using a SRS Scaling Amplifier. Before reading these two parameters with the DAQ they are filtered at 10 kHz using the SRS Analog Filters. The voltage signal proportional to the vertical deflection of the cantilever will have to be calibrated to yield absolute force values. This procedure is outlined later in this chapter.

Coarse approach is necessary because the piezo travel distance is limited to  $1.5 \mu\text{m}$ . This is achieved using a linear piezo actuator (Nano PZ, Newport). The coarse approach can be operated manually or automatically through a software interface controlled via the serial port. This is fully integrated to allow automatic approach based on both conductance and force feedback, which helps protect the cantilevers from breaking or blunting. After achieving contact, the actuator is disconnected to eliminate noise contribution otherwise visible in both force and conductance measurements. To minimize external mechanical and acoustic vibrations the CAFM setup rests inside a wooden crate as shown in Figure 2.6. The setup rests on top of a granite block which is suspended from bungee cords. The crate is lined with a grounded electrical

meshes to create an effective faraday-cage and a layer of acoustic insulating foam (McMaster-Carr, 5692T48). The entire box then rests on an optical air table (TMC). These combined isolation mechanisms have been quantified and evaluated through spectral analysis of vibrationally excited cantilever deflections measured both in and out of contact with the substrate. At a fraction of the cost, the isolation system performs better than active and passive commercial bench top solutions (BM-4 from minusK Technology and TS-150 from Table Stable) tested with the same methodology. This is especially true for the low frequency noise around a few Hertz.

## 2.2b Software for Experimental Control

The custom written IGOR software controls hardware components and data analysis functions. Specifically, the current amplifier and SRS mainframe housing the filters and summing and scaling amplifiers are interfaced using IGORs GPIB commands. This allows settings such as filter cutoff frequencies and amplifier gains to be initialized and set automatically. The National Instruments DAQ cards are controlled using IGOR extensions written in C and the serial coarse approach is addressed using IGOR's VDT2 command set. Temporal synchronization of the 24-bit and 16-bit cards is achieved by automated post-acquisition analysis of an artificially applied voltage spike which is read with both cards independently. This is done for each individual junction formation. The sequential actions taken as part of each junction formation are triggered by the software and are schematically represented in Figure 2.7. First, all parameters such as pulling speed and distance and applied voltage are set and output through the appropriate

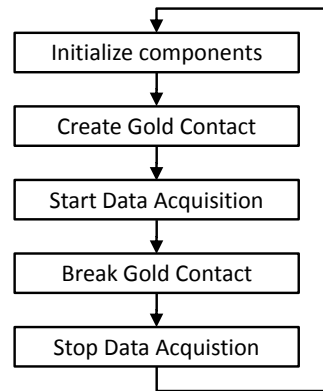


Figure 2.7 Schematic of experimental junction formation procedure

interface. Second, the voltage is applied to the piezo causing the substrate to approach the cantilever until a characteristic gold-gold junction conductance has been reached. Third, the data acquisition of conductance and force data is started at a rate of 100 kHz. The piezo is then instructed to retreat a fixed distance, typically 5nm, in order to break the gold contact and form a molecular junction if molecules are present. Finally, the data acquisition is halted and conductance and force traces are saved before the process begins anew. The software package also includes tools necessary to calibrate the cantilever so that deflection measurements can be converted to forces. This involves first converting the measured deflection in voltage to a deflection in nanometers using the piezo and then determining the spring constant of the cantilever as will be discussed in more detail later in this chapter.

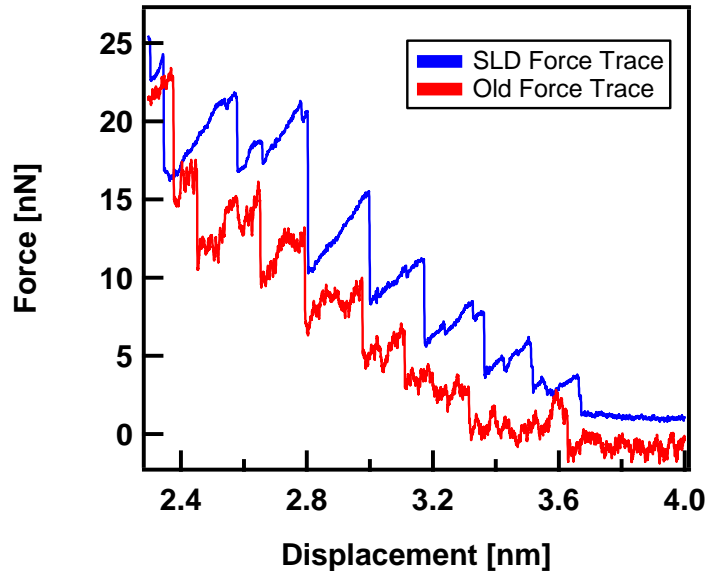


Figure 2.8 shows a comparison of a typical force trace before (red) and after (blue) the upgrade of the optical system. The blue trace is offset for clarity.

## 2.3 Noise Sources and Limitations

While the experimental setup as discussed so far has yielded successful gold-gold and gold-molecule breaking force measurements the noise levels in the force data was significant as is illustrated in Figure 2.8 where we show a typical force trace as taken with the setup (red trace). In order to improve the signal to noise ratio we started a targeted evaluation of the noise from all components of the system. We divided the setup into three functional units: the source, the instrument, and the detector. The source includes all components directly responsible for the laser beam used to measure cantilever deflection, particularly the laser diode, the current source powering the laser diode, and the optical components to focus and collimate the laser. The instrument unit consists of the cantilever, the holder, and mirrors and their respective positioning stages. The quadrant photodiode, its power and amplification circuitry, and the DAQ cards are part of the detector unit. Investigation of the instrument unit revealed two sources of noise, namely the thermal vibrations of the cantilever itself and vibrations of mirrors and stage components. The noise due to thermal cantilever motion can be estimated theoretically.<sup>84</sup> Assuming small cantilever displacements leads to a harmonic oscillator description with the following equation describing the thermal noise power spectral density,

$$x(f) = \sqrt{\frac{2k_B T}{\pi Q f_0 k} \left[ \left(1 - \left(\frac{f}{f_0}\right)^2\right)^2 + \left(\frac{f}{Qf_0}\right)^2 \right]} \quad \text{Equation 2.1}$$

where  $k_b, T, Q, k, f, f_0$ , represent the Boltzmann Factor, temperature, the cantilever quality factor, spring constant, frequency, and resonance frequency respectively. Typical parameters are  $T=293, Q=400, k=50 \text{ nN/nm}$ , and  $f_0=200 \text{ kHz}$ . This yields a noise floor of around  $1 \text{ fm}/\sqrt{\text{Hz}}$  at high frequencies. Our experimental level was around  $25 \text{ fm}/\sqrt{\text{Hz}}$  which indicated that we were not limited by thermal noise of the cantilever unlike experiments with biological molecules

where thermal noise is a primary limitation when using cantilevers with stiffness of a few pN/nm.<sup>42</sup> Noise contributions from the mirror and stage components were also investigated but have not found to be a problem.

The noise characterization of the detector components also suggested operation below our noise floors of around  $10 \text{ } \mu\text{V}/\sqrt{\text{Hz}}$  at 1 kHz. The summing and scaling amplifiers and DAQ card noise levels could be found from their manufacturers and indicated noise floors around tens of  $\text{nV}/\sqrt{\text{Hz}}$  at 1 kHz, which again was much lower than our noise levels. The detector noise floor was measured with and without incident laser light. This showed that the laser noise was the dominant noise source in our system. A detailed look at mechanisms contributing to noise originating in the laser source can be found in the reference.<sup>85</sup> To summarize, laser noise is intrinsic in the form of quantum and mode hopping noise and extrinsic in the form of “optical feedback noise” and interference because of secondary reflections. Experimental results with our system showed an insignificant effect of radio-frequency modulation to the noise levels and power dependent noise levels indicative of mode hopping and temperature instabilities and drifts. We concluded that mode hopping and temperature drifts were the dominant sources of noise in our force measurements.

## 2.4 System Upgrades

We modified the setup to address the laser noise problems using a temperature controlled and carefully powered super luminescent diode as the light source. These diodes output over a wider frequency range thereby decreasing mode hopping, optical feedback, and optical interference effects. We chose a 980 nm wavelength super luminescent diode (SLD) (QPhotonics, QSSL-980-2) with a power of 2mW because 680 nm SLDs at 2mW or larger were

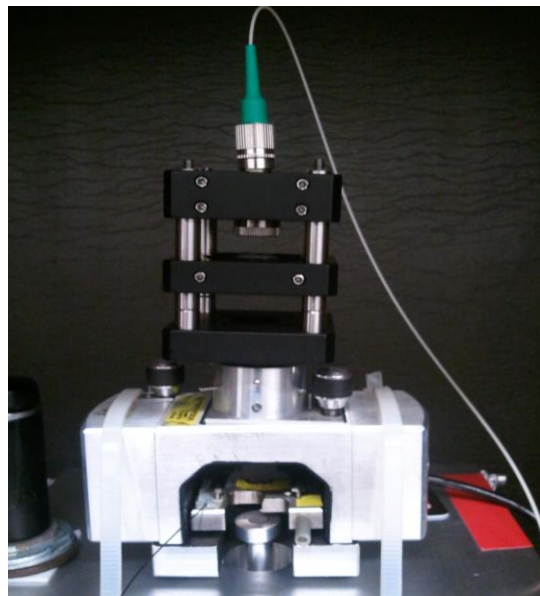


Figure 2.9 The modified AFM head showing the fiber coupled, collimated, and focused super luminescent diode mounted on the AFM.

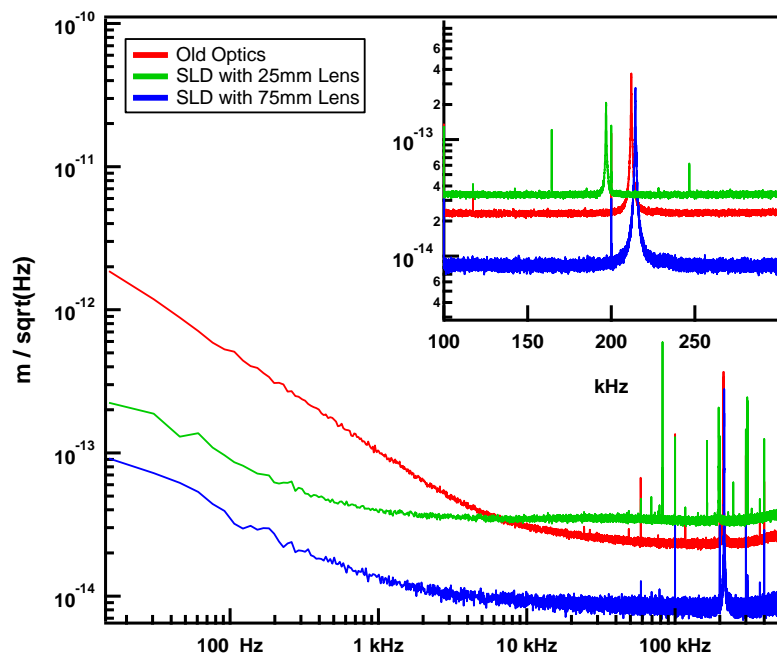


Figure 2.10 Comparison of experimental spectral noise before (red) and after (green with 25mm lens and blue with 75 mm lens) the upgrades to the optical components. The inset highlights the resonance peak of the cantilever for the curves on a linear scale.

hard to find and, because of large internal gain requirements, are more prone to damage from back reflections. The diode is temperature controlled (Arroyo, TECSource 3.5A/7V) and powered by an ultra low noise laser diode driver (ILX Lightwave, LDX-3620). Additionally we collimated and focused the beam in order to maximize the signal strength. Figure 2.9 shows a picture of the modified AFM head. The black optics housing (Thorlabs) holds the laser diode, collimator (Thorlabs, CFC-11X-APC), and focusing optics (Thorlabs, AC254-060-B) and allows for fine distance adjustments to optimize signal strength which depends on the proper collimation and focus of the laser with respect to the cantilever and detector. We found that the focusing lens has a dramatic impact on signal to noise ratio. A built in infrared filter in front of the quadrant photodiode has also been removed to ensure maximal incident laser power on the detector itself. Figure 2.10 quantifies the changes and compares the spectral noise in nm/ $\sqrt{\text{Hz}}$  for typical experiments taken with the original (red) components and new components both non-optimized (green) and optimized (blue). We see that the fully optimized system with the new SLD and optics has a noise floor that is about a factor of 10 lower for frequencies up to about 1 kHz the range most important for our measurements, and about a factor of 3 for higher frequencies compared to the old system,. The linear inset shows the resonance peak of the corresponding cantilever. We can see that the reduction in the noise floor has been achieved without sacrificing signal strength. We can also conclude that the proper alignment of the laser system is crucial. The green and blue traces were both taken with the new SLD but with lenses of differing focal lengths. To translate the changes observed in the spectral noise levels to the experimentally relevant force data, Figure 2.8 shows a typical force trace using the optimized system (blue). The difference compared with the data taken before the system upgrade is significant. The force associated with the breaking of a gold-gold bond is an ideal measure to

compare the signal/noise ratios before and after the system upgrade. While spectral noise data indicate significant improvements, the quantity of interest is the ratio between the force signal of a particular bond breaking event and the noise in the force for that particular trace. Figure 2.11 shows the standard deviations of the force trace for about 2500 measurements taken with the setup before (red) and after (blue) improvements, indicating an overall performance increase of almost a factor of ten.

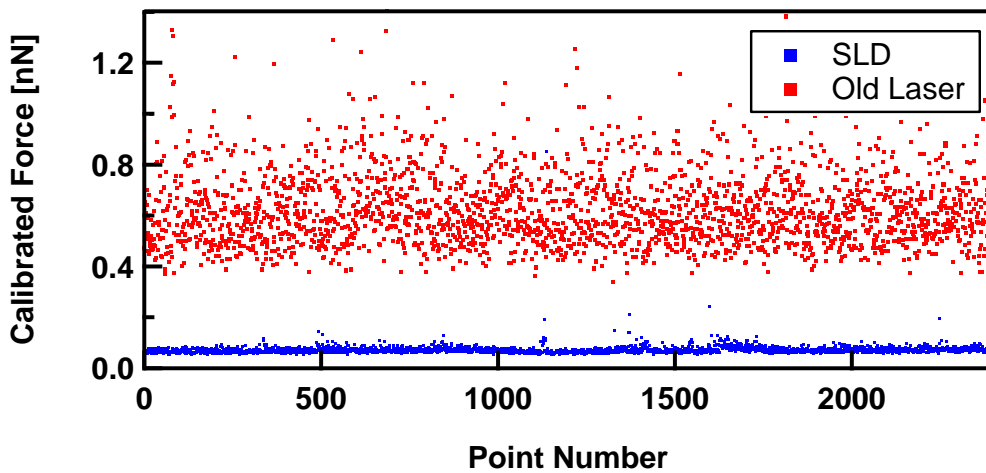


Figure 2.11 Shows the standard deviations for 2500 force waves to indicate calibrated noise levels in units of nN for the old (red) and new (blue) laser setup. The improvement is almost a factor of ten.

## 2.5 Cantilever Selection and Calibration

### 2.5a Cantilever Selection

Since the cantilever forms one electrode in the system, we need a conductive cantilever that is stiff enough to break a thick metal-metal contact down to a single atomic contact, but is also as soft as possible to provide the most force sensitivity since sensitivity scales linearly with the cantilever stiffness. Conductive gold-coated AFM tips that are needed here can be obtained from commercial sources. However, there are numerous issues why these are not suitable for our

work. The gold coating on commercial cantilevers usually peels off as the chrome adhesion layer used is typically not thick enough. For this work, we choose to coat all of our cantilevers in-house using a thermal evaporator (Edwards BOC/Auto 306). Typically we evaporate a 5-10 nm chrome adhesion layer followed by 110-140 nm of gold (Alfa Aesar, 99.999%). The backside of the cantilevers, the reflective side, is separately coated with a gold layer of about 40 nm to increase the reflectivity in the 980 nm wavelength range. This step is important as it has been found to increase the total laser power incident on the detector significantly. The ideal stiffness of a cantilever for our experiments is in the range of a few tens of nN/nm and a typical tapping mode cantilever with a stiffness constant of 40 nN/nm is strong enough to form the single atomic gold contact we require. Cantilevers with around 1 nN/nm are too soft as the gold-gold contact cannot be broken in a controlled manner. Instead, these soft cantilevers bend, load the junction, and then break spontaneously without forming an observable single atom contact. We initially used tapping mode cantilevers: PPP-ZEIHR from Nanosensors<sup>86</sup> and Tap300 from BudgetSensors<sup>87</sup>. These models have a nominal force constant of 27 and 40 nN/nm respectively. These cantilevers are sharp however, with a typical tip radius of a couple of nanometers and after repeated junction formation the evaporated gold layer peeled off around the sharp tip area rendering the cantilever non-conductive. To avoid such problems, we switched to using plateau tips PL2-NCH cantilevers from Nanosensors.<sup>86</sup> The platforms of these tips are formed by cutting of a conical tip by an ion mill to yield a plateau of about 2 micrometer in diameter. The stiffness and resonance frequency of the cantilevers are 42 nN/nm and 330 kHz nominal respectively. After a coating of gold as described above, these plateau tips are resistant to the peeling off of gold during the smash in each experimental cycle. Loss of conduction because of the depletion of gold at the tip/plateau region is hardly ever observed even after repeated smashing of the tip into

the substrate. This system is ideal as it allows for reliable data acquisition of thousands of traces without losing conductivity. Large gold-gold contacts can also be created which forces rearrangement of the tip atoms during experimental runs with the same tip-substrate combination. The plateau tips also proved to be simpler to calibrate accurately as the conversion from voltage to deflection distance can be accomplished more reliably as discussed below.

## 2.5b Cantilever Calibration

The experimental approach to measuring force, as described above, is to measure the voltage corresponding to the deflection of a cantilever and calibrate it to determine the force. This calibration is carried out in a two step process. First, we need to calibrate the detector by converting the acquired voltage signal into corresponding deflection of the cantilever in nanometers. Second, in the linear limit of small displacements, we deduce the force using the stiffness of the cantilever as  $F=k^*\Delta x$ . This step requires accurate knowledge of the cantilever stiffness  $k$ . The procedures to accomplish both steps are now outlined in more detail.

The detector is calibrated using the accurate displacement information of the piezo positioner which has been calibrated both by the manufacturer as well as in-house using laser interference method. Figure 2.12 shows a typical force spectroscopy curve used to calibrate the detector. The force curve starts with the cantilever approaching the substrate. We read a zero voltage signal since no deflection has taken place yet (red trace). As the cantilever pushes into

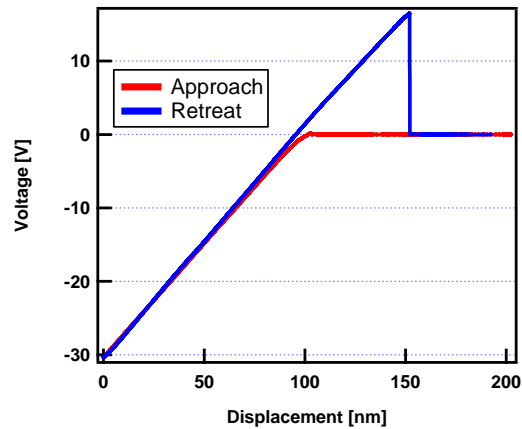


Figure 2.12 Typical Force Spectroscopy signal used to calibrate the quadrant detector response.

the substrate a solid contact is formed such that the substrate motion is equal to the cantilever displacement. This region is identified by the linear relationship between voltage and piezo displacement. The blue trace corresponds to the retraction of the sample with respect to the cantilever and retraces the approach curve until the cantilever experiences adhesion forces and finally snaps out of contact. The slope of the linear region gives a conversion from voltage to displacement.<sup>88</sup> The accurate determination of this slope is important and has been investigated. It is crucial to force a solid contact which can be achieved reliably by movement of a few hundred nm. Sharp tapping mode cantilevers, compared to plateau tips, show significant non-linearity resulting from gold rearrangements if a solid contact is not ensured. We find that the accurate calibration of cantilevers with a sharp tip on a gold surface is difficult and results in variability of the slope of about 30%. With Sharp tips, the slope should therefore be measured using a hard substrate such as glass. These problems have not been observed with the plateau cantilevers, presumably because of the larger contact area. For an accurate determination of the slope we use the data during the retraction of the substrate and avoid the area corresponding to the adhesion forces. We typically average three individual slope measurements to obtain a more reliable slope.

Numerous methods to determine the cantilever stiffness exist. An overview of these is given in the references.<sup>89-90</sup> We have evaluated four different methods. First, Sader's method, which is based on theoretical calculations in combination with experimentally determined cantilever quality factor, resonance frequency, and dimensions.<sup>91-92</sup> Although the method is accurate for uncoated tips, it does not capture changes in the spring constant of gold coated cantilevers. Second, the Cleveland method is based on measuring the changes in resonant frequencies of a given cantilever due to the sequential addition of precisely known masses.<sup>93</sup>

This method is hard to implement given that we need to calibrate a new cantilever for every experiment. The third method is based on calibration against well known reference cantilevers.<sup>94</sup> These cantilevers can be bought and their stiffnesses are precisely known. The unknown cantilever needs to be aligned and pressed against the reference cantilever, a task not easily possible with our AFM setup because it does not feature imaging capabilities. We have however verified that this method yields accurate stiffnesses when compared with our preferred method which is based on measurements of the thermal noise induced cantilever vibrations.<sup>88</sup> The method is quick, accurate, and non-destructive, allowing cantilevers to be used for multiple experiments. The method measures thermally induced cantilever vibrations as a function of frequency. The area under the resonance peak of this power spectrum is related to the thermal energy and can be equated to the potential energy of a simple harmonic oscillator as described in Equation 2.2, where  $k$ ,  $k_B T$ , and  $x$  are the cantilever stiffness, the Boltzmann factor, the temperature, and the cantilever displacement respectively. Corrections due to cantilever tilt angles have been proposed but are small and offset so that they can be ignored here.<sup>95-96</sup>

$$\frac{1}{2}k_B T = \frac{1}{2}k \langle x^2 \rangle \quad \text{Equation 2.2}$$

$$k = \frac{k_B T}{\langle x^2 \rangle}$$

In order to obtain a reliable thermal power spectrum we typically average 100 individual measurements which are taken with our DAQ at an acquisition frequency of 1 MHz. To prevent aliasing we filter the signal with the SRS Analog filters at 500 kHz. The square roots of the power spectral densities for different experimental configurations are shown in Figure 2.10 where the resonance peak is clearly visible. The peak in the power spectral density is fitted with a Lorentzian. The area under this curve corresponds to the thermal power exciting the cantilever.

For a given temperature, the stiffness  $k$  can then be calculated using Equation 2.2. It is critical to note that the detector gain must be calibrated in order to avoid errors. Typically, the detector gain depends on the laser wavelength and signal frequency. While this effect is negligible at low frequencies and in the visible spectrum range, around the resonance frequency of 200 kHz for typically used cantilevers, the gain of the detector is about 0.5. The actual power spectrum is therefore underestimated by almost a factor of 2 if this correction is neglected. The response curve of the detector has been determined accurately by modulating the laser with at different frequencies and constant amplitude. The observed changes in the power spectrum provide a gain versus signal frequency plot shown in Figure 2.13. The frequency range from 120-260 kHz was fit with an exponential that is used as a correction to obtain accurate stiffness measurements.

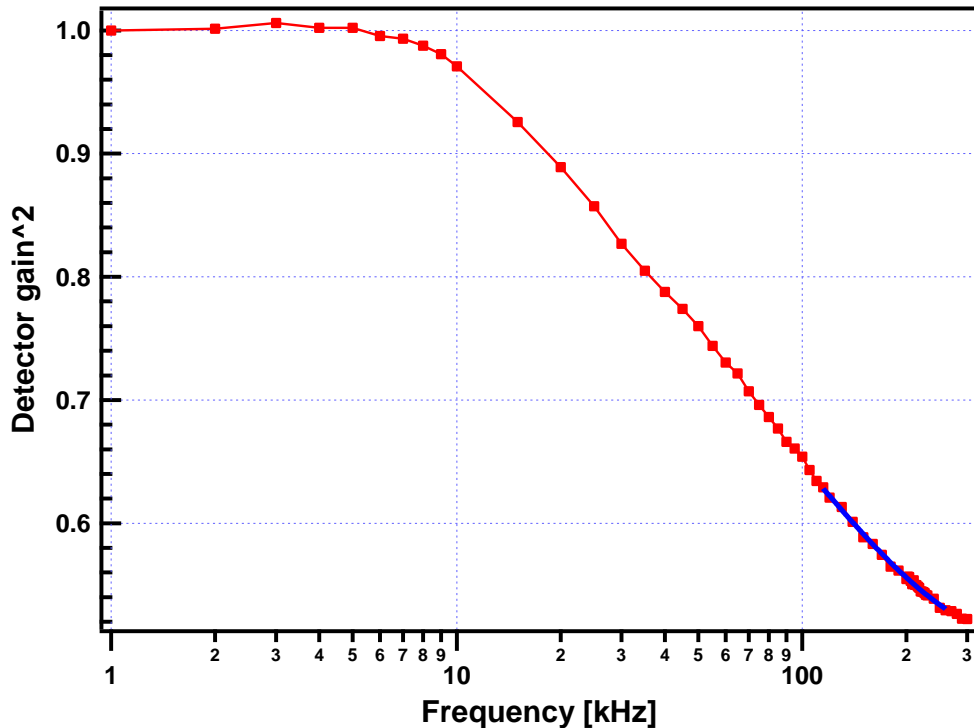


Figure 2.13 Frequency dependent detector gain. The blue fit is used to correct the power spectrum when calibrating AFM cantilevers.

## 2.6 Substrates Preparation and Molecule Deposition

The conductive metal substrates are formed by gluing a piece of mica sheet (TedPella, Prod. No. 52) onto an AFM Specimen Disc (TedPella, Prod. No. 16208) with conductive silver epoxy (TedPella, Prod. No. 16014). After cleaving of the mica sheet with scotch tape and cleaning them in a UV-Ozone cleaner (NovaScan PSD-UV) for 45 minutes, the substrates are coated with metal using a thermal evaporator. For gold, the samples are coated in a home-built evaporator used only for gold depositions to ensure clean substrates. Typically we evaporate about 100 nm of gold (Alfa Aesar, 99.999%) at a rate of about 2 Å/s and a base pressure of around  $5 \times 10^{-7}$  Torr. The samples are stored in ambient condition but UV cleaned prior to use. For metals other than gold a shared facility thermal evaporator (Edwards BOC/Auto 306) is used. Evaporation parameters are similar with rates of about 2 Å/s and base pressures around  $2 \times 10^{-6}$  Torr.

The deposition of molecules onto the substrate is done either through the addition of a dilute concentration of molecules in solvent or the thermal evaporation of the molecule onto the metal surface. While either procedure can yield excellent results, the method is dictated by the type of molecule and the success of both methods sensitively depends on deposition conditions. For thermal evaporation of the molecule, the substrate is held over the heated molecule. In the case of some thiol and methylsulfide terminated molecules no heating is required as the vapor pressure of the molecule is sufficient to create a layer of molecules on the metal surface. For evaporated molecules it is possible to deposit a thick layer of molecule. This layer is evident as the cantilever shows a distinct deflection before electrical contact is made with the metal surface. Single molecule force and conductance measurements are rarely possible under these conditions. In many occasions, the sample can be heated slightly to remove excess molecule coverage. It is

worth noting that the AFM setup is much more sensitive to the molecular layer thickness than the STM set-up which uses a stiff gold wire as a second electrode that can penetrate the thick molecular layers and form a metal contact. Depositing molecules by adding a few drops of a dilute solution to the metal substrate is an alternative method. The solvent prevents contaminations from depositing on the gold surface. However, running a force measurement with solvent is not straight forward. Capillary forces do not influence our force measurements as evident by the comparison of gold and molecule breaking force measurements in air and solvent. However, the often rapid evaporation of the solvent under elevated temperatures due to laser heating is problematic. This can be mitigated by using a high boiling solvent and frequently realigning the laser with respect to the center of the quadrant detector. For the solvent 1,2,4-trichlorobenzene (213°C from MSDS) for example, readjustment of the quadrant detector alignment is necessary after every thousand measurements while bromobenzene, which has a lower boiling point (156°C), cannot be run effectively. The solvents 1-phenyloctane (261°C) and tetradecane (252°C) were found to be ideal. When running experiments with too much solvent it can also happen that the solvent draws up on the cantilever holder, resulting in an increased conductance noise floor. Retraction of the cantilever from the substrate and subsequent removal of some of the liquid solves the problem and a continuation of the experiment is possible.

## 2.7 Summary

In this chapter we described the experimental AFM setup and described each component in detail. We have outlined our approach to increase the force resolution through the investigation of dominant noise sources and the subsequent introduction of a new optical system. The results were significant as an improvement of about a factor of 10 in the signal to noise ratio

has been achieved. Since the measured force data needs to be calibrated, procedures for the accurate determination of the cantilever stiffness and voltage to nanometer conversion have been discussed. Finally, gold and molecule layers have to be deposited onto the substrate and the cantilever and the respective methods have been discussed. We are now in position to apply these measurements to gold and molecular junction breaking measurements.

# Chapter 3 Force and Conductance Data Analysis for a Gold Point Contact

This chapter describes simultaneous conductance and force measurements of gold point-contacts, and introduces data analysis techniques used to extract bond rupture force results from statistically large data sets. Statistical evaluation methods for force data are analogous to the conductance histograms method introduced in chapter 2. As a benchmark, we apply these methods to determine the breaking force of a gold single atom contact. Results from measurements of molecular junction rupture forces are then discussed in the following chapters.

## 3.1 Gold Point-Contact Force and Conductance Data

Each experimental junction formation starts with a thick gold neck that is formed through the smashing of the gold coated AFM cantilever into the gold substrate. Subsequent elongation of the junction by moving the substrate away from the tip results in a gradual thinning of the gold contact until a point contact a few atoms in cross-section is formed and broken. While the conductance data shows steps at integer multiples of  $G_0$ , the quantum of conductance, the force data shows repeated features corresponding to loading and breaking of each configuration.<sup>27</sup> There is also a final breaking event after which the contact is broken and no additional features are observed in the force data. The loading events manifest themselves as gradual, linear increases of the force since the force acting on the junction is determined by the constant movement of the substrate away from the AFM cantilever. During this process, reversible rearrangements such as gold bond stretching in the junction dominate. Once the force on the junction reaches a magnitude that can no longer be sustained, the junction breaks irreversibly

into a new, longer configuration and adapts to the new geometric constraints as defined by the increased tip/sample separation. These sudden reliefs result in sharp and sudden drops in the force signal and, together with the linearly increasing features, produce a characteristic saw tooth pattern. This electrical and mechanical evolution of gold (other metals are limited to electrical measurements) nanowires has been studied extensively in the literature both theoretically and experimentally and a pronounced saw tooth pattern has been confirmed.<sup>28,97-110</sup> However, experimental measurements are limited to thicker gold contacts; single atomic gold-gold breaking forces have only been observed by one group and its statistical analysis has been limited.<sup>111-116</sup> Figure 3.1 shows three typical simultaneous measurements of conductance (red) and force (blue) versus piezo displacement for a gold-gold junction evolution. The trace in

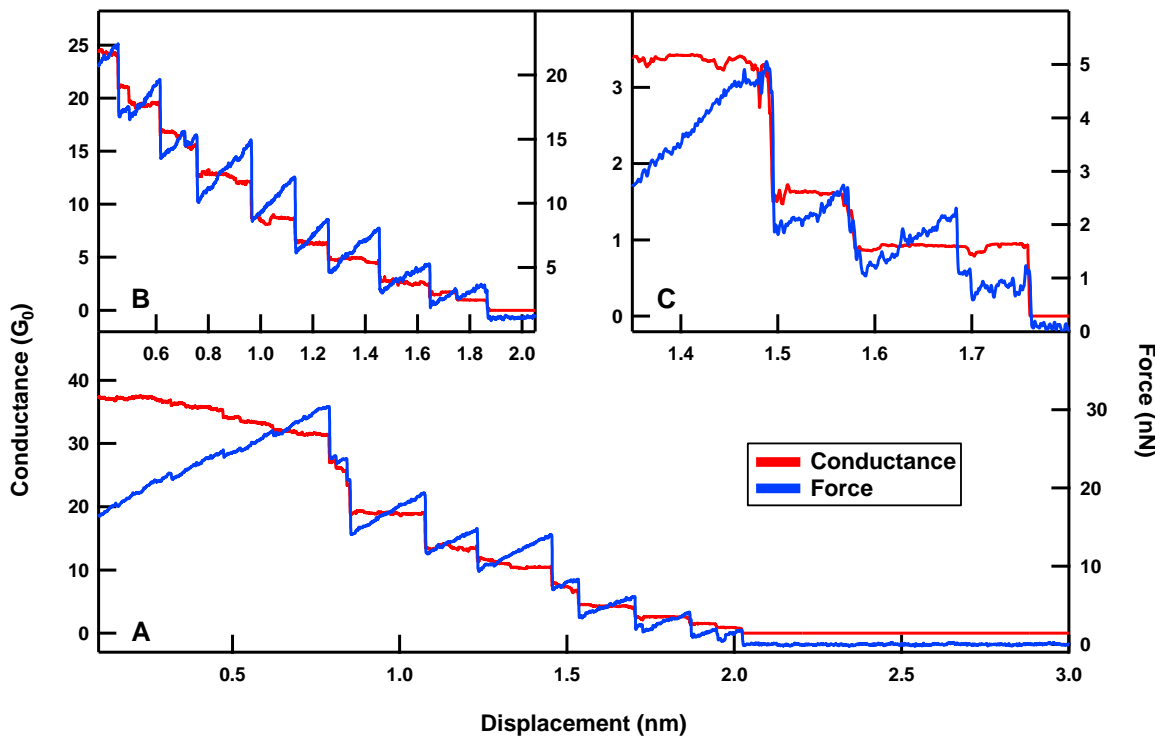


Figure 3.1 Typical force (blue) and conductance (red) measurements displayed as a function of piezo displacement. (A) Force and conductance evolution of an entire junction breaking process from loading of a thick gold contact to breaking of the final Au-Au contact. The lack of additional force events after the gold breaking event indicates that physical contact no longer exists. (B) Another example of a gold contact evolution. (C) Zoom in on a junction evolution just before the single atomic gold contact breaks

Figure 3.1A shows the evolution of the entire junction formation process, while Figure 3.1C shows the junction evolution just prior to the rupture of the single atomic gold contact. The conductance decreases in quantized steps until the formation of a single atomic gold chain with a characteristic conductance of  $1G_0$ . The end of this plateau serves as an identifier for final gold-gold bond rupture event. The force traces show the expected saw tooth pattern and provide clearly resolved mechanical junction evolution data all the way from a sizable gold neck down to a single atomic gold chain. Before focusing on the statistical analysis of the force event corresponding to the single atomic gold chain breaking, we should highlight the wealth of quantitative information the force data provides. Besides the rupture forces corresponding to irreversible junction rearrangements, we have junction stiffness information (slope of the force data immediately before the rupture event). We can also detect significant force events within a constant conductance plateau and the reverse situation of changing conductance without simultaneous changes in the force. The former is illustrated in Figure 3.1C; we can clearly see a significant mechanical rearrangement within a single atom gold contact of roughly constant conductance. And finally, the lack of force events after the  $1G_0$  plateau indicates that no mechanical contact exists between the tip and the substrate. All this information, can lead to new insight into junction formation down to the atomic contact that would not be possible with conductance data alone. Of course, each junction we form is an entirely new structure. It is therefore expected that significant fluctuations in measurable quantities such as bond breaking forces occur. As a result, a statistical analysis of thousands of measurements of the same event is necessary. The next sections outline different approaches, apply such statistical analysis to evaluate the rupture force for a single atom contact, and describe the methodology that will be

applied to molecular force and conductance data. Comparison to existing experimental results and theoretical calculations will test the validity of our experimental and analytical approaches.

## 3.2 Analysis of Force and Conductance

### 3.2a Conductance Step Recognition and Histograms

In order to evaluate a particular bond rupture force, we generally rely on the conductance data for a signature of the rupture event. Direct identification of force events is also possible and used for analysis of data that does not show characteristic conductance features or in cases that do not allow for conductance measurements. Thiol linked molecules are one such example and discussed as part of Chapter 5. The method used for direct, conductance independent force event recognition is discussed later in this chapter. For the majority of the molecules discussed in this thesis and for the single atom gold contact rupture, we do have a well established conductance signature that allows for a clear identification of the mechanical event under consideration. Conductance signatures for a wide variety of different molecules have been extensively studied experimentally in the literature and provide a reliable and accepted identification method.<sup>25,37,76-</sup>

<sup>77,79,117-132</sup> As such, the first step of the analysis of our force data is the identification of events of interest in the conductance measurement. Conductance step detection is carried out as follows: first, 1D conductance histograms are computed from all measured traces to determine the conductance peak and width. A typical 1D histogram was shown in Chapter 2 Figure 2.4 for 2000 consecutive traces measured with the molecule 4,4'-bipyridine. For single atomic gold chain measurements, the conductance range is from 0.5 – 1.2 G<sub>0</sub> (linear inset) and the peak height confirms a clean gold deposition. For molecules, we determine a most probable (peak value), minimum, and maximal conductance value. We then create a histogram of every trace

individually and sum the counts within the respective conductance window. If this value is larger than the number required for a plateau with a minimum length of 0.02 nm, the plateau length and slope, normalized to the average conductance value of the plateau, is obtained. Typically, traces with a conductance plateau longer than 0.02 nm and with a normalized slope larger than -5, are selected for further analysis. A fraction of the traces do not show a clear, well defined conductance plateau at  $G_0$  or a plateau corresponding to a molecular junction. It is likely that the absence of the  $G_0$  or the molecular conductance plateau means that a single-atom point contact or a single molecule junction was not formed during that trace. Figure 3.2 shows three sample conductance traces that illustrate these scenarios. The black trace shows both a  $1G_0$  and molecular plateau and would be included in the evaluation of either the gold or molecular breaking force. The red trace would be omitted from the evaluation of the gold breaking force because it is lacking a plateau at  $1G_0$  and similarly the blue trace would be omitted from the determination of a molecular breaking force

because it does not show a molecular conductance feature. Rejected traces cannot be used for further analysis because they do not contain the bond rupture event of interest. The statistical occurrence of the targeted junction varies and will be noted for each event under consideration, but a statistically significant and unbiased data set results in each case. Finally, the end of the conductance plateau is determined, and each

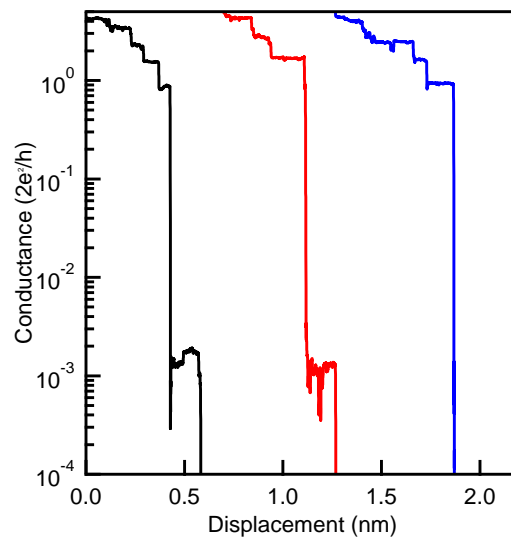


Figure 3.2 (Black) Sample accepted conductance trace showing both a  $G_0$  and molecular plateau. (Red) Sample rejected conductance trace lacking the  $G_0$  plateau. (Blue) Rejected conductance trace lacking a molecular plateau.

conductance trace is analyzed to ensure that they exhibit a sharp conductance drop following the plateau by requiring that the conductance immediately after the plateau is about ten times less than that of the plateau. This requirement ensures that the junction has a well defined breaking event. The location of the end of the conductance plateau is expressed in terms of the x-displacement of the piezoelectric positioner. Since this location is common to both the force and conductance data we can easily investigate force signatures of the corresponding junction rearrangements identified by the conductance features. The selection criteria are molecule independent and ensure the inclusion of well defined conductance steps. While the analysis of force data is discussed further below, the conductance data is not analyzed further for the projects discussed within this thesis. However, conductance data is typically presented in the form of 2D conductance histograms which have the benefit of preserved displacement information.<sup>77</sup> Such histograms are created by realignment of the displacement axis by redefining the displacement value at which the gold or molecular junction plateau breaks as zero displacement. All traces are now aligned along both the conductance and displacement axis such that thousands of traces can be added to form a two dimensional histogram. Figure 3.3A shows a two-dimensional conductance histogram aligned after the single atomic gold contact breaks. It is constructed from over 38000 individual conductance traces collected over approximately 20 different tip/sample pairs. The inset shows one representative conductance trace to illustrate the realignment to zero displacement at the break of the gold-gold contact. The 38000 traces were selected using the procedure described above starting from an initial set of 49500 traces. A 75% selection rate is typical for gold junctions as not every single junction evolution results in a clean, well defined single atomic gold contact. The histogram clearly shows the quantized evolution of the gold junction before rupture of the single atomic contact as steps

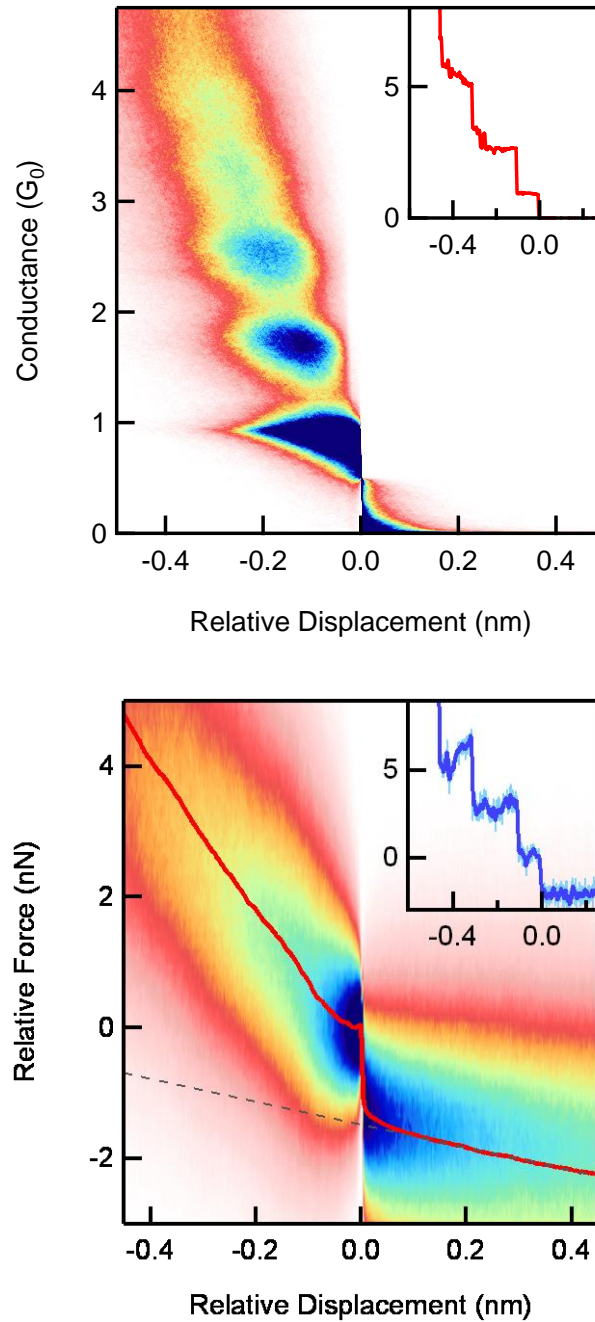


Figure 3.3 **(A)** Two-dimensional conductance histogram constructed from over 38 000 traces. All traces are aligned such that the end of the plateau at  $G_0$  is at zero along the displacement axis. A large number of counts is visible at integer multiples of  $G_0$ . Inset: Sample conductance trace aligned to zero displacement at the end of the  $G_0$  plateau. **(B)** Two-dimensional force histogram constructed from simultaneously acquired force traces. The force profile (red curve) is overlaid and shows a clear jump at zero displacement. The rupture force of 1.4 nN for a single atomic contact is determined by extrapolating the fit of the force profile (dotted line). Inset: Force trace acquired simultaneously with conductance trace shown in the inset to panel A, aligned after the  $G_0$  break. The light blue trace is the raw signal and the dark blue is smoothed force data.

at integer multiple of  $1G_0$  can easily be identified for negative relative displacements. With the procedures outlined above we can now successfully use conductance to identify the displacement position at which a force event of interest occurs. We now need to develop a statistical method to analyze the corresponding force data and two methods are used throughout the work discussed in this thesis.

### **3.2b 2D Force Analysis**

Analogous to the two-dimensional conductance histograms, we constructed two-dimensional histograms from the force traces, setting the origin of the displacement axis at the point where either the  $1G_0$  conductance step or the molecular conductance step breaks. This well-defined position on the x-axis was determined individually for each trace, using an unbiased automated algorithm as discussed above. Not every trace exhibits the conductance and force features under investigation. It is important to note though that the 2D force histogram method includes every trace that does exhibit a conductance feature of interest. This is in contrast to the trace-by-trace force evaluation method (see below) where some force events have to be excluded due to fitting issues, even though the conductance trace shows a plateau. Since the force signal is a relative measurement, each force trace needs to be aligned in the force coordinate as well as in the position coordinate. This is achieved by setting the force at the new zero-displacement position to zero by subtracting an offset from the entire force trace. This will realign all force traces to a common point such that each force and displacement value is now determined relative to that at the end of the conductance step in each trace. After this realignment, thousands of force traces are added to generate a two-dimensional force histogram. A statistically averaged force profile is obtained from this histogram from the peak of a Gaussian that is fit to vertical sections at every displacement bin. Figure 3.3B shows a two-dimensional force histogram, constructed

from over 38 000 traces measured without any molecules present and using approximately 20 different tip/sample pairs. Inset to Figure 3.3B shows a sample force trace, illustrating the alignment along the position and force axis. As in the 2D conductance histogram, negative displacements are events that occur before the end of the  $1G_0$  plateau while positive corresponds to data acquired after the end of the plateau. The force histogram is created from the same set of traces as the 2D conductance histogram shown in Figure 3.3A, and shows a trend in the force that is decreasing with increasing displacement with a clear sharp drop at zero displacement. The force required to break the  $G_0$  contact can be determined from the magnitude of this drop. The force profile is effectively an averaged force trace for the single atom contact rupture event. It shows a clearly defined drop of 1.4 nN corresponding to the breaking force of a single Au-Au bond. The error in the determined force is found to be about 0.1nN, as determined by the standard deviation of the measured breaking force for identical junctions on multiple days and with multiple tip and substrate combinations. This value is in good agreement with published results and demonstrates that our 2D analysis method agrees with the conventional, trace-by-trace evaluation method.<sup>108,111-116</sup> However, we note here that this analysis method is not biased toward larger force drops which are easier to identify if individual traces are analyzed as will be discussed below. This ensures the inclusion of force events of small or even zero magnitude and explains the slightly smaller force magnitude when compared to the trace-by-trace method described below. These events are certainly physically feasible and as such should be considered in a statistical analysis of breaking forces. We would also like to draw attention to the size of the data set of about 38000 individual breaking events, providing the first robust and unbiased determination of the single Au-Au bond breaking force.

### 3.2c Trace-by-Trace Force Analysis

Unlike the conductance data, the force data does not show plateaus, but rather saw-tooth patterns. Consequently, the calculation of a force drop on a trace by trace basis, without using the 2D analysis method, cannot be achieved by simply creating a histogram. Analysis of the force data relies on the simultaneously acquired conductance data. The force associated with a given breaking event which is determined from the conductance data is the difference between the cantilever deflection prior to the break and that right after the break. This can be determined on a trace by trace basis using an automated algorithm by either fitting a line to the force data in the region before and after the break and extrapolating these fits to the breaking point or by simply averaging a few data points of the force before and after the event respectively. Figure 3.4A schematically shows, for a single force trace, how this is carried out and the resulting determined forces of a typical  $G_0$  junction rupture are shown as green markers in Figure 3.5. The resulting histogram of 22000  $G_0$  breaking events (selected from the 46500 traces) is shown in Figure 3.4B. The data has been collected over 19 separate experiments, each involving separate calibration of the cantilever force constant as detailed in chapter 2. Our algorithm fails to determine the breaking force for a significant fraction of the measured traces resulting in this high selectivity, primarily because of the signal to noise limitations on the force measurements. Nonetheless, this procedure shows that the most probable breaking force measured over a statistically large data set is 1.5 nN, in excellent agreement with the theoretical value of 1.4-1.6 nN<sup>29,115</sup> and experimental value of 1.5 nN<sup>113,115</sup> from literature and supports the validity of our measurements, cantilever calibration, and analysis methods. Although this force analysis method works well for larger breaking forces such as the Au-Au breaking force, it is biased towards larger forces which are easier to determine on a trace by trace basis. Since two line sections have to be fit for each force trace, this method introduces larger uncertainty for junctions with smaller signal to noise ratio.

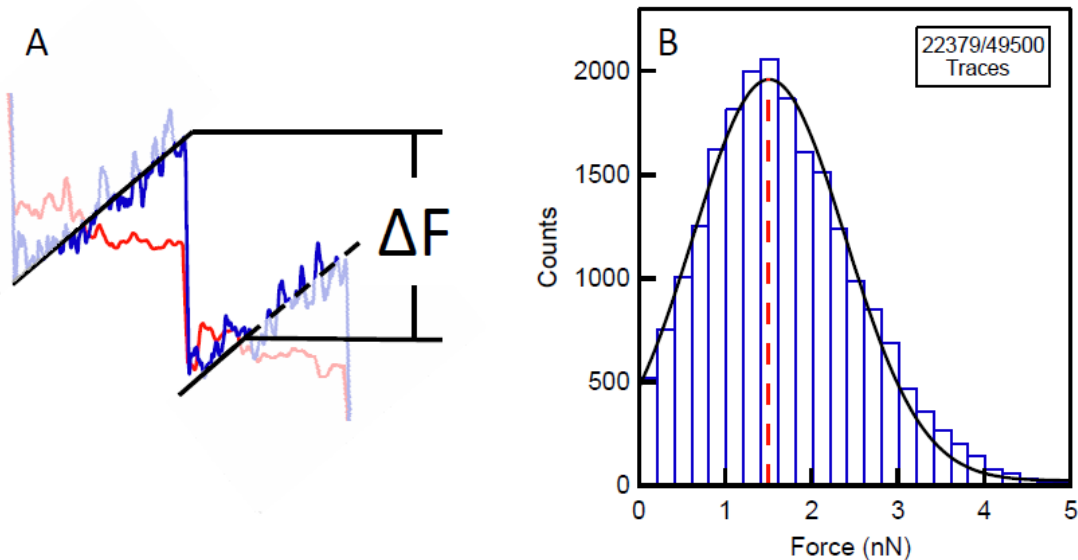


Figure 3.4 (A) Schematic illustrating how bond rupture force is determined on a trace-by-trace basis for the traditional force analysis method. (B) Histogram of  $G_0$  bond-rupture force determined for 22000 traces selected from 49500 traces. A Gaussian fit is shown, and force peak is at 1.5nN.

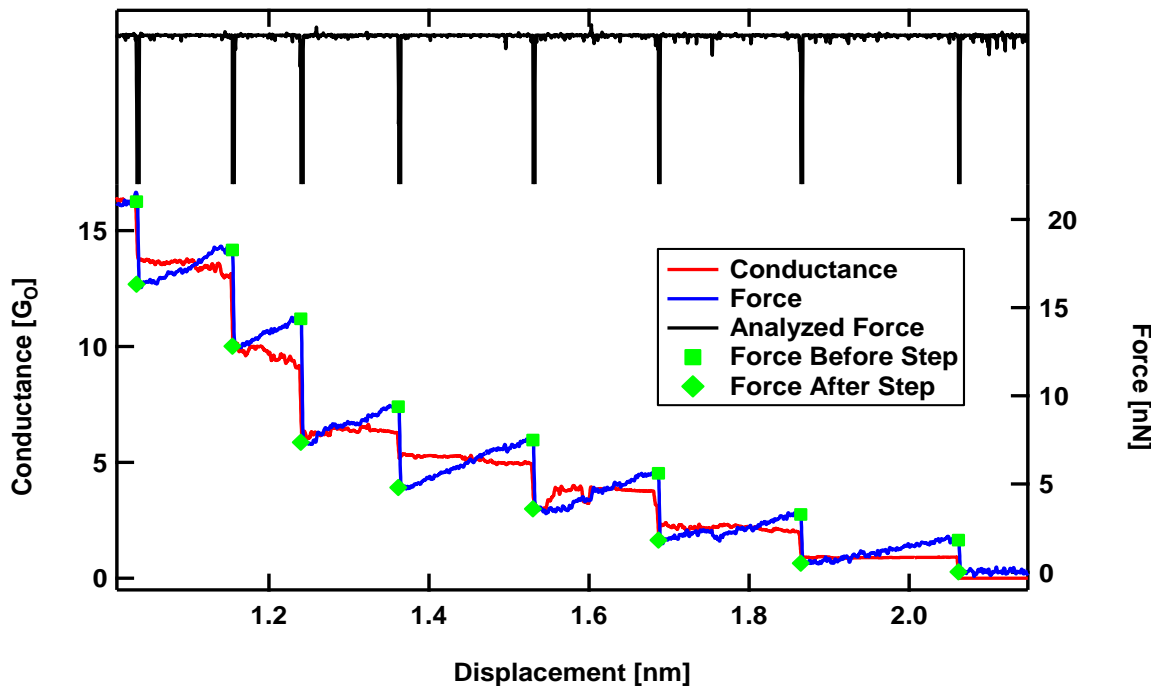


Figure 3.5 Illustration of the force based event recognition procedure in combination with a trace-by-trace force evaluation as applied to a typical gold junction evolution, including the breaking of a single atomic gold contact. The black trace is a manipulated force trace used to identify the force features. The green markers indicate the determined force values before (squares) and after (diamonds) the breaking event.

With the introduction of the updated optical system our force resolution has increased significantly so that individual force event recognition becomes easier experimentally. This is important if junction parameters such as stiffness, breaking force, and conductance want to be analyzed on a trace by trace basis in order to possibly distinguish between different crystallographic orientations or geometric molecule arrangements for example. For data collected using the improved set-up, we can determine rupture forces and junction stiffnesses using a more precise fitting method as follows: For a given force event, we fit a three-line segment around the rupture location as shown in Figure 3.6. We select the fit with the lowest error from 400 different fit combinations where the end of line segment one (X1) and beginning of line segment 3 (X2) are varied in 20 incremental steps of 0.0006 nm along the displacement axis. This iterative fitting mechanism is more accurate in determining the location of rupture events which are often not correctly identified within a distance of 0.004 nm. In order to further eliminate fitting inaccuracies we also exclude traces for which the end of the first line segment (X1) occurs after the start of the third line segment (X2) and traces for which the middle segment has a positive slope. Finally the numerical value of each rupture is taken as the difference between the value of the fit at X1 and X2.

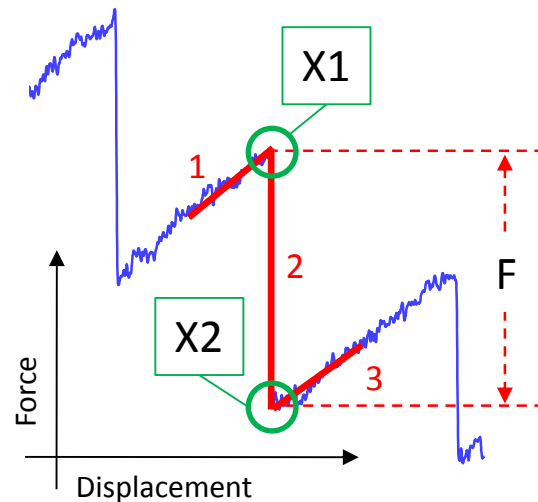


Figure 3.6 A schematic of the iterative fitting procedure. 400 three-line-segment curves (1,2,3) are fit to the force event by varying X1 and X2 incrementally. The best fit is chosen by selecting the minimal fitting error.

The peak of a Gaussian fit to the histogram created of thousands of such individual force events gives a statistically most likely breaking force for the particular bond breaking under consideration. This method is much more time consuming but is more accurate. Furthermore, the slope of the first line segment gives the stiffness of the given junction configuration just before the rupture event. Figure 3.7 shows junction stiffnesses obtained in this way for junctions with a conductance of three, two, and one  $G_0$ , which correspond to a single, two and three atom contact. A stiffness of 17.5 N/m, 14 N/m, and 8.5 N/m is determined in agreement with published results.<sup>115-116</sup> These values were corrected to account for the cantilever spring constant in series with the junction stiffness. A more detailed discussion of junction stiffness for gold and molecular junctions, length scale measurements and how they relate to underlying energy potentials is an active area of research and will be the topic of future publications. This thesis focuses

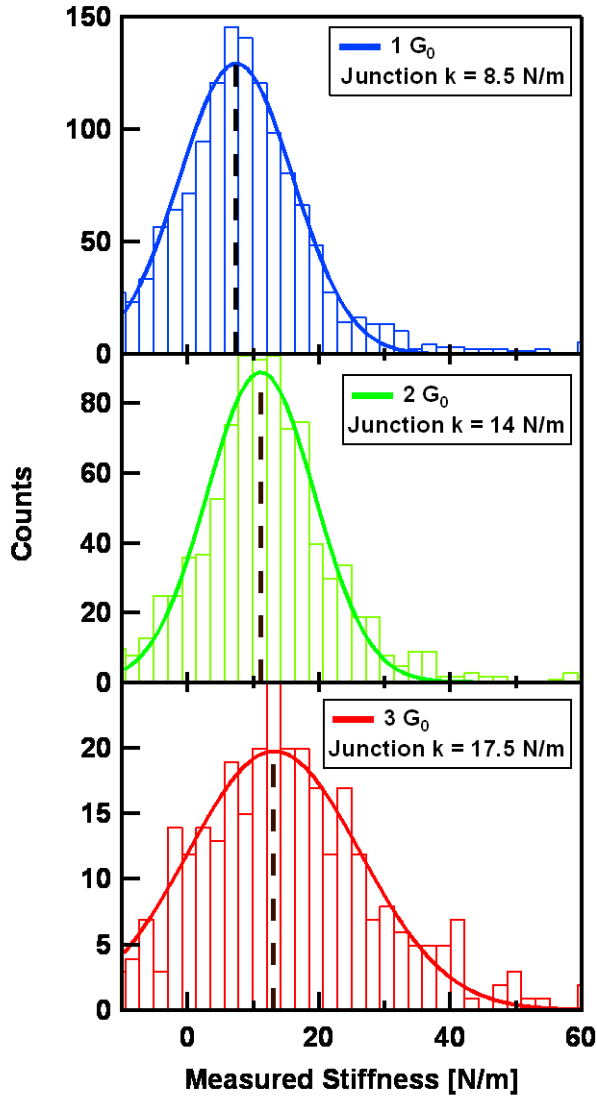


Figure 3.7 Junction stiffness measurements for 1,2,3 $G_0$  obtained with the multi-line fit approach. 1441, 944, and 325 traces have been selected from a set of 2000 gold junctions. A correction to account for the cantilever stiffness in series has been applied.

on the evaluation of breaking force data for a variety of different molecular junctions.

### 3.2d Direct Force Event Identification

Relying on conductance to identify specific events during junction evolution is not always possible. For example, the conductance feature of a given molecule may lie outside of the experimentally measurable conductance range yet some conclusions about junction formation and breaking mechanism are desired. Furthermore, certain linker groups do not show characteristic conductance plateaus but a rather continuous decrease of the conductance as a function of junction elongation. For these cases the identification of all force events within a given conductance or displacement window is an attractive option as measurable quantities such as stiffness and breaking forces may still lead to conclusions about the evolution of the mechanical and hence electronic system.

In force based event recognition all events are identified using force data. The goal is to determine the location of every sharp force event occurring in each trace. This is achieved using a three step algorithm: (1) we subtract, from the raw force trace, a smoothed and laterally offset force trace. This effectively highlights low frequency changes of the force signal. (2) We multiply these by the square of the derivative of the original force trace. (3) The resulting traces has sharp spikes at locations where the original force trace has sharp drops, thus bond rupture events can be identified by finding all spikes above a cutoff determined from the signal noise for each individual trace. Figure 3.5 shows, in black, the trace where all drops are identified for gold point contact. The location of all spikes is noted, and the force and conductance right before and after is determined for each measurement. For example, a single atomic gold-gold chain rupture can be identified by simultaneously requiring the conductance before and after the event to be close to quantum of conductance ( $G_0$ ) and below  $G_0$  respectively. The limitations of this

approach are that small force events are hard to reliably distinguish from the noise background. Since small force events are statistically meaningful when investigating the average breaking force of a particular breaking event, this method may overestimate the average breaking force. It is important to note though that it does not overestimate the force events that are identified. Once a force event is identified, we can determine the magnitude of the force using a Trace-by-Trace or 2D approach as described previously.

### 3.3 Accurate Measurements of Single Gold-Gold Bond Breaking Forces

We have now demonstrated that we have both the experimental and analytical capabilities to determine single bond breaking forces in a statistically meaningful manner. When applied to the single gold bond breaking, the methods are consistent and agree extremely well with theoretical first principles calculations and previous experimental results. This gold breaking force measurement can serve as an ideal benchmark to compare magnitudes of other breaking forces such as molecular breaking forces. However, we have observed that certain care has to be taken when determining the gold breaking force, and in extension, molecular breaking forces that are discussed later. First, it is important to note that the range of observed breaking forces (see Figure 3.4B) is rather large. Evidently, even a single gold-gold bond which breaks with an average force of 1.5 nN can break frequently under measured forces as high as 3 nN. This point is important, because it emphasizes the need for a statistically representative sample set, which may not be given if only tens of events are observed. Furthermore, it also emphasizes the care that must be taken when selecting a subset of all traces for inclusion in the determination of an averaged breaking force. As a guideline, aggressive selection based on force magnitude, junction stiffness, conductance plateau length, and conductance plateau slope should be approached with

care. We did not find a correlation between the magnitude of each force event and these junction parameters and hence an identification and separation of distinct junctions was not possible. A further attempt based on the relation of these parameters to the underlying bonding potential may prove more successful in the future.

A second parameter that can critically influence the measured breaking force of the gold-gold bond is the applied voltage across the junction. A high applied voltage can result in significant capacitance between the tip and substrate. As a result of the buildup of charge immediately after the single atomic gold contact and the resulting conductance drop of the junction by orders of magnitude, the cantilever feels an attractive force towards the sample. Immediately after the conductance breaks the force measured by the cantilever is therefore a convolution of the attractive capacitive effect and the relaxation of the cantilever and electrode due to bond rupture. Figure 3.8 shows a 2D force histogram and a corresponding average force profile constructed from about 1000 traces taken at biases of 500 and 750 mV and indicates the capacitive effect on the measured force. This effect depends sensitively on the details of the tip structure. We find that with plateau tip cantilevers, capacitive effects are not significant at biases under 100 mV. Capacitive effects in conductive AFM measurements have been observed in the literature and theoretical calculations on the impact of cantilever shape have been investigated.<sup>133</sup> All measurements discussed in this thesis have been made at low voltages to minimize capacitive effects. This problem does limit the ability to measure low conducting molecules as increasing the current signal through an increase in applied voltage is not an option.

### 3.4 Summary

In this chapter we presented methods to analyze simultaneously acquired force and conductance measurements. We see that we can determine rupture forces as well as junction stiffness using force data. Conductance is often used as a clear finger print of a given structural rearrangement and we have developed both a trace-by-trace and 2D histogram method to analyze force events identified by conductance. An alternative analysis method that relies solely on force data was also presented. Both force analysis methods have provided a first statistically representative measurement of the single gold-gold bond breaking force and agree very well with the experimental and theoretical published results. We see that the averaged single gold breaking forces are constant and hence can serve as a force standard at this atomic scale.

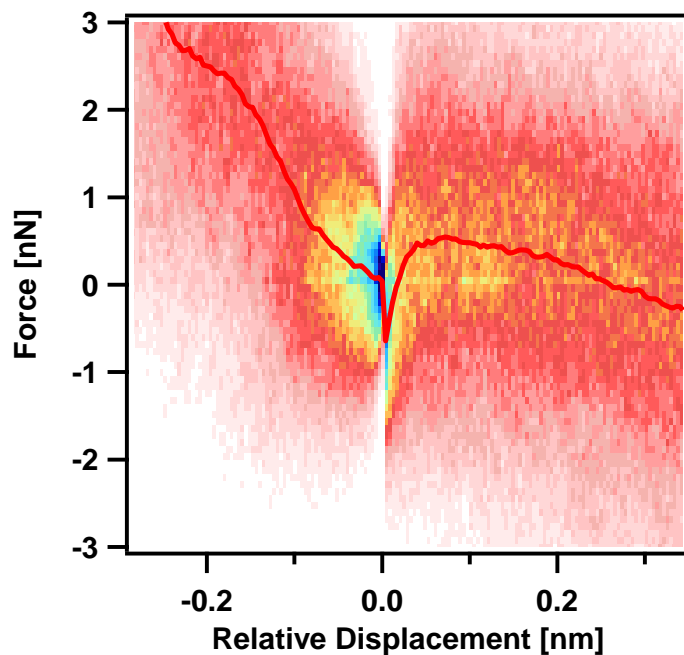


Figure 3.8 2D force histogram with an averaged force profile indicating the effects of capacitive forces at high applied biases. This plot consists of about 1000 individual traces taken at an applied voltage between 500 and 750 mV.

# Chapter 4 Single Molecule Bond Rupture Forces: Influence of Molecular Backbone

## 4.1 Introduction and Motivation

Understanding physical properties of single molecule junctions is of fundamental importance to nanoscale electronics<sup>134</sup>. While electrical and thermal properties have been probed in a variety of organic molecules bound to metal electrodes<sup>3,32,135-139</sup>, measurements of rupture forces of single metal-molecule-metal junctions are new<sup>140-141</sup>, and simple predictions relating the mechanics of these junctions to the backbone chemistry have not been tested. In this chapter we use the experimental setup described in Chapter 2 to simultaneously measure force and conductance data for single gold metal-molecule-metal junctions. The evaluation procedures discussed in Chapter 3 will yield averaged single molecule breaking forces for a series of molecules terminated with amine and pyridine linkers. For all these molecules studied, single molecule junctions rupture at the Au-N bond. Selective binding of the linker group allows us to correlate the N-Au bond-rupture force to the molecular backbone and we find that the rupture force ranges from 0.8 nN for 4,4' bipyridine to 0.5 nN in 1,4 diaminobenzene. These experimental results are in excellent quantitative agreement with density functional theory based adiabatic molecular junction elongation and rupture calculations.

## 4.2 Experimental Details

The experimental details follow the discussions in previous chapters. For each measurement, a gold point-contact with a set conductance larger than  $5G_0$  is formed between the

substrate and cantilever. This is to ensure that the Au/molecule/Au junction from the previous measurement was completely destroyed and a fresh junction is formed for every measurement. The junction is then pulled apart at a constant velocity of 18 nm/s and broken in an environment of molecules while conductance and force are measured as a function of sample displacement. This process is repeated thousands of times to obtain large data sets of conductance and simultaneously acquired force traces. Before adding a molecule to the substrate, at least 1000 traces are collected to ensure that no contamination is present in the set-up. When measurements are carried out in an environment of molecules an additional conductance step is frequently observed at a molecule dependent conductance value below  $1 G_0$  along with an additional abrupt change in the force trace. The full trace of force versus elongation presents a rich data set describing the mechanical evolution of these junctions under stress. In this study, we focus on the force associated with the breaking of a gold-molecule-gold junction, but we also determine single atom contact breaking force which we use as a calibration standard. For this particular study, all molecules were obtained from Sigma-Aldrich and were used without further purification. Conductance is determined by measuring current through the junction at a constant applied bias of 25 mV for short molecules and 75 mV for 1,6-hexanediamine and for 4,4' bipyridine. Molecules are evaporated onto the Au-on-mica substrates, and for each molecule, over 30,000 conductance and simultaneously acquired force traces are collected with multiple tip/sample pairs. Both conductance and force data is then evaluated by identifying the breaking event using conductance data. The conductance and force data is then evaluated statistically using the 2D histogram method. The AFM is operated in ambient conditions at room temperature

### 4.3 Amine and Pyridine Linked Molecules: Force and Conductance Data

Table 4.1 lists the names and structures of the four molecules studied. Three are amine ( $\text{NH}_2$ ) terminated molecules, 1,4-benzenediamine, 1,4-butanediamine, and 1,6-hexanediamine, which bind selectively to under-coordinated gold through a donor acceptor bond between the terminal N and Au atom.<sup>142</sup> The fourth is 4,4' Bipyridine, which also binds through an N-Au donor-acceptor bond.<sup>77</sup>

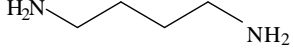
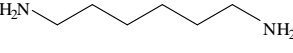
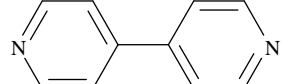
Molecule	Structure	Conductance ( $G_0$ )	Bond Rupture Force (nN)	
			Experiment	Theory
1,4 Benzene-diamine		$6.2 \times 10^{-3}$	$0.53 \pm 0.09$	0.46
1,4 Butane-diamine		$9.0 \times 10^{-4}$	$0.69 \pm 0.06$	0.84
1,6 Hexane-diamine		$1.1 \times 10^{-4}$	$0.62 \pm 0.09$	N/A
4,4' Bipyridine		$1.0 \times 10^{-4}$	$0.80 \pm 0.08$	1.00

Table 4. 1 List of molecules and their structure considered to investigate the effect of molecular backbone on the rupture force of single molecule junctions. The experimentally determined conductance is provided and the measured and calculated rupture forces are provided for comparison.

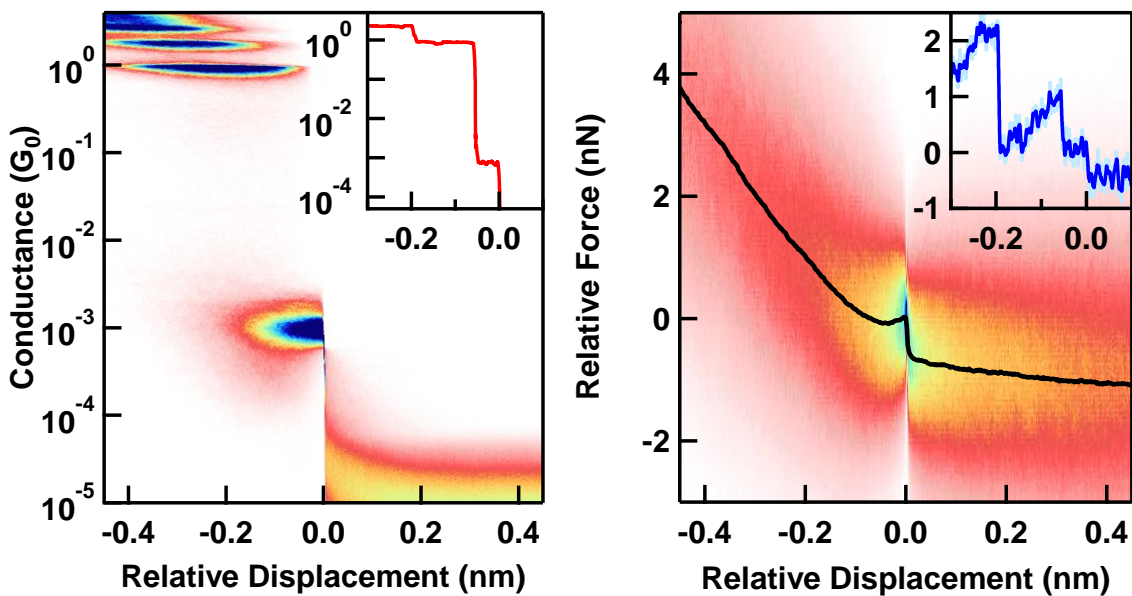


Figure 4.1 (A) (a) Two-dimensional conductance histogram of 1,4-butanediamine data constructed from over 10000 traces with a molecular conductance step. The conductance data is presented on a log scale. Features representing a sequence of gold contacts clearly appear at integer multiples of  $G_0$ . A molecular signature can be clearly seen at  $1 \times 10^{-3} G_0$ . Inset: A sample conductance trace showing a  $G_0$  and molecular plateau with zero displacement set to the end of the molecular plateau. (b) The two-dimensional force histogram for 1,4-diaminobutane is constructed from the set of simultaneously acquired force traces used to construct the conductance histogram. The average force profile (black curve) shows a clear drop at zero-displacement, which gives a statistically determined breaking force for the N-Au bond of 0.69 nN. Inset: The simultaneously acquired force trace aligned after the molecular step is shown both unsmoothed (light blue) and smoothed (dark blue). Force events corresponding to a  $G_0$  rupture and molecular breaking are clearly visible.

Figure 4.1A shows a 2D conductance histogram for 1,4-butanediamine where the origin in the displacement axis is set at the end of the molecular conductance step. Logarithmic bins for the conductance (y-) axis and linear bins for the displacement (x-) axis are chosen for image clarity. Insets of Figure 4.1A and B show conductance and simultaneous force data for one particular junction breaking event. Approximately 30% of the 31000 measured traces showed evidence of full single molecule junction formation, and contribute to the histogram. A clear peak is seen in the conductance histogram at  $9 \times 10^{-4} G_0$ , which gives us the most probable conductance of a gold-1,4-butanediamine-gold junction. This peak extends over a displacement

of about 0.15nm, indicating that molecular junctions can be elongate over this distance prior to the final rupture. Conductance histograms for measurements with all other molecules are shown in Figure 4.2A, Figure 4.3A, and Figure 4.4A. Of the four molecules measured, the three diamines show a single conductance peak due to the selective binding of the NH<sub>2</sub> linker to undercoordinated gold atoms.<sup>142-143</sup> 4,4' Bipyridine shows two conductance peaks (a high-G and a low-G peak) which occur at distinct junction elongation distances. In this work, we probe the rupture from the low-G peak, which corresponds to a geometry where the molecule bridges the two gold electrodes vertically.<sup>77</sup> All conductance peak positions for these four molecules are close to previously published data (see Table 1) collected in solution using the scanning tunneling microscope-based break junction technique.<sup>77,143</sup> This validates our measurement set-up and the molecule deposition technique. Furthermore, the clear conductance signature seen for all these molecules allows us to measure these specific single gold-molecule-gold junction rupture events unambiguously.

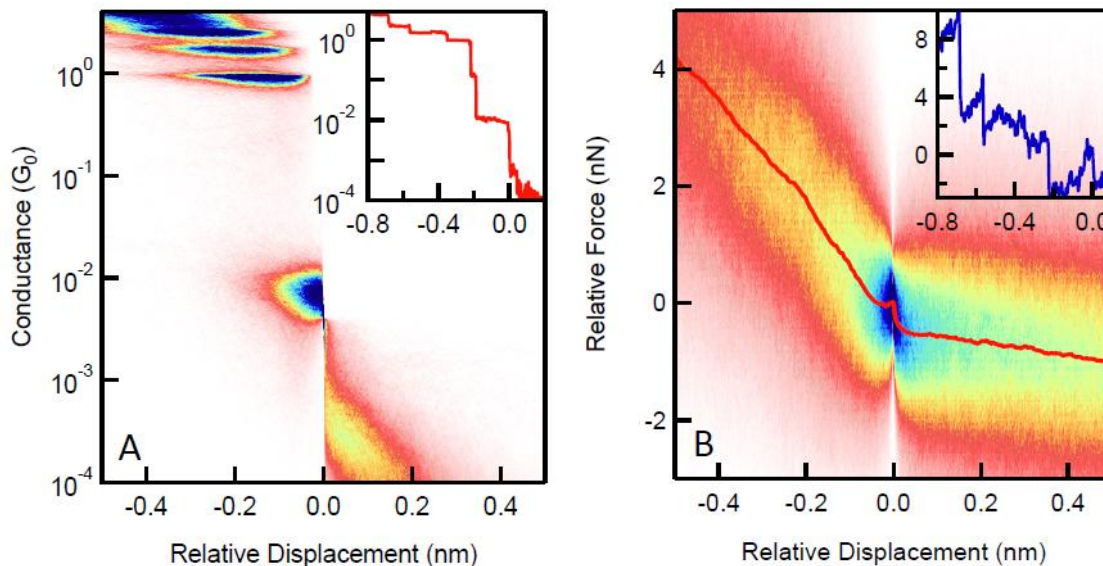


Figure 4.2 (A) Two-dimensional conductance and (B) force histograms for 1,4 benzenediamine. Histograms are for 7345 traces selected from 58000 traces. The insets show a typical molecular conductance and force trace respectively aligned after the molecular plateau. The red trace in (B) indicates the average force profile.

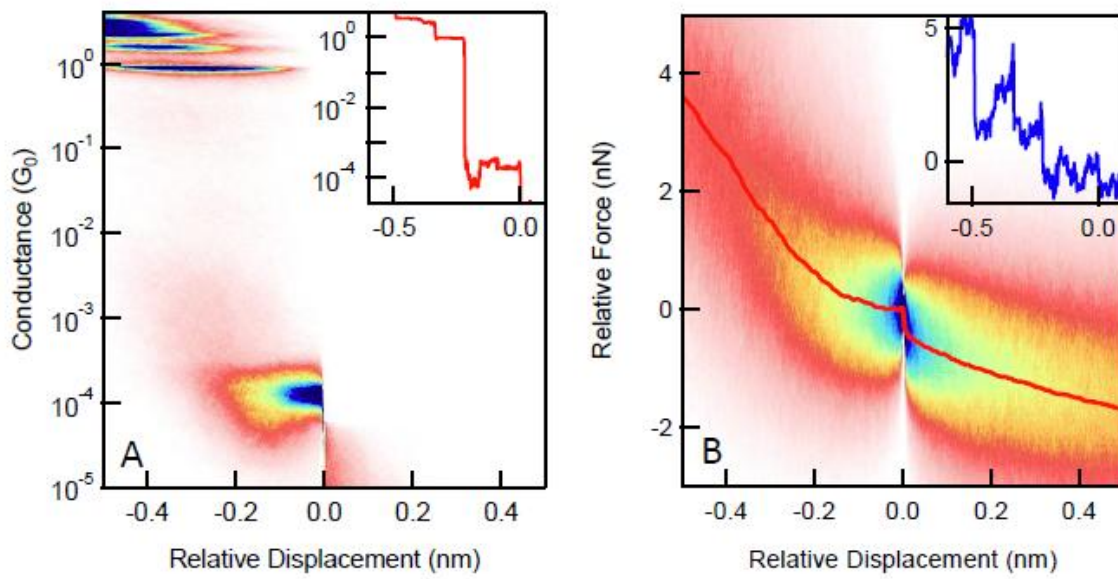


Figure 4.3 (A) Two-dimensional conductance and (B) force histograms for 1,6 hexanediamine. Histograms are for 6431 traces selected from 34000 traces. The insets show a typical molecular conductance and force trace respectively aligned after the molecular plateau. The red trace in (B) indicates the average force profile.

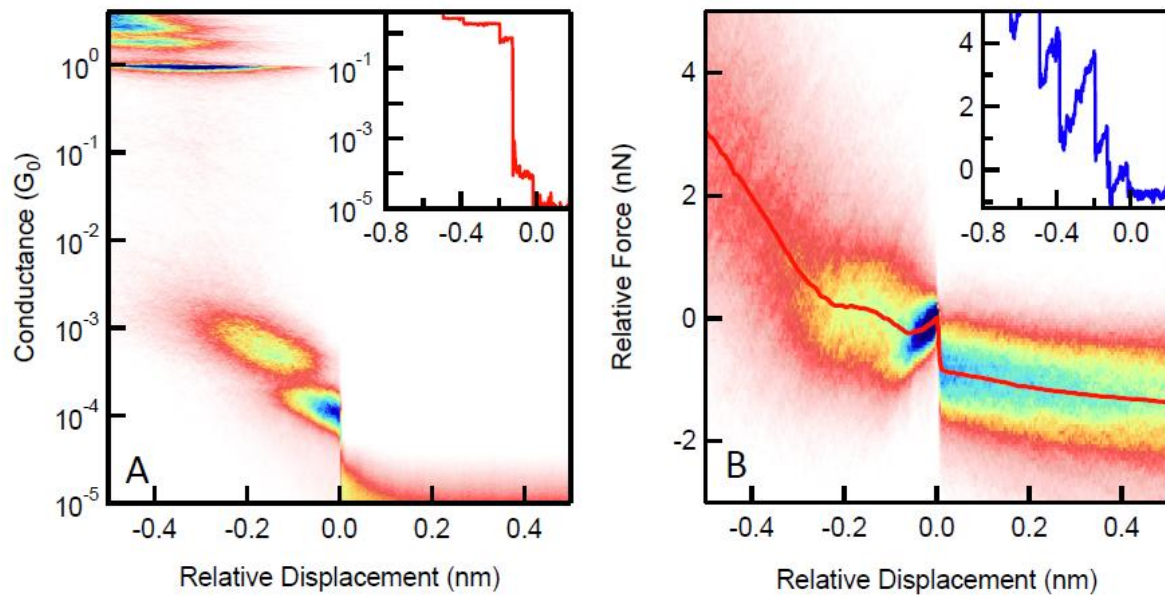


Figure 4.4 (A) Two-dimensional conductance and (B) force histograms for 4,4' bipyridine for one tip/sample pair. Histograms are for 3423 traces selected from 11000 traces. The insets show a typical molecular conductance and force trace respectively aligned after the molecular plateau. The red trace in (B) indicates the average force profile.

Figure 4.1B-Figure 4.4B show the corresponding 2D force histogram created from the force traces acquired simultaneously with the conductance traces used to create the respective 2D conductance histograms. Since the origin in the displacement axis is set at the point where the molecular conductance step ends, the drop in the force profile, shown overlaid on the 2D histogram, corresponds to the average force required to rupture the gold-molecule-gold junction. This force is determined to be  $0.69 \text{ nN} \pm 0.06 \text{ nN}$  for 1,4- butanediamine for example, where the error bar represents the standard deviation of the measured force from 5 different tip/sample pairs. This force is significantly smaller than the force required to break the gold-gold bond. Although the conductance steps extended over 0.15 nm as seen in Figure 4.2A, we see no signature in the force histogram over this range that would indicate statistically reproducible force events at a well defined displacement prior to junction rupture. However, individual traces do show additional force features indicating that during the junction elongation process, bond breakage or other atomic rearrangements do occur<sup>144</sup>. The case of 4,4' Bipyridine is different in that it presents two distinct conductance peaks. Conductance drops from the high state to a low state during junction elongation. We see in Figure 4.4B that even the 2D force histogram aligned at the break of the low conductance state to an open junction does show a small peak-like feature in the averaged force profile at -0.2 displacement. This is equivalent to saying that another force event occurs shortly before the break from a vertical junction frequently. This is attributed to the transition from the high conducting to the low conducting state and we can conclude that this transition evidently occurs with some mechanical rearrangements in the junction with a finite force that can be measured by our setup. These force measurements thus provide new insight into the junction evolution.

In Table 1, we show bond rupture forces determined from 2D-force histograms for all four molecules considered here. We see that in all cases, the gold-molecule-gold junction ruptures at a force smaller than that of a gold-gold bond, indicating that rupture occurs at the Au-N donor acceptor bonds consistent with earlier work.<sup>141</sup> Comparing the measured rupture forces of the different molecules, we see first that for the two alkanes with 4 and 6 carbons in the backbone, the rupture forces are very similar. Additionally, we see that the force required to break the N-Au bond in the conjugated molecule, 1,4-benzenediamine, is considerably smaller than in 1,4-butanediamine and 1,6-hexanediamine, which are fully saturated. Finally we can also conclude that the measured average breaking force of 4,4' Bipyridine is larger than for any of the other three amine linked molecules.

#### 4.4 Theoretical Calculations of Bond Rupture Forces

To better understand these results, we have carried out density functional theory (DFT) based calculations simulating the junction elongation and rupture process<sup>145-146</sup> for three of the four molecules studied here, excluding the longer alkane. The Au tip and surface were modeled with Au pyramids (20 atoms each) with (111) surfaces. The tip atom on the top pyramid was moved to an adatom site on one facet resulting in a blunt, three atom tip. These model structures were previously used to analyze extended elongation trajectories<sup>144</sup>. Here we focused on the portion of the trajectory where the junction was elongated from a local energy minimum through the inflection point and finally probed the dissociated structure after one bond ruptures. The back layer of Au atoms in each pyramid was held fixed with a bulk lattice parameter 4.08 Å. All other degrees of freedom were relaxed until all forces were less than 0.005-0.01 eV/Å for each junction structure. The junction was elongated in steps of 0.1 Å by increasing the separation

between the pyramids along the z direction and then fully optimizing the geometry. As the point of maximum force was approached for the 4,4' bipyridine junction, competing structures were examined to identify that with the lowest energy, while in the other junctions the lowest energy structure emerged naturally at each step. Density functional theory total energy calculations and geometry optimization were performed with the VASP package<sup>147</sup>, using the projector augmented wave approach which naturally included scalar relativistic effects for gold<sup>148-149</sup> and the generalized gradient approximation (GGA) of Perdew, Burke and Ernzerhof (PBE)<sup>150</sup> for the exchange-correlation density functional. The model junction was placed in a hexagonal supercell ( $a=2.0\text{nm}$ ,  $c=3.5\text{nm}$ ) and the basis set for solution of the Kohn-Sham equations was determined by a 400 eV cutoff. The accuracy of the GGA for calculation of donor-acceptor binding energy, such as the amine-Au bond here, has been tested in specific examples. Comparison to carefully converged coupled-cluster calculations for the Au-NH<sub>3</sub> molecular complex showed that GGA calculations underestimate the binding energy by about 0.11-0.13 eV<sup>151</sup>. Analyses of ammonia and pyridine adsorption on the Au (111) surface are also consistent with at least an 0.1 eV underestimate<sup>152-153</sup>. The present calculations with a well-converged basis set gave a Au-N bond energy that was about 0.2 eV smaller than that obtained previously with the def2-SVP basis in TurboMole<sup>144</sup>, the latter being a less complete basis and exhibiting some basis set superposition error in the binding energy.

Total energy and applied force computed from adiabatic junction elongation trajectories for each molecule are shown in Figure 4.5A and B. All three junctions were studied using the same Au structure and link attachment points to highlight the chemical trends, as illustrated in Figure 4.5C. We see that in all cases, the junction ruptures at the Au-N bond, as observed in the experiment. The maximum calculated sustained force determined for each molecule is reported

in Table 1. We see that 1,4 benzenediamine can sustain the smallest force, while 4,4' bipyridine the largest, in good quantitative agreement with the measured trends, and for 4,4' bipyridine in good agreement with earlier DFT based studies<sup>154</sup>.

These calculated forces are the largest sustainable breaking forces calculated from a *single* adiabatic junction elongation trajectory. However, previous studies<sup>144</sup> showed that small changes in junction structure (attachment point or molecule orientation) can lead to ~0.1-0.2 nN variations in the maximum sustained force. More generally, we expect that diverse junction structures are sampled in the experiments, including variations in Au-N bond orientation in the junction and relative to the pulling direction (Figure 4.5D).

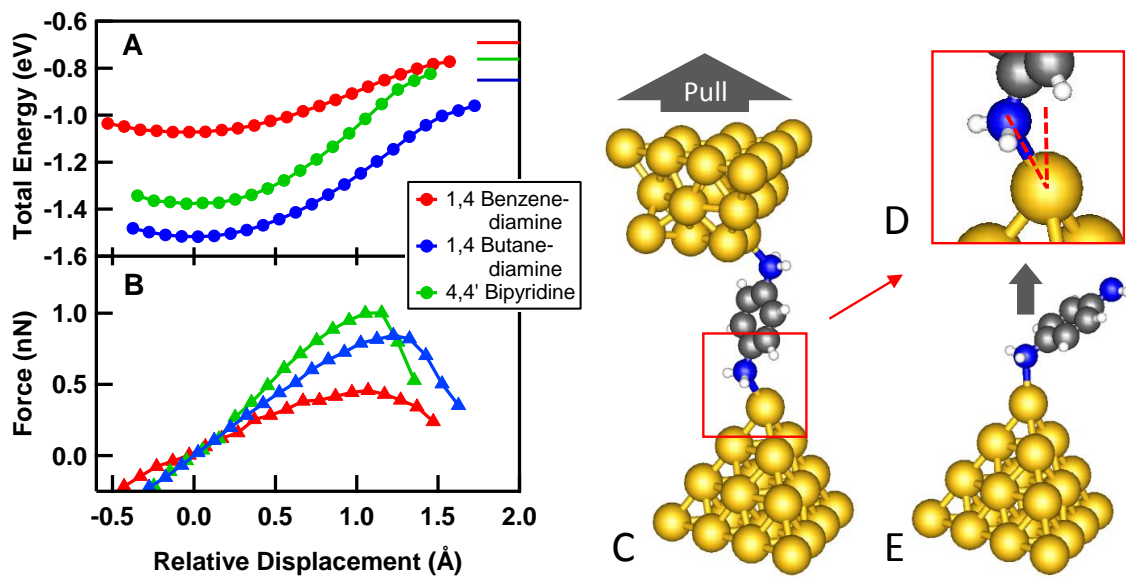


Figure 4.5 (a) Calculated total energy curves from adiabatic trajectories for 1,4-benzenediamine (red), 1,4-butanediamine (blue), and 4,4' bipyridine (green) shown as a function of displacement. Bars shown at right indicate the asymptotic values. (b) Calculated applied force curves for the same molecules shown against displacement display the same trend as the experimental results. (c) Junction structure showing a 1,4-benzenediamine junction at 0.1 nm elongation relative to the local energy minimum. (d) Zoom in of the Au-N bond indicating bond angle with respect to pulling direction. (e) Sample structure used to investigate a single Au-N bond force profile for 1,4-benzenediamine bound to a gold electrode with bond aligned to the pulling direction.

To probe the importance of the bond orientation on the maximum sustained force, we also studied the elongation of a single N-Au bond for a well-aligned model structure, as illustrated for the 1,4 benzenediamine case in Figure 4.5E. Stretching the N-Au bond by constraining the position of the bound N and the back plane of the Au pyramid structure resulted in a calculated maximum sustained force of 0.83, 1.09 and 1.12 nN for 1,4 benzenediamine, 1,4 butanediamine and 4,4’bipyridine respectively. The full trajectories for energy and force for the three cases can be seen in Figure 4.6A and B respectively. Thus the force required to rupture the Au-N bond depends on the backbone chemistry. In 1,4-benzenediamine, the N lone-pair is partly delocalized into the  $\pi$ -system, which weakens the N-Au donor-acceptor bond. In saturated molecules, or in pyridines, where the lone-pair is orthogonal to the  $\pi$ -system, the lone-pair is fully available for binding, resulting in larger rupture forces. However, the differences between 1,4 butanediamine and 4,4’bipyridine are more subtle. While an  $sp^3$  derived lone pair of 1,4 butanediamine is more sharply directed in space than an  $sp^2$  derived lone pair in 4,4’bipyridine, the availability of the  $\pi$ -space on the pyridine contributes to the binding<sup>155-156</sup>. As a consequence, the binding energies and maximum sustained forces are similar.

Comparing the single Au-N bond rupture forces listed above with those for the junctions listed in Table 1, we see that the impact of Au-N bond orientation (Figure 4.5D) is most prominent for 1,4 benzenediamine and least important for 4,4’bipyridine. In 4,4’bipyridine, the N lone-pair orbital is oriented in the plane of the rings allowing for a vertical molecule geometry<sup>157</sup>, thus the calculations for the junction and the bond are very close. For 1,4 butanediamine and 1,4 benzenediamine junctions, which naturally result in geometries where the backbone and the N-Au bond are tilted, the component of the force projected on the junction elongation direction (vertical) will be reduced by the direction cosine. This will be more

significant for 1,4 benzenediamine and 1,4 butanediamine than for 4,4' bipyridine. Indeed, we find that although Au-N *bond* rupture forces for 4,4' bipyridine and 1,4 butanediamine are very similar, the experiment and trajectory based calculated show that 1,4 butanediamine junctions rupture at smaller forces.

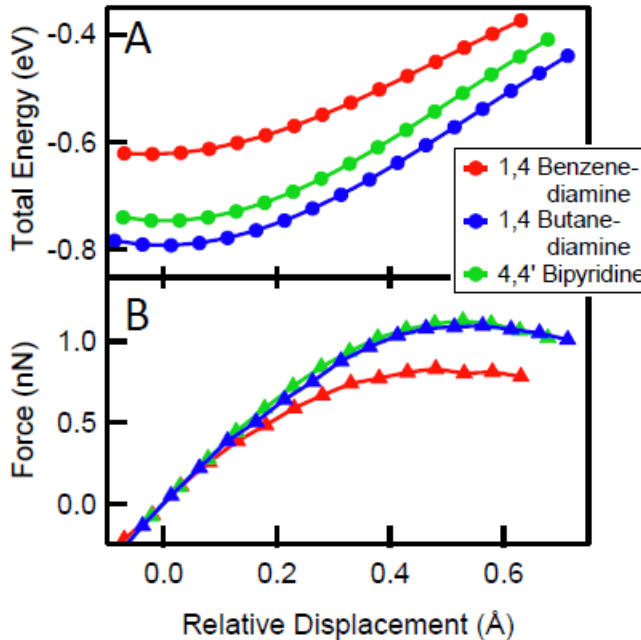


Figure 4.6 (A) Calculated total energy and (B) force curves from adiabatic trajectories for a well-aligned model structure for 1,4-benzenediamine (red), 1,4-butanediamine (blue), and 4,4' bipyridine (green) shown as a function of displacement. Initial geometry as illustrated in Figure 4E in the text, with the N-Au bond aligned to vertical. Displacement controlled by fixing the position of the back plane of Au atoms in the cluster modeling the electrode and the N atom bonded to the Au tip atom.

## 4.5 Conclusion

In summary, we successfully applied our experimental and analytical approaches from Chapters 2 and 3 to measure the average breaking force for amine and pyridine terminated molecules. These forces were determined through analysis of thousands of individual measurements and present a first and statistically robust determination of rupture forces of amine

and pyridine linked single molecule break junctions. Contrasting these measurements to the force required to break a single gold-gold bond as determined in Chapter 3, we can conclude that both the amine and pyridine linked molecules break at the gold-nitrogen bond during the final stages of the junction evolution. By comparison of the breaking forces for 1,4-benzenediamine, 1,4-butanediamine, 1,6-hexanediamine, and 4,4' bipyridine we show that the electronic structure of the molecular backbone alters N-Au bond strengths considerably. This can be seen both in the calculations and in the measurements: 1,4-benzenediamine binds most weakly to Au atoms, while the pyridine-gold bond exhibits the largest breaking force amongst the molecules considered here. These measurements demonstrated the significant insight that force measurements can provide into the evolution of a gold-molecule-gold junction. While this Chapter focused on the effects of the molecular backbone on the breaking force of identical linker atoms, we also expect the nature of the linker to play a significant role. The investigation of this will be the focus of the next chapter.

# Chapter 5 Linker Dependent Bond Rupture Force Measurements in Single - Molecule Junctions

## 5.1 Introduction and Motivation

Probing the relation between mechanical and electronic properties of single molecule circuits provides a deeper understanding of the structure-conductance relation in these systems. Here, we use a modified conducting atomic force microscope to simultaneously probe the conductance of a single molecule junction and the force required to rupture the junction. We use alkanes terminated with four different chemical link groups which vary in binding strength and mechanism to the gold electrodes. We find that molecular junctions with amine, methylsulfide and diphenylphosphine terminated molecules show clear conductance signatures and rupture at a force that is significantly smaller than the 1.4 nN force required to rupture the single-atomic gold contact. In contrast, measurements with a thiol terminated alkane which can bind covalently to the gold electrode, show conductance and force features unlike that of the other molecules studied. Specifically, we find that in these junctions the strong Au-S bond can cause structural rearrangements in the electrodes which are accompanied by conductance changes. While one might expect these junctions to rupture at a force around 1.4 nN, equivalent to that of the pristine single-atom gold contacts, our experiments show that on smaller average they rupture at a smaller force.

## 5.2 Experimental Details

We use a modified conductive atomic force microscope (AFM) to investigate the breaking mechanism of single molecule junctions formed with different linker groups. The experimental setup and analytical procedures have been described in detail in Chapter 2 and Chapter 3. Briefly, a gold coated cantilever and a gold-on-mica substrate are repeatedly brought in and out of contact using a high resolution piezoelectric positioner at a velocity of about 18 nm/s. Conductance is measured across the tip/sample junction at constant bias of 25mV. Force is measured simultaneously by monitoring the deflection of a laser focused on the back of the cantilever. In the absence of molecules clean Au-Au point-contacts are formed and broken. A conductance trace (Figure 5.1A) shows typical stepwise decrease in conductance as a function of displacement. The simultaneously measured force traces show a typical saw tooth pattern attributed to reversible (elastic) and irreversible (plastic) deformations during conductance

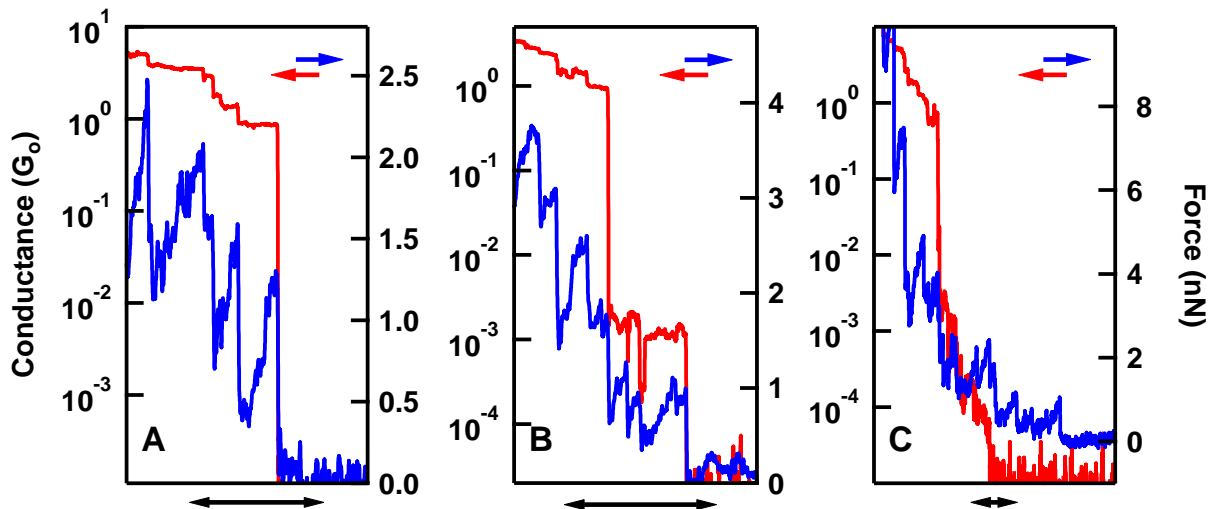


Figure 5.1 Sample conductance (red) and force (blue) traces for gold only (left), C4SMe (middle), and C4SH (right). All three traces exhibit characteristic gold features above  $1G_0$  and molecular signatures below for the case of C4SMe and C4SH.

plateaus and drops respectively.<sup>101</sup> When Au-point contacts are broken in the presence of

molecules, additional features are seen in the conductance and force traces Figure 5.1B and C). The averaged conductance of a single molecule junction and the force required to rupture this junction can be determined from these simultaneously acquired data with the procedures outline earlier.

### 5.3 Junction Evolution of Molecules with Different Linkers

In this chapter, we investigate how single molecule junction rupture forces correlate with the molecular link chemistry. Since measured rupture forces for the Au-N donor-acceptor bond depend on the molecular backbone,<sup>158</sup> we focus here on measurements of alkane backbones terminated with different linkers. Specifically we compare bond rupture forces in junctions formed with 1,4-butanediamine ( $C_4NH_2$ ), 1,4-bis(methylsulfide) butane ( $C_4SMe$ ), 1,5 bis(diphenylphosphino)-pentane (C5DPP), and 1,4-butanedithiol (C4SH). All these compounds are obtained from commercial sources, and used without further purification. The amine ( $NH_2$ ), methylsulfide ( $SMe$ ), and diphenylphosphine (DPP) linkers bind to gold through a donor-acceptor bond<sup>143,159</sup> while the thiol linker can form a covalent bond with the Au electrodes, displacing the H. In the experiments, the molecules are deposited onto the Au substrate either by evaporation or by addition of a dilute concentration of molecule in the solvent 1,2,4-trichlorobenzene (TCB). Both conductance and force results are independent of the deposition method. Figure 5.1B shows a typical, single conductance (red) and force (blue) measurement for  $C_4SMe$ . In addition to the gold features at and above  $1G_0$  we can now also identify a molecular conductance plateau at around  $10^{-3} G_0$ . In the simultaneously measured force trace, two additional saw-tooth patterns are seen within the step, followed by the final rupture, coinciding with the end of the conductance plateau. This indicates that this single molecule junction is

elongated elastically first, undergoes some structural rearrangements which is followed by junction rupture. Sample conductance and force traces for C4NH<sub>2</sub> and C5DPP have similar features, though conductance plateaus and rupture forces are molecule and linker dependent. In contrast, however, the conductance traces for measurements with C4SH are quite different (Figure 5.1C). We do not see a clear conductance plateau, and multiple saw-tooth events are seen after the single Au point-contact is broken at a range of conductance values, down to the measurement limit of  $2 \times 10^{-5}$  G<sub>0</sub>. We will return to a discussion of this data set later in this chapter.

To determine, with statistical significance, junction conductance and bond rupture forces, we collect thousands of simultaneous conductance and force traces for each molecule on multiple tip/sample pairs. For clean Au, C4NH<sub>2</sub>, C4SMe and C5DPP, these large data sets are analyzed by using a two-dimensional histograms technique for both conductance and force

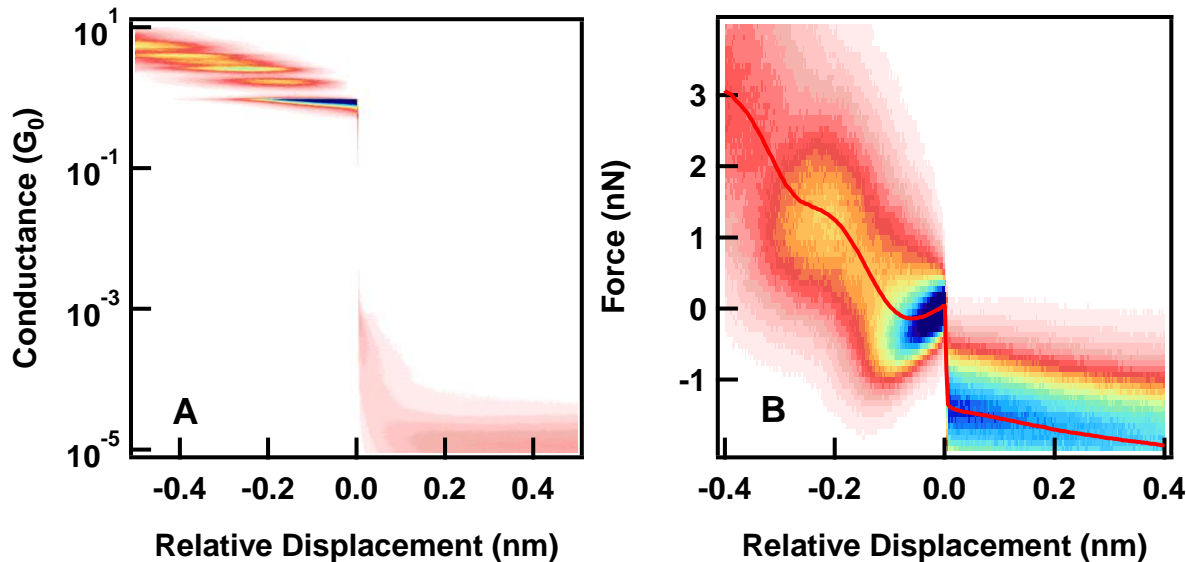


Figure 5.2 (A), 2D conductance histogram (15542 traces) for clean gold traces showing quantized steps above 1<sub>G0</sub> and a clean break to experimental noise. (B) 2D force histogram for the same traces as (A) with the average force profile in black indicating a most probable breaking force for the gold-gold bond of 1.4 nN.

as detailed in previously. Figure 5.2A shows this conductance histogram for 15542 measurements of clean gold showing clear gold conductance quantization without additional features below the atomic gold contact. The rupture force of a  $G_0$  conductance junction is determined from the corresponding force histogram (Figure 5.2B) and measures 1.4 nN, consistent with previous experimental and theoretical results.<sup>113,160-161</sup> The same methodology is applied to evaluate the average junction rupture force for Au-molecule-Au junctions with NH<sub>2</sub>, SMe and DPP linker groups.

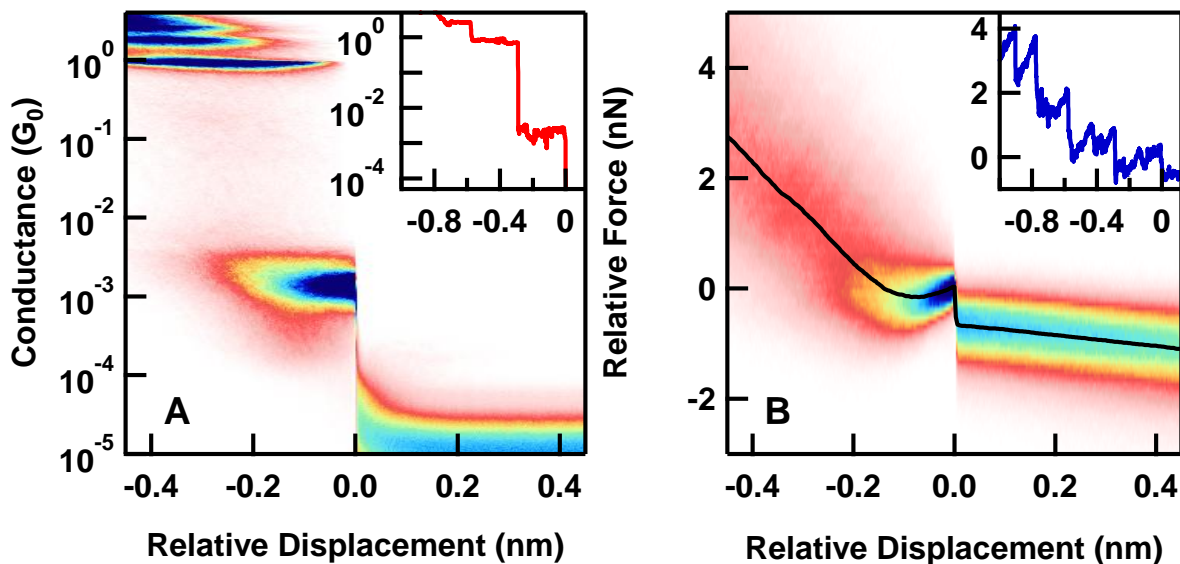


Figure 5.3 (A) 2D conductance histogram for C4SMe constructed from 9774 traces, showing quantized conductance features of the gold breaking and the molecular signature at a conductance value of  $1.4 \times 10^{-3} G_0$ . The inset shows a sample conductance trace. (B) 2D force histogram for the simultaneously acquired force traces with the average force profile in black indicating an average breaking force of 0.66 nN. The inset shows the corresponding force data for the same sample trace.

## 5.4 Statistical Evaluation of Lone-Pair Coupled Alkanes

Figure 5.3A shows a 2D conductance histogram of C4SMe measurements constructed from 9774 traces similar to those shown in Figure 5.1B, and in the inset of Figure 5.3A. The histogram is constructed using logarithm bins along the y-axis and linear bins along the x-axis.

All traces in this histogram are aligned such that zero-displacement is right after the molecular conductance plateau. The subset of measured traces that do not show molecular conductance plateaus are not included in this histogram and thus these histograms are created using 9774 traces out of 27000 traces measured. A prominent peak at  $G_0$  is visible, and is slightly offset from a single, well-defined conductance peak centered at about  $10^{-3} G_0$  along the conductance axis and extending from -0.3 nm to 0 nm along the displacement axis, consistent with previous measurements.<sup>143,159</sup> This validates the deposition method and assures that the subsequent statistical force evaluation of the molecules of interest. Figure 5.4A and Figure 5.5A show the 2D conductance histograms for measurements with C4NH<sub>2</sub> and C5DPP. They are constructed from 3544 and 1694 traces respectively and show similar behavior as the C4SMe case with a molecular conductance feature at the respective values of about  $1 \times 10^{-3}$  and  $6.6 \times 10^{-4} G_0$ .

Figure 5.3B shows the 2D force histogram for C4SMe constructed from the 9774 simultaneously measured force traces corresponding to the conductance traces used to generate the histogram in Figure 5.3A. The force profile (black line) indicates an average breaking force of 0.7 nN for C4SMe. Figure 5.4B and Figure 5.5B show the respective force histograms for C4NH<sub>2</sub> and C5DPP, which show an average breaking force of 0.6 nN and 0.8 nN. For these three linker groups, we see that the bond rupture force is much smaller than that of the 1  $G_0$  contact. It is most likely that these junctions break at the Au-N, Au-S, or the Au-P donor-acceptor bonds respectively.<sup>143-144,158</sup>

Comparing these experimental results with past calculations<sup>143</sup>, we find good agreement for the Au-N and Au-S donor-acceptor bonds. However, the calculated rupture force for the Au-P donor-acceptor bond was found to be around 1.5 nN for dimethylphosphine linker.<sup>143-144</sup> This is significantly larger than what we measure here. Indeed, the calculated rupture forces are

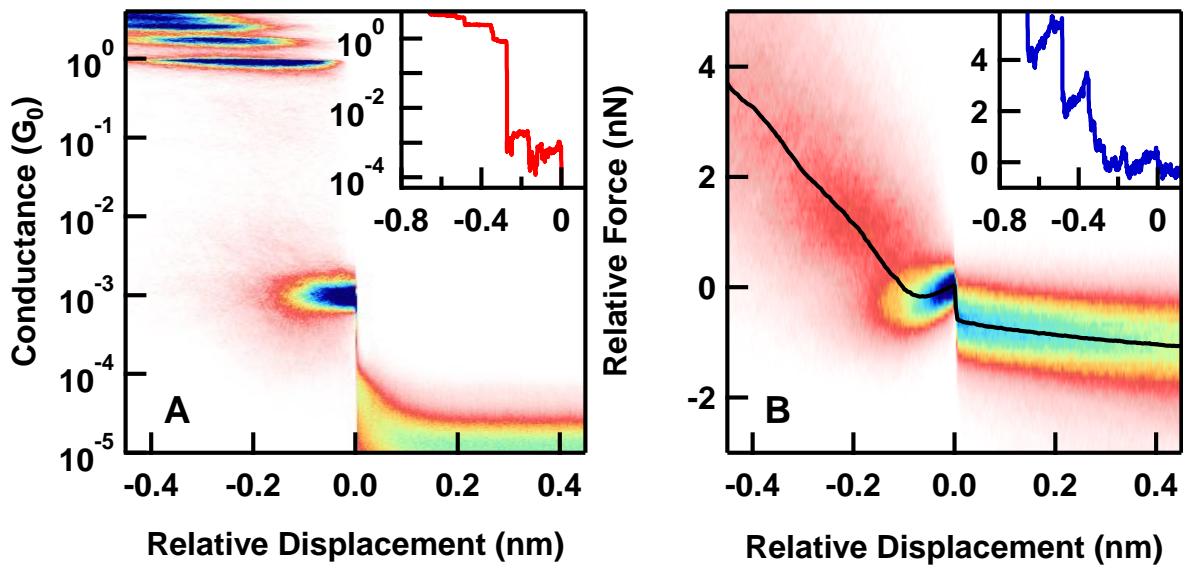


Figure 5.4 (A), 2D conductance histogram (3544 traces) for C4A showing quantized steps above  $1G_0$  and a typical molecular signature at around  $10^{-3} G_0$ . (B) 2D force histogram for the same traces as (A). The average force profile indicates a breaking force of 0.62 nN.

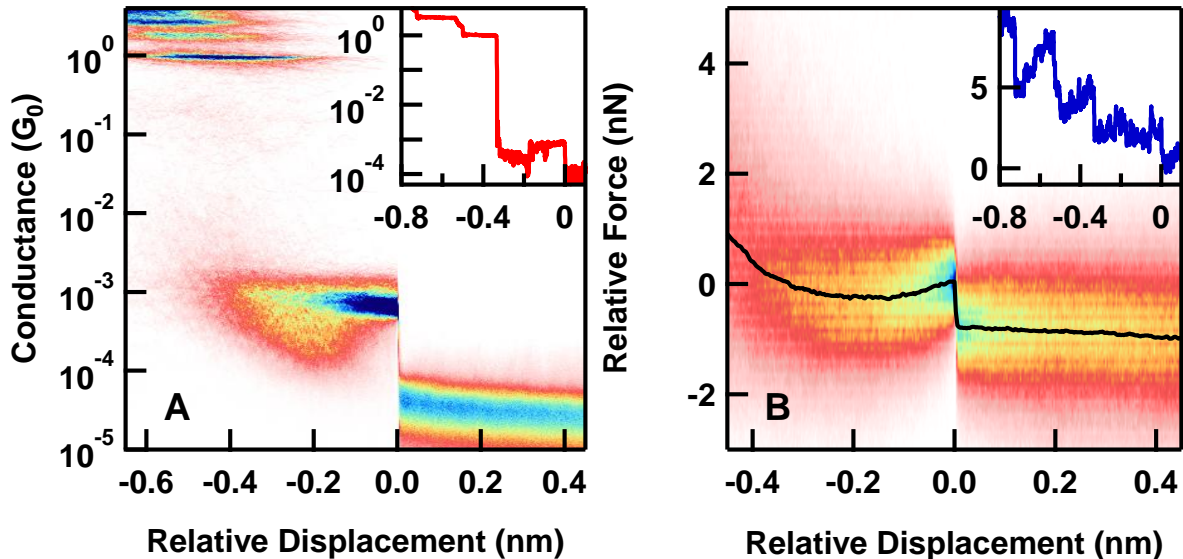


Figure 5.5 (A), 2D conductance histogram (1694 traces) for DPPP showing quantized steps above  $1G_0$  and a typical molecular signature for DPPP at around  $6.6 \times 10^{-4} G_0$ . (B) 2D force histogram for the same traces as (A). The average force profile indicates a breaking force of 0.77 nN.

comparable to that of the Au-Au bond suggesting that significant electrode rearrangements during junction evolution could be observed. However the well-defined conductance plateaus and clean force signatures seen experimentally do not support this picture in contrast to the results obtained with C4SH presented below. For the diphenylphosphine terminated molecule, steric effects imposed by the phenyl groups on the Phosphorus could result in experimentally sampled junctions that differ dramatically from the ideal pyramidal structure considered in the calculations. This could result in lower rupture forces.

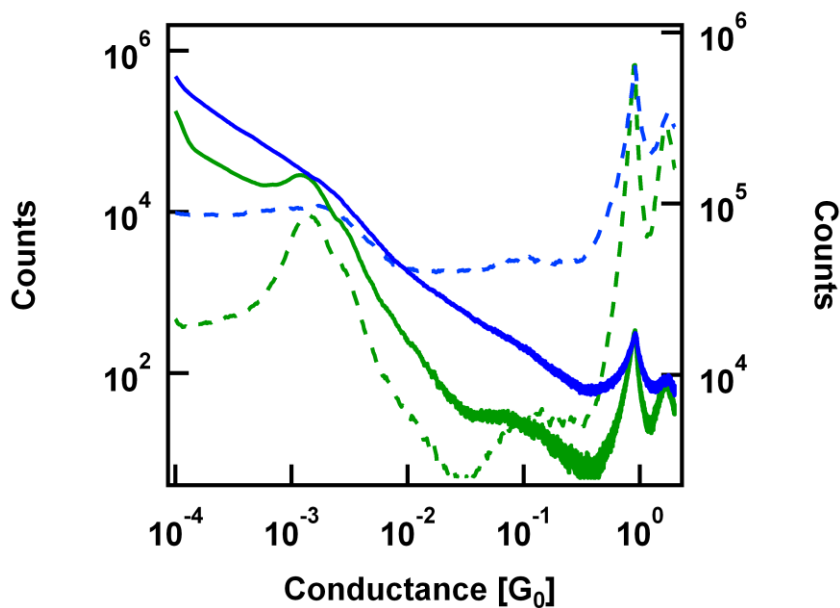


Figure 5.6 One dimensional conductance histograms for C4SMe (green, 10000 traces) and C4SH (blue, 14000 traces). The lack of a clear peak for C4SH is evident and the higher overall counts in the molecular region indicate conductance features ranging from below gold to experimental noise. The dashed lines represent log binned histograms of the respective sets and are plotted against the right axis.

## 5.5 Statistical Evaluation of Covalently Coupled Alkanes

Results from measurements with the C4SH differ from those of the other three linkers. We see a multitude of conductance features within a wide range of conductance spanning from just below  $G_0$  to the experimental noise.<sup>162-163</sup> These are in contrast to the distinct conductance plateaus seen in C4SMe measurements where we form a donor-acceptor bond between the S and an undercoordinated Au atom. For the SH linker, there are multiple bonding scenarios for an Au-S covalent bond,<sup>164</sup> many possible locations for the adsorption of the H atom on the electrodes, and also a possibility of forming an Au-SH donor acceptor bond.<sup>165</sup>

Both linearly (solid) and log (dashed) binned one-dimensional conductance histograms, generated from over 10000 traces for both molecules are shown in Figure 5.6. Since no clear conductance peak is visible for the C4SH data, we cannot construct a 2D conductance or force histogram as there is no clear displacement location in individual traces that can be used to determine the molecular junction bond rupture location along the displacement axis. We thus focus our analysis on the force traces, and use an alternate approach, based on identification of all sharp drops in individual force traces using an automated algorithm, described in detail as part of Chapter 3. Each force drop corresponds to either a bond rupture or a structural rearrangement in the junction, and can be associated with the conductance of the junction prior to the rupture event. One key difference between the 2D force analysis technique used above and this alternate force event identification method is that the former relies on the identification of events through conductance and therefore does not bias the results towards larger force values that are more easily identified. In what follows, we compare the results from measurements of C4SH and C4SMe.

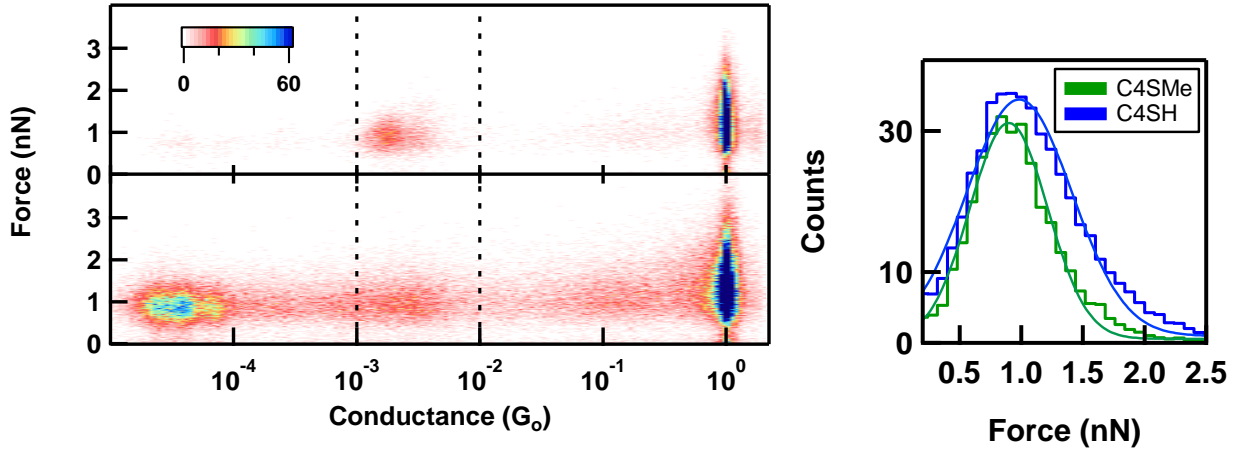


Figure 5.7 (A), 2D histogram showing all identified force events versus conductance right before the force event for C4SMe (top) and C4SH (bottom). The histograms include 51000 and 121000 individual force events respectively. The conductance bin size is 30 bins per decade, and the force bin size is 0.04 nN. (B) Histogram of force events for C4SMe (green) and C4SH (blue) with associated conductance values ranging from  $10^{-2}$  to  $10^{-3} G_0$  composed of multiple data sets.

In Figure 5.7, we show a two-dimensional histogram of bond rupture forces against the conductance prior to the rupture event from all measured traces for C4SMe (Figure 5.7A, top) and C4SH (Figure 5.7A, bottom). We see first that both histograms show a large number of force events at a conductance value around  $1G_0$ . These force events correspond to rearrangement and the final breaking of a single-atom gold contact. Second, for C4SH we find numerous force events spread along the conductance axis from just below  $1G_0$  to the experimental conductance noise of about  $2 \times 10^{-5} G_0$ . For C4SH, we find that 75% of all measured traces exhibit bond rupture events with a conductance below  $1G_0$ . Furthermore, from this selected subset, we find that each trace has an average of 2.7 bond rupture events. This is a direct indication that the sulfur-gold bond causes junction rearrangements at a range of conductance values. Finally, the C4SH data also shows a significant number of force events with conductance values equal to our experimental noise thus a large number of force events occur at a conductance that is too low to measure. This could be due to the formation of molecule dimers or due to pulling out of chains

of gold atoms, as has been seen theoretically.<sup>166</sup> In contrast, C4SMe data shows that almost all force events below  $1G_0$  occur at a narrowly defined conductance range. Of all the measured traces, 40% show bond rupture events below  $1G_0$ , and of this subset, each trace has an average of 1.5 bond rupture events. Thus although there are some structural rearrangements in SMe-terminated molecular junctions, they are not accompanied by large changes in conductance, in agreement with DFT based junction elongation simulations.<sup>124</sup> We thus conclude that C4SMe junctions form reproducibly with a narrow conductance range, and do *not* sustain multiple junction rearrangements or result in low-conducting, but mechanically robust junctions like the thiol-linked molecule.

In order to determine a bond rupture force for events having a narrow conductance range, we focus on a subset of data presented in Figure 5.7A, bound within a conductance range from  $10^{-2} - 10^{-3} G_0$  for both molecules. In Figure 5.7B we plot a histogram of all force values within this conductance range (delineated by the dashed lines in Figure 5.7A). For C4SMe the peak of this distribution occurs at 0.9 nN, which is higher than the force determined from the 2D force histogram analysis method since this selected data set is skewed towards traces that have larger force rupture events as discussed above. For C4SH, the peak is at 1 nN, significantly lower than the rupture force of the pristine single Au-atom contact. However, this distribution does show a significant number of high force events when compared with that of C4SMe. Keeping in mind that individual force events are not overestimated but the force distribution is skewed to higher forces, it does imply that rupturing or rearranging a junction with a conductance ranging from  $10^{-2} - 10^{-3} G_0$  does not, on average, require the 1.4 nN required to rupture the single Au-atom contact.<sup>141</sup> Changing the conductance range to include all force events below  $0.1 G_0$  does not change the distribution of forces significantly. Finally, to rule out the possibility that the

distributions shown in Figure 5.7 are skewed to lower forces in the C4SH case, since each trace includes multiple rupture/rearrangement events, we look at the distribution of the maximal rupture/rearrangement force within each trace with a conductance value within the molecular region. The resulting histogram is shown in Figure 5.8. Even this maximum breaking force histogram does not show a force distribution similar to that of single Au-atom contact forces. We do find that the average maximum breaking force for these thiol junctions (1.2 nN) is significantly higher than for C4SMe (0.9 nN). Combined with previous arguments these results indicate very strongly that most junctions formed with Au-thiol bonds do not rupture at a force of 1.4 nN. However, this does not imply that they do not break at the Au-Au bond. It is plausible that C4SH molecules alter the mechanical properties of the gold contacts they are bonded to, resulting in weaker Au-Au bonds. Furthermore the evolution of the molecular junction could result in gold contact structures that are very different from those of pristine gold point-contacts. Finally, position and resulting effects of the hydrogen can lead to drastic changes in force and conductance values observed, as has been shown theoretically.<sup>167-169</sup>

Although we cannot determine a unique bond rupture force for the thiol-terminated molecular junctions, we clearly see that these junctions can sustain a larger force than junctions formed with other linkers. This supports the idea that the Au-thiol bond is strong enough to cause multiple junction structure rearrangements, along with associated changes in conductance. This variability is in agreement with the experimentally observed data presented. However our data suggests that perhaps not one or the other scenario is likely but that rich features even within a single trace and certainly within a given experiment may result from a combination of these junction rearrangement processes.

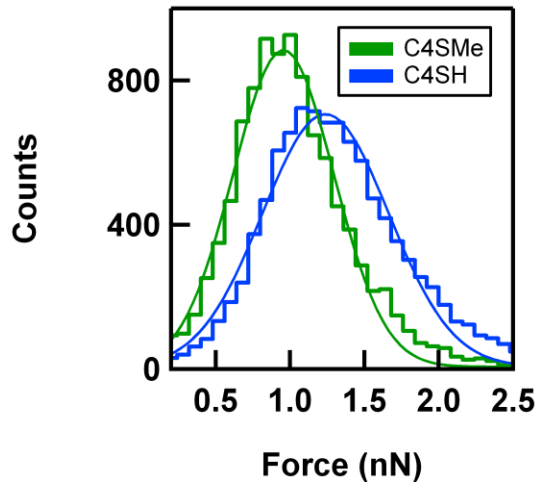


Figure 5.8 Histograms of largest force events per trace with conductance values consistent with molecular features for C4SMe (green, 10092 events) and C4SH (blue, 22888 events).

## 5.6 Conclusion

In conclusion, we presented simultaneous force and conductance data for four different chemical linker groups. Analysis of this data using 2D conductance and force histograms based on conductance event recognition shows that amine, methylsulfide, and diphenylphosphine linkers break in a molecular junction with a most probable breaking force of about 0.6, 0.7, and 0.8 nN respectively. Rupture forces of measurements carried out with C4SH, which does not have a well-defined molecular conductance signature, are analyzed directly from force traces. We see that C4SH junctions on average have more force events per trace than C4SMe. While on average the forces are smaller than that of the single Au contact, the force distributions do exhibit increased counts at forces greater than 1.4 nN. These two observations support the notion of that a strong covalent sulfur-gold bond can rearrange these molecular junctions significantly.

# Chapter 6 Mechanical Properties of Silver and Palladium Atomic Contacts

## 6.1 Introduction

The mechanical and electrical study of different metal point-contacts is motivated by observed variations in conductance measurements, bulk mechanical properties, and calculated rupture forces for single atomic chains.<sup>170-176</sup> While the conductance of these metals at the atomic scale has been investigated, their different electronic structures may lead to the formation of single-molecule junctions with different electronic and mechanical properties when compared to junctions formed with gold electrodes. This could result from changes in energy level alignment of the molecular levels with respect to the Fermi level or changes in the bond character between the molecular linker groups and the metal. Differences in metal cohesive energies could also impact mechanical properties such as electrode structure, stiffness and point-contact relaxation mechanism immediately after rupture. Electronic and mechanical properties of single-molecule junctions created using different metal electrodes could show new and interesting phenomena.

In this chapter we present simultaneous force and conductance measurements of Silver (Ag), Palladium (Pd), and Ag/Au and Pd/Au alloy atomic contacts and compare them with data from gold point contacts. There are two main challenges with these experiments which limit our choice of metals to Silver and Palladium. First, the deposition of the metal on the substrate and tip by thermal evaporation is not straightforward, and only a limited number of metals can be used. Second, we operate of our experiment under ambient conditions, and thus reactive metals cannot be used. With these constraints, we focus on Ag and Pd point contacts and study their conductance and mechanical properties. We find that Ag and Pd point contacts show markedly

different conductance and force features compared to Au point-contacts. Furthermore, we find that silver junctions formed under ambient conditions also exhibit conductance and mechanical features characteristic of oxygen impurities. We use a simple separation procedure to investigate the role of these oxygen impurities in junction formation and compare the resulting electrical and mechanical characteristics to pure atomic silver contacts. Finally, we also compare Au/Ag and Au/Pd alloy junctions and find that they are considerably different compared with the pure metal contacts.

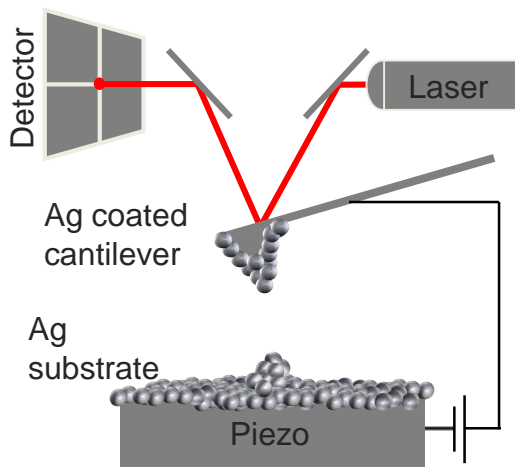


Figure 6.1 Schematic of the conductive atomic force microscope break-junction technique.

## 6.2 Experimental Methods

We use a modified conductive atomic force microscope (AFM) to investigate mechanical and electrical properties of point contacts with different metals. The experimental setup and analytical procedures have been described in Chapter 2. Briefly, a metal coated cantilever and a metal-on-mica substrate are repeatedly brought in and out of contact using a high resolution piezo positioner at a velocity of about 18 nm/s. Conductance is measured across the tip/sample junction at constant bias of 25 mV. The force is measured simultaneously by monitoring the

deflection of a laser focused on the back of the cantilever (Schematic Figure 6.1). For this study silver and palladium was deposited on mica substrates and AFM cantilever tips using a thermal evaporator (Edwards BOC/Auto 306). Typically around 300 nm of metal were deposited. No special care has been taken to limit or prevent the oxidation of our samples. For the bi-metallic junctions, we used a gold substrate and either an Ag or Pd coated cantilever.

Figure 6.2A shows a typical Ag conductance trace where a stepwise decrease in conductance is seen as a function of junction elongation similar to what is observed for an gold point-contacts. The simultaneously measured force traces show a typical saw tooth pattern attributed to reversible (elastic) and irreversible (plastic) deformations<sup>101</sup>. To determine, with statistical significance, junction conductance and bond rupture forces, we collect thousands of simultaneous conductance and force traces for each metal with multiple tip/sample pairs.

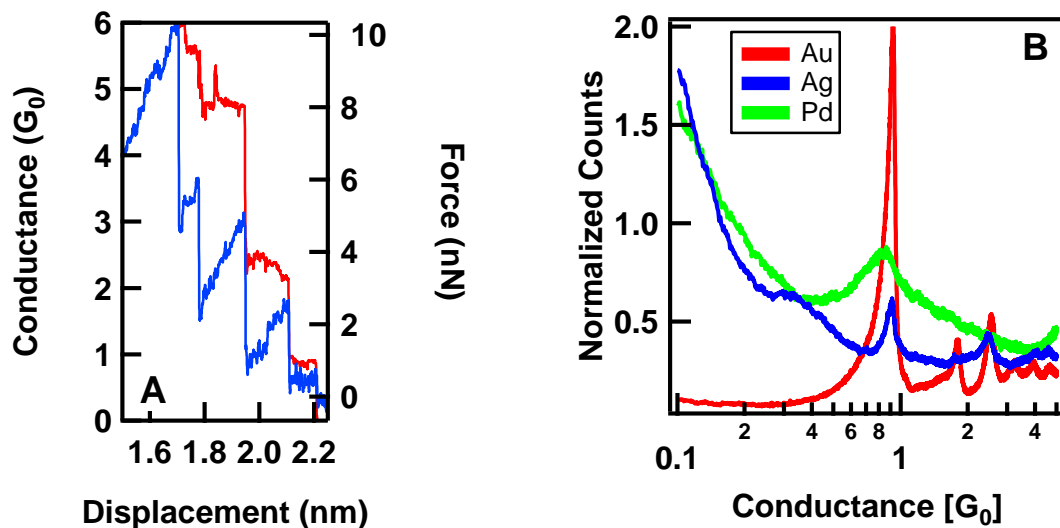


Figure 6.2(A) Example silver conductance and force trace. (B) Normalized 1D conductance histograms for gold (6000 traces), silver (10000 traces), and palladium (8000 traces). Compared to gold, silver and palladium do not form long single atomic gold chains and also show significant conductance features below the single atomic contact as indicated by the high counts.

### 6.3 Analysis Methods

We statistically analyze the large data sets using one and two-dimensional histograms techniques as detailed previously.<sup>73</sup> Briefly, these 2D conductance and force histograms are constructed by overlaying data from thousands of traces after aligning all traces to a common point along the displacement axis and aligning all force traces to have zero force at zero displacement (See Figure 6.7). To determine the rupture force, a force profile is obtained by fitting a Gaussian to the histogram cross-section at every displacement value. The magnitude of the sharp drop in this profile at zero-displacement corresponds to the average bond rupture force. For measurements with clean gold, the rupture force of a  $G_0$  conductance junction was previously determined to be 1.4 nN,<sup>73</sup> consistent with previous experimental and theoretical results.<sup>29,113,115</sup> The same methodology is applied to evaluate junction rupture forces for silver and palladium junctions.

For silver, we separately analyze measured traces that show evidence of an oxygen impurity based on the occurrence of conductance features around 0.4  $G_0$  and 1.3  $G_0$ . This amounts to creating subsets of all measured data, as will be discussed in detail later in this chapter. The selection procedure is based on conductance only. Each trace is analyzed to determine whether a plateau corresponding to a clean Ag contact ( $1G_0$ ) or that of an Ag-O-Ag contact (1.3  $G_0$  or 0.4  $G_0$ ) is present. This is done by constructing conductance histogram for each individual trace and requiring a number of data points (or the lack of data points) within specific conductance ranges. To select clean Ag junctions we require a step within the conductance range of 1-0.7  $G_0$  and fewer than 50 data points (~0.01nm in length) within the range from 0.03 – 0.63  $G_0$ . This ensures that no oxygen signature is present. The structure with conductance feature at 1.3  $G_0$  is selected by requiring a plateau in the range from 1.1 to 1.4  $G_0$ .

and fewer than 50 data points within the range from 0.5 to 1  $G_0$  and similarly, the structures resulting in the 0.4  $G_0$  signature are selected by requiring a step in the range from 0.3 to 0.6  $G_0$  and a conductance drop of an order of magnitude after the step as was applied in previous chapters. This selection procedure is very selective and often only about 5-10 percent of the collected silver traces are analyzed. This high selectivity ensures that each subset contains only the junctions of interest, i.e. an Ag point-contact or Ag contact with an O impurity.

## 6.4 Results and Discussions

Figure 6.2B shows normalized 1D conductance histograms for gold (red, 6000 traces), Ag (blue, 10000 traces), and Pd (green, 8000 traces). Au is presented for comparison and shows the typical quantized conductance features above 1  $G_0$  and a clean break after as indicated by the low count in the histogram below the 1  $G_0$ .<sup>176-179</sup> The Ag and Pd histograms show a much reduced 1 $G_0$  peak and a large increase in histogram counts below 1 $G_0$ . This indicates that these metals either do not form 1  $G_0$  contacts very frequently or form 1  $G_0$  contacts that are much shorter than the Au 1 $G_0$  contacts. Furthermore, after a 1 $G_0$  contact is broken, the conductance of Ag and Pd junction does not drop down to the tunneling regime as in Au contacts, due to the formation of some structures with conductances just below 1  $G_0$ . This yields large counts at all conductance values below 1 $G_0$ . The Ag histogram also shows a pronounced feature around 0.4  $G_0$ , indicating a frequent and stable configuration with that conductance exists. These results are in agreement with those in the literature. First, it has been observed that both Pd and Ag do exhibit a 1  $G_0$  plateau corresponding to a single atomic contact, but do not form long single atomic chains.<sup>180-185</sup> For Pd, a variety of single atomic chain conductance values have been reported; junctions with a 1 $G_0$  conductance are typically attributed to hydrogen impurities which

cannot be excluded here.<sup>185-190</sup> For Ag, a  $1G_0$  conductance plateau corresponds to a junction with a single conducting channel with unit transmission.<sup>180-184</sup> The Ag histogram peak around  $2.5 G_0$  has also been observed and attributed to a stable wire geometry with a triangular cross-section.<sup>180,184</sup> Finally, the peak around  $0.4 G_0$  in the Ag histogram has been observed experimentally and predicted theoretically, and attributed to the inclusion of oxygen in the Ag atomic wire.<sup>191-196</sup> It was proposed that the high reactivity of under-coordinated silver can dissociate oxygen molecules leaving oxygen atoms that can bridge two silver atoms to form stable Ag-O-Ag structures.<sup>197-198</sup> The evolution of the Ag point-contact in an  $O_2$  environment can thus result in single atomic Ag contact with O in parallel which can then evolve into a single atomic chain of Ag with O in series. These two structures were shown, theoretically, to have a conductance of 1.3 and  $0.4 G_0$  respectively. The reference also suggests that if a junction has a plateau at  $1.3 G_0$  or  $0.4 G_0$ , then it is less likely to have a plateau around  $1G_0$ .<sup>191,199</sup> If an O impurity is present, a clean Ag single atom contact may not be formed. Thus the occurrence of plateaus at  $1.3 G_0$  or  $0.4 G_0$  should be anti-correlated with plateaus at  $1 G_0$  and  $2.5 G_0$  and positively correlated with each other. To test this hypothesis, we carry out a cross-correlation analysis for the measured conductance traces following methods proposed in the literature as follows.<sup>200</sup> A conductance histogram is created from each trace, r, using 1000 bins of width 0.01  $G_0$ . For each bin (enumerated by the index i or j) the number of counts in the bin  $N_i(r)$  or  $N_j(r)$  is determined. The cross-correlation between a conductance bin i and j for a trace r is defined as:

$$C_{i,j} = \frac{\langle \delta N_i(r) * \delta N_j(r) \rangle_r}{\sqrt{\langle [\delta N_i(r)]^2 \rangle_r \langle [\delta N_j(r)]^2 \rangle_r}} \quad \text{Equation 6.1}$$

where  $\delta N_i(r) \equiv N_i(r) - \langle N_i(r) \rangle_r$ , and  $\langle \rangle$  represents an average over all traces r. This is calculated for every trace, and accumulated into a two-dimensional plot where the x-axis

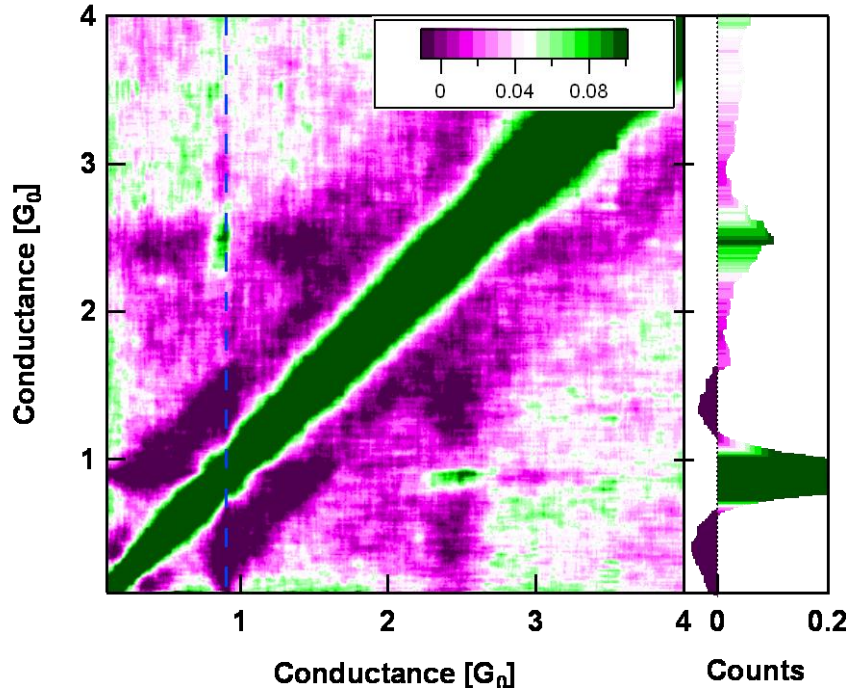


Figure 6.3 Correlation plot for 25000 Ag conductance traces along with a vertical profile at  $0.9 G_0$ . The plot supports the anti-correlation of  $.4 G_0$  steps with  $1 G_0$  and  $2.5 G_0$  steps. It also shows the positive correlation of  $0.4 G_0$  with  $1.3 G_0$ , both of which are attributed to O impurities in the Ag point-contact. The negative spots just below  $.4 G_0$  indicate the presence of plateaus at around  $0.4 G_0$ .

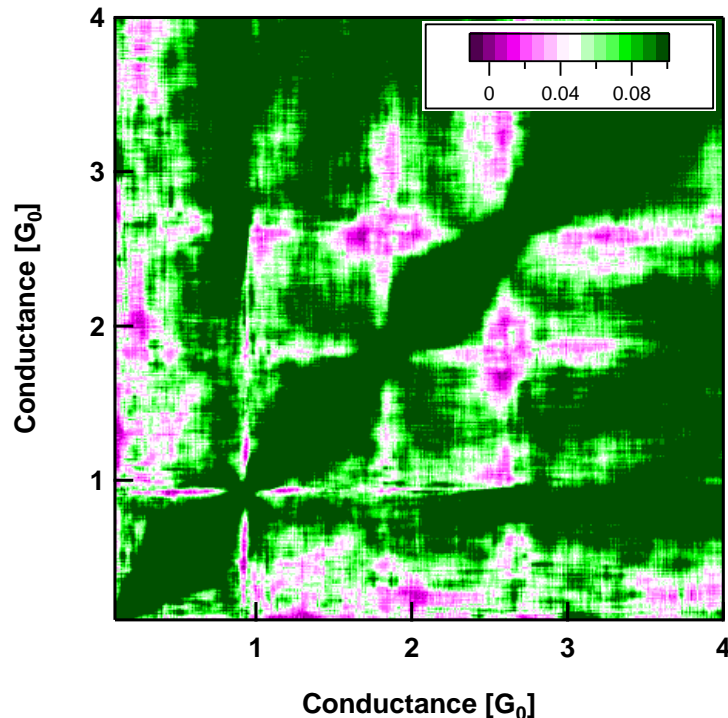


Figure 6.4 Correlation plot for 6000 Au conductance traces. The distinct step features observed for silver at around  $0.4 G_0$  are not observed for gold.

corresponds to the i-label while the y-axis corresponds to the j-label. Figure 6.3 shows the correlation plot computed from 25000 Ag point-contact conductance traces. The plot is symmetric about the diagonal (by definition). To elucidate correlations between different features in this plot, we first consider a vertical section of this plot taken slightly below  $1G_0$  (as shown in the figure). We see that this is dark green and positive around  $2.5 G_0$  indicating that plateaus around  $1G_0$  and  $2.5G_0$  are likely to occur in the same trace. We see also that this section is a dark purple and negative around  $0.4G_0$  and  $1.3 G_0$  indicating that  $1G_0$  plateaus are anti-correlated with plateaus that occur when O is present. Next, we consider a vertical section around  $1.3G_0$  (not shown). This is light green around  $0.4G_0$  indicating that traces that have a plateau around  $1.3 G_0$  are likely to also have a plateau around  $1.3G_0$ . Finally, we see that there are dark purple regions just below  $0.4 G_0$  indicate the presence of well-defined steps at around  $0.4 G_0$ , something that is not observed statistically in gold junctions, as seen in the correlation plot for clean gold in Figure 6.4. We conclude that silver point-contacts formed under ambient conditions display signatures of both clean Ag junctions and junctions with O impurities. Using the separation method discussed above we can now present conductance and force data for clean Ag, O contaminated Ag junctions, and Pd contacts.

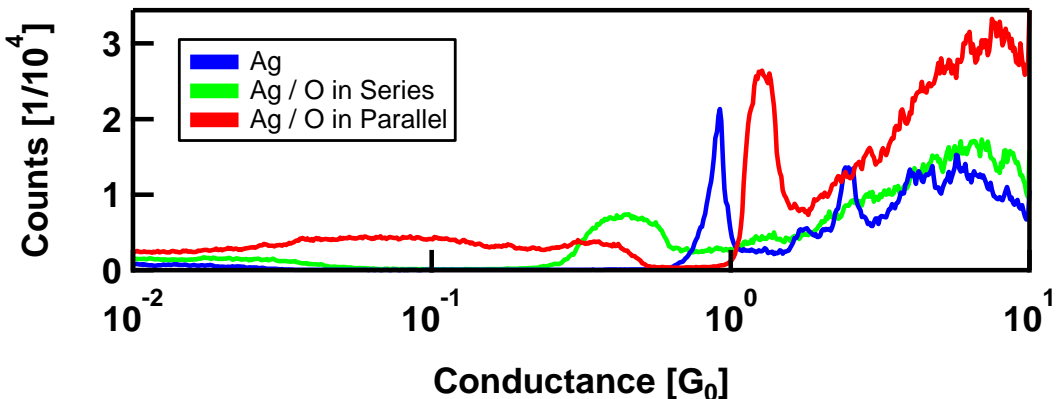


Figure 6.5 Conductance histogram for the three selected cases of clean silver (blue, 878 traces), silver and oxygen in parallel (red, 1864 traces), and silver and oxygen in series (green, 1138 traces).

To analyze the clean Ag force data, we focus on the subset of all measured traces that show a clear plateau at  $1 G_0$  step. The conductance histogram for this subset is shown in Figure 6.5 (blue trace) and has a clear peak at  $1 G_0$  with few data points below. However, it also shows a clear peak at 1.8 and  $2.5 G_0$ , as shown for oxygen free experiments in high-vacuum.<sup>180</sup> The histogram is constructed from 878 traces selected out of 22000 from three separate tip/sample pairs, indicating that these clean Ag contacts are not very frequent in these ambient experiments. Figure 6.6 shows the corresponding conductance and force histograms indicating a  $1G_0$  Ag-Ag contact rupture force of 0.9 nN, well below the benchmark for a single Au-atom contact of around 1.4 nN in excellent agreement with theoretical calculations.<sup>173,195</sup> We now compare these results with those of  $1 G_0$  Pd contacts. In Figure 6.7, we show the 2D conductance and force histogram for Pd constructed from 1054 out of 13000 traces selected to include a clear plateau at  $1G_0$  as detailed above. The data is from two separate tip/sample pairs. The average  $1G_0$  junction rupture force determined from the force profile is 1.8 nN, which is clearly larger than the rupture force of a single Au atom contact of 1.4 nN, and consistent with theoretical calculations.<sup>186-187,201</sup>

We now focus on the subsets of Ag data corresponding to the junctions with O impurities. Figure 6.5 shows one dimensional conductance histograms for the selected subsets with features at  $0.4 G_0$  (O in series) and  $1.3 G_0$  (O in parallel) generated from 1138 and 1864 traces respectively. The histogram of traces selected with a  $1.3 G_0$  plateau also shows a small peak at  $0.4 G_0$  in agreement with the cross-correlation analysis. However, this is not a one-to-one correlation as the  $0.4G_0$  peak is much smaller than that of the  $1.3G_0$ . Similarly, the histogram of traces selected with the  $0.4G_0$  also shows a peak around  $1.3 G_0$ . Two dimensional conductance and force data each of these subsets are shown in Figure 6.8 and Figure 6.9. From the force profile, we find that the rupture force of an Ag-O-Ag junction is 0.9 nN. Within error, this is

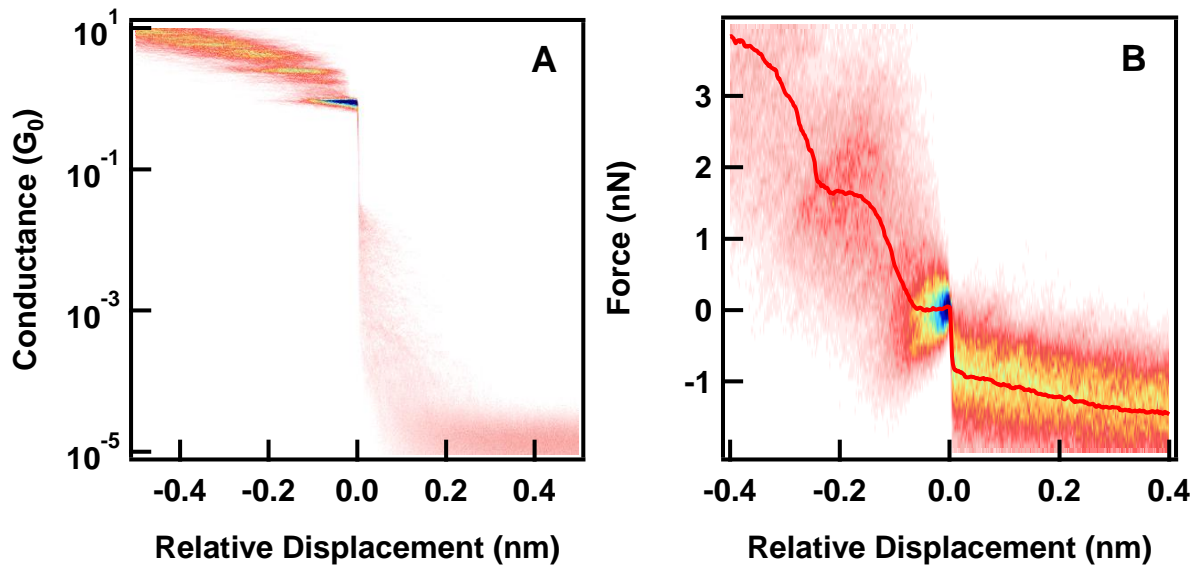


Figure 6.6 (A) Two-dimensional conductance and (B) force histograms aligned at the break from  $1 G_0$  for Silver. Histograms are for 878 traces selected from 22000 traces. The red trace indicates the averaged force profile.

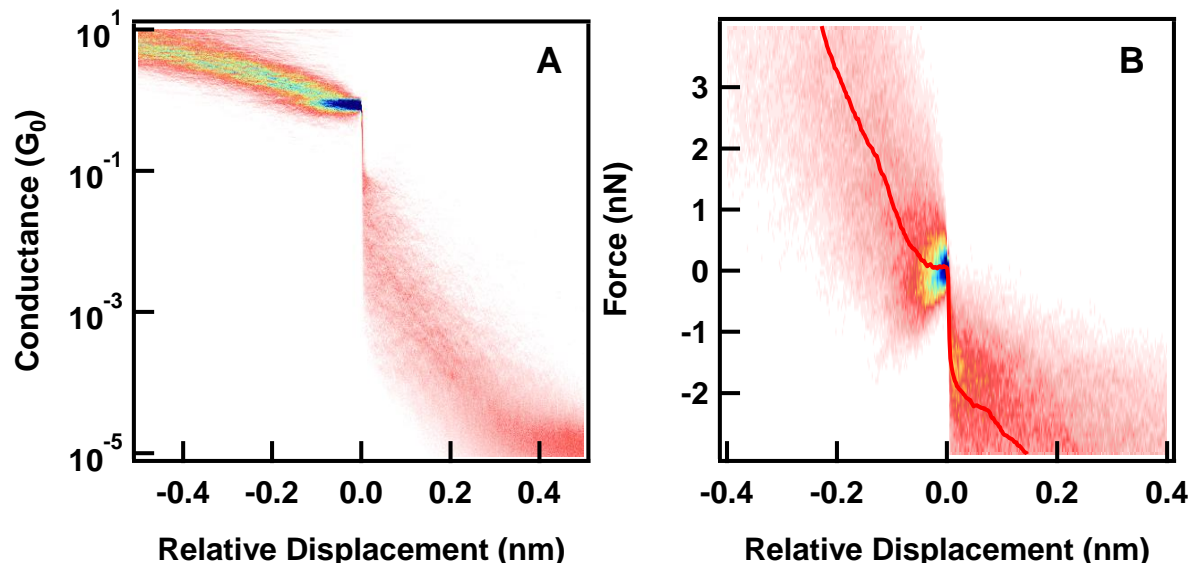


Figure 6.7 (A) Two-dimensional conductance and (B) force histograms aligned at the break from  $1 G_0$  for Palladium. Histograms are for 1054 traces selected from 13000 traces. The red trace indicates the averaged force profile.

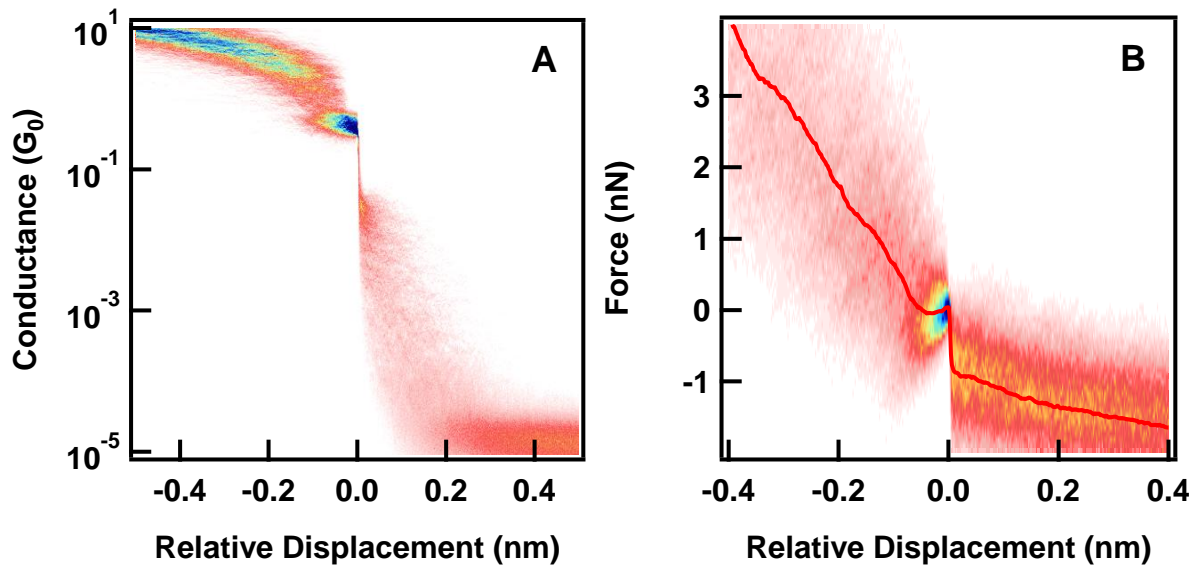


Figure 6.8 (A) Two-dimensional conductance and (B) force histograms aligned at the break from  $0.4 G_0$  for Silver. Histograms are for 1138 traces selected from 22000 traces. The red trace indicates the averaged force profile.

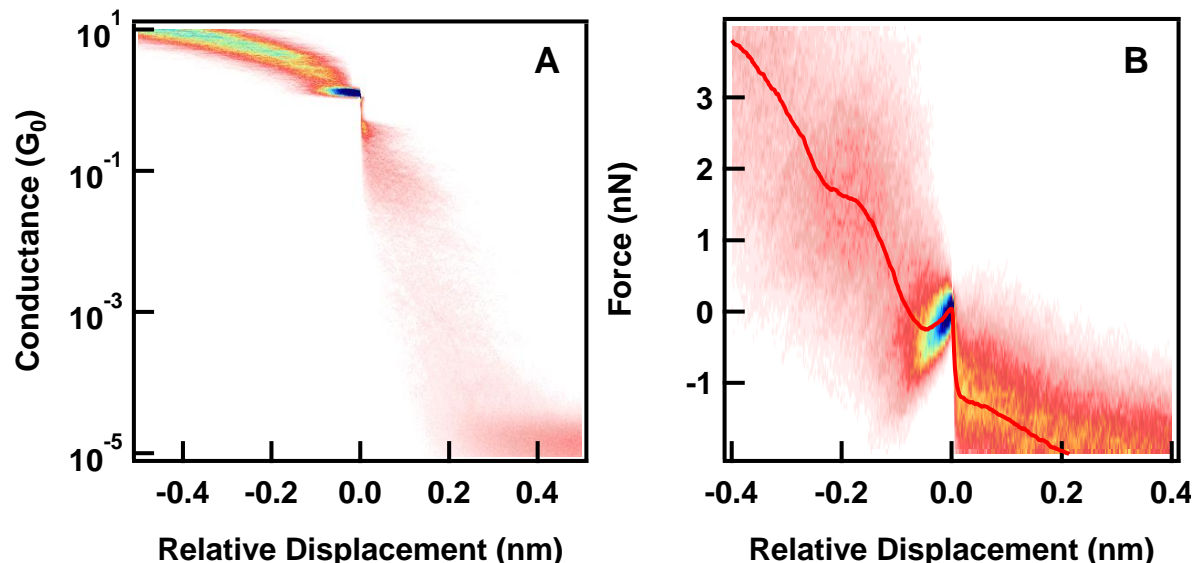


Figure 6.9 (A) Two-dimensional conductance and (B) force histograms aligned at the break from  $1.3 G_0$  for Silver. Histograms are for 1864 traces selected from 22000 traces. The red trace indicates the averaged force profile.

identical to the rupture force of a  $1 G_0$  Ag-Ag contact and in excellent agreement with calculations, where the proposed structure ruptures at a Ag-Ag bond because the Ag-O bond is much stronger.<sup>195</sup> The junctions with conductance values of  $1.3 G_0$  are found to break with a force of about 1.1 nN as seen in Figure 6.9. These junctions correspond to having an O in parallel to the Ag-Ag contact, which should have a larger rupture force in agreement with our results.<sup>191,197-198</sup> If we exclude, from these selected traces, those that have a plateau around  $0.4 G_0$  (leaving only 150 traces), we find that the rupture force of the  $1.3 G_0$  junction increases to 1.6 nN. Thus junctions that do not evolve into an Ag-O-Ag structure rupture at a significantly larger force. These results are summarized in Figure 6.10.

We now turn to measurements where we use either an Ag or Pd coated cantilever and an Au substrate. Figure 6.11B shows the conductance histograms constructed from all measured traces, along with a histogram of clean Au junctions. Figure 6.12 shows the conductance and force histograms for the Ag/Au measurements. We see that the conductance data of the Ag/Au system shows a  $2 G_0$  peak reminiscent of gold junctions. This 1D conductance histogram shows that we could be creating a variety of different junctions (just Au, just Ag or mixed junctions), which cannot be identified clearly. The force data indicates however, that the rupture of the  $1 G_0$  plateau occurs at a force of about 1.4 nN significantly higher than that of the Ag-Ag contact.

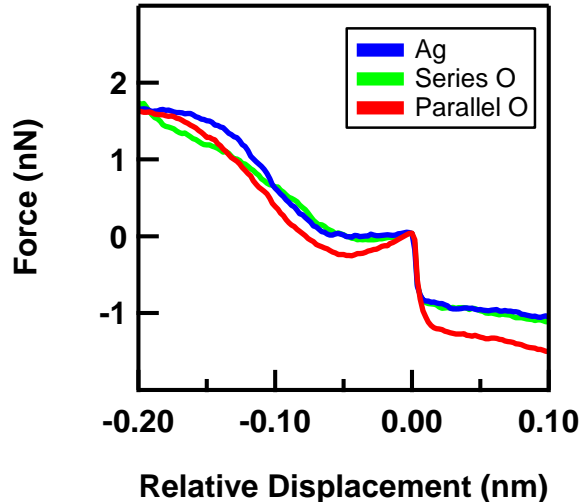


Figure 6.10 Averaged force profiles for silver, silver-gold, and silver with oxygen in series and parallel.

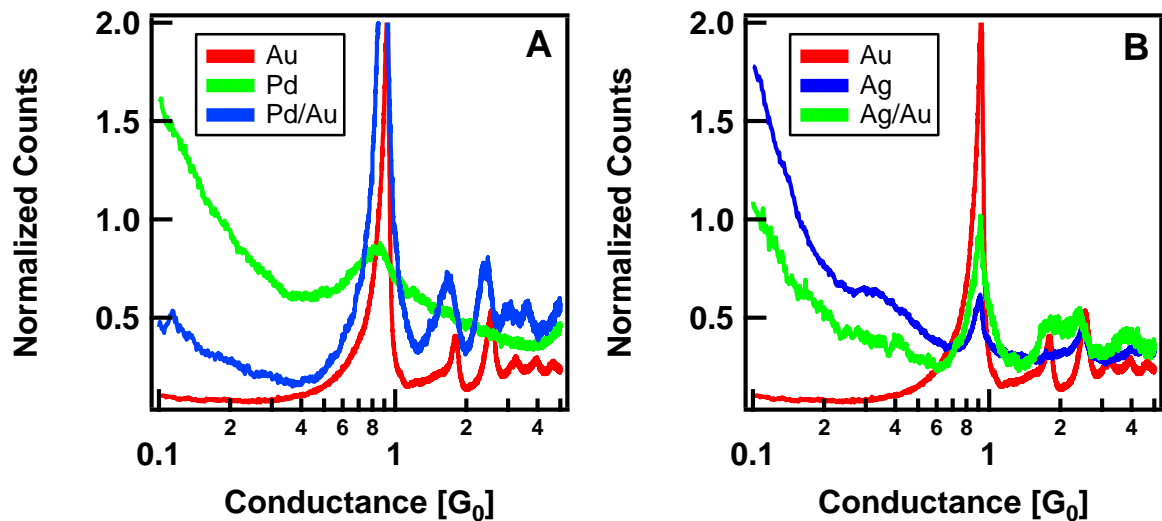


Figure 6.11 (A) Conductance histogram for Gold, Palladium, and Gold/Palladium. (B) Conductance histogram for Gold, Silver , and Gold/Silver.

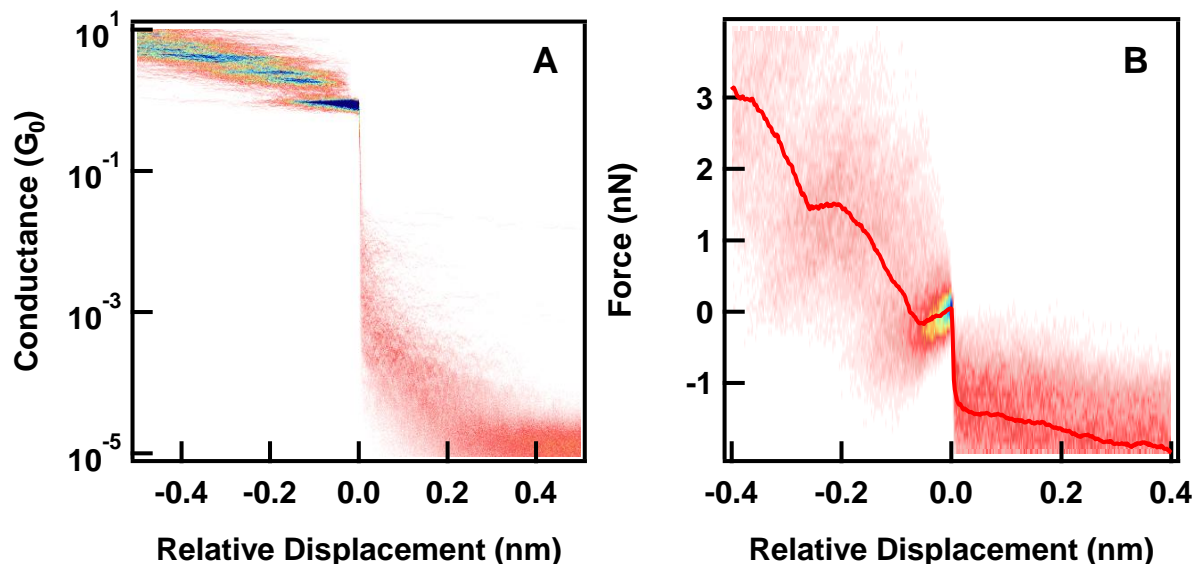


Figure 6.12 (A) Two-dimensional conductance and (B) force histograms aligned at the break from  $1 G_0$  for Silver/Gold junctions. Histograms are for 530 traces selected from 3000 traces. The red trace indicates the averaged force profile.

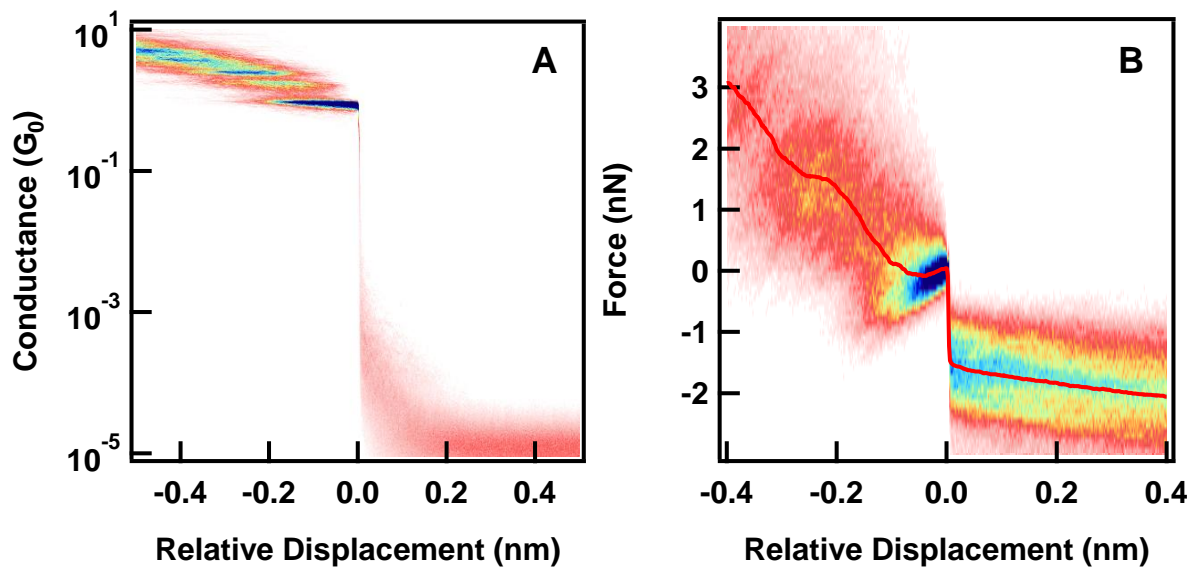


Figure 6.13 (A) Two-dimensional conductance and (B) force histograms aligned at the break from  $1 G_0$  for Palladium/Gold junction. Histograms are for 1315 traces selected from 5000 traces. The red trace indicates the averaged force profile.

Thus although the conductance signatures are not clearly identified, the rupture force is very close to that of an Au single atom contact. The data for Pd/Au junctions is shown in Figure 6.11A where the previous results for only Pd and only Au are provided as a reference. Figure 6.13 shows the corresponding 2D conductance and force histograms. The result for Pd/Au (blue) shows conductance features nearly identical to gold-only junctions (red). Particularly, we find clear steps at integer multiples of  $1 G_0$  and much lower counts below  $1 G_0$ , indicative of clean rupture of the atomic contact. The average breaking force for these junctions is about 1.6 nN, slightly larger than that of the single Au-atomic contact. Again, this suggests that the Au-Pd breaking force is smaller than  $1 G_0$  Pd breaking force, or that a significant number of pure Au-Au contacts are broken. If, as suggested in the literature,<sup>202-203</sup> the Au-Pd junction has a much lower conductance value than  $1 G_0$ , we can conclude that we form a combination of predominantly Au-Au and some Pd-Pd junctions, which agrees with previous work suggesting the dominance of the

noble metal in these alloy junctions under low bias.<sup>184,204-206</sup> Figure 6.14 summarizes the rupture force results for Pd, Pd/Au, Ag, and Ag/Au junctions.

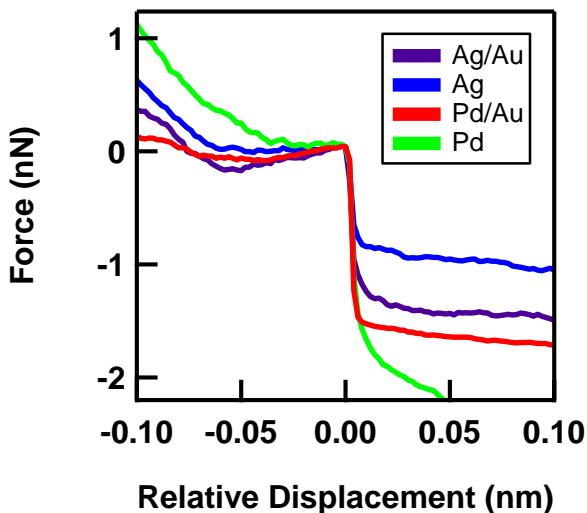


Figure 6.14 Force profiles for silver, silver-gold, palladium, and palladium-gold.

## 6.5 Summary

We have studied the electric and mechanical behavior of Ag and Pd junctions in ambient conditions. Measurements with Ag show conductance features of clean Ag-Ag contacts as well as those that include O impurities. Using a simple selection process we can separate different junctions from the data set. We find that the rupture forces for an Ag-Ag bond is 0.9 nN. Junctions that show a conductance plateau around  $0.4 G_0$  rupture at the same force, while those with a final conductance plateau at  $1.3G_0$  rupture at 1.6 nN. This supports the picture that these two plateaus can be attributed to Ag point contacts with an O atom in series and with an O atom in parallel respectively. Pd junctions exhibit a broad  $1 G_0$  peak and rupture at a force of 1.8 nN, larger than that of an Au-Au single atom contact. Interestingly, alloy junctions of Ag/Au show

conductance features of both gold and silver junctions but break at a force identical to the clean gold-gold breaking force. For Pd/Au junction the conductance histogram suggests a clean gold rupture but a breaking force larger than for clean Au-Au.

## Chapter 7 Outlook

The results presented as part of this thesis have afforded a wealth of new information about single molecule break junction measurements. Looking ahead however, changes and improvements in both the experimental and analytical procedures could be beneficial.

Long term setup modifications could include a force feedback mechanism, an interferometer based vibration isolation system<sup>207</sup>, a non-laser-based force detection mechanism, and operation under vacuum. These directly address some of the limitations or difficulties of the current setup. For example, laser heating leads to expansion of the metal and bending of the cantilever and also accelerated evaporation of solvents used during molecule deposition. Elimination of the laser could be achieved through some of the techniques mentioned in Chapter 1. Operation of the experiment under vacuum would allow environmental control which would be particularly useful for oxidizing metals such as silver (as seen in Chapter 6). While mechanical stability is not an issue under the current experimental parameters, vibrational damping would need to be improved if pulling the junctions at significantly lower speeds is desired. Shorter term improvements could focus on the transition to solid metal cantilevers.

On the analytical side, a theoretical model relating the measured quantities such as stiffness, breaking force, and step-length is needed. While such models exist for biological systems, it is not clear if and how they are applicable to these dynamic single molecule break-junction measurements. With such a model, it would be possible to relate the measured parameters to the energy landscape of the particular bond, providing a fingerprint for identification of observed rupture events during junction formation and breaking.

## References

- (1) Aviram, A.; Ratner, M. A. *Chem Phys Lett* **1974**, *29*, 277.
- (2) Elbing, M.; Ochs, R.; Koentopp, M.; Fischer, M.; von Hanisch, C.; Weigend, F.; Evers, F.; Weber, H. B.; Mayor, M. *P Natl Acad Sci USA* **2005**, *102*, 8815.
- (3) Smit, R. H. M.; Noat, Y.; Untiedt, C.; Lang, N. D.; van Hemert, M. C.; van Ruitenbeek, J. M. *Nature* **2002**, *419*, 906.
- (4) Datta, S. *Electronic transport in mesoscopic systems*; Cambridge University Press: Cambridge ; New York, 1995.
- (5) *Introducing Molecular Electronics*; Cuniberti, G., Giorgios, F., Richter, K., Ed.; Springer, 2005; Vol. XIII.
- (6) Holcomb, D. F. *Am J Phys* **1967**, *35*, 547.
- (7) Ashcroft, N. W., Mermin, N.D. *Solid State Physics*; Saunders College, 1976.
- (8) Cuevas, J. C. *Molecular Electronics: an Introduction to Theory and Experiment*; World Scientific Publishing Co., 2010; Vol. 1.
- (9) Kittel, C. *Introduction to Solid State Physics*, 1953; Vol. 78.
- (10) van den Brom, H. E.; van Ruitenbeek, J. M. *Phys Rev Lett* **1999**, *82*, 1526.
- (11) Silbey, R. J. *Physical Chemistry*; Wiley: New York, 2001.
- (12) Atkins, P. W. *Molecular Quantum Mechanics*; Third Edition ed.; Oxford University Press: New York, 2001.
- (13) Griffiths, D. J. *Introduction to quantum mechanics*; Prentice Hall: Englewood Cliffs, N.J., 1995.
- (14) Morse, P. M. *Phys Rev* **1929**, *34*, 57.
- (15) Dudko, O. K.; Filippov, A. E.; Klafter, J.; Urbakh, M. *P Natl Acad Sci USA* **2003**, *100*, 11378.
- (16) Dudko, O. K.; Hummer, G.; Szabo, A. *P Natl Acad Sci USA* **2008**, *105*, 15755.
- (17) Dudko, O. K.; Mathe, J.; Szabo, A.; Meller, A.; Hummer, G. *Biophys J* **2007**, *92*, 4188.
- (18) H.A, K. *Physica* **1940**, *7*, 284.
- (19) Jarzynski, C. *Phys Rev Lett* **1997**, *78*, 2690.
- (20) Bell, G. I. *Science* **1978**, *200*, 618.

- (21) Evans, E. *Annu Rev Biophys Biom* **2001**, *30*, 105.
- (22) Hanke, F.; Kreuzer, H. J. *Phys Rev E* **2006**, *74*, 031909.
- (23) Beyer, M. *J. Chem. Phys.* **2000**, *112*, 7307.
- (24) Akkerman, H. B.; de Boer, B. *J Phys-Condens Mat* **2008**, *20*.
- (25) Xu, B.; Tao, N. J. *Science* **2003**, *301*, 1221.
- (26) Muller, C. J.; van Ruitenbeek, J. M.; de Jongh, L. J. *Physica C: Superconductivity* **1992**, *191*, 485.
- (27) Agrait, N.; Yeyati, A. L.; van Ruitenbeek, J. M. *Phys Rep* **2003**, *377*, 81.
- (28) Smith, D. T.; Pratt, J. R.; Tavazza, F.; Levine, L. E.; Chaka, A. M. *J Appl Phys* **2010**, *107*.
- (29) Tavazza, F.; Levine, L. E.; Chaka, A. M. *J Appl Phys* **2009**, *106*.
- (30) Song, H.; Lee, H.; Lee, T. *J Am Chem Soc* **2007**, *129*, 3806.
- (31) Wold, D. J.; Frisbie, C. D. *J Am Chem Soc* **2000**, *122*, 2970.
- (32) Reed, M. A.; Zhou, C.; Muller, C. J.; Burgin, T. P.; Tour, J. M. *Science* **1997**, *278*, 252.
- (33) Kergueris, C.; Bourgoin, J. P.; Palacin, S.; Esteve, D.; Urbina, C.; Magoga, M.; Joachim, C. *Phys Rev B* **1999**, *59*, 12505.
- (34) Dulić, D.; van der Molen, S. J.; Kudernac, T.; Jonkman, H. T.; de Jong, J. J. D.; Bowden, T. N.; van Esch, J.; Feringa, B. L.; van Wees, B. J. *Phys Rev Lett* **2003**, *91*, 207402.
- (35) González, M. T.; Wu, S.; Huber, R.; van der Molen, S. J.; Schönenberger, C.; Calame, M. *Nano Lett* **2006**, *6*, 2238.
- (36) Lörtscher, E.; Weber, H. B.; Riel, H. *Phys Rev Lett* **2007**, *98*, 176807.
- (37) Tam, E. S.; Parks, J. J.; Shum, W. W.; Zhong, Y. W.; Santiago-Berrios, M. B.; Zheng, X.; Yang, W. T.; Chan, G. K. L.; Abruna, H. D.; Ralph, D. C. *Acs Nano* **2011**, *5*, 5115.
- (38) Champagne, A. R.; Pasupathy, A. N.; Ralph, D. C. *Nano Lett* **2005**, *5*, 305.
- (39) Binnig, G.; Quate, C. F.; Gerber, C. *Phys Rev Lett* **1986**, *56*, 930.
- (40) Albrecht, T. J. *Appl. Phys.* **1987**, *62*, 2599.
- (41) Fotiadis, D.; Scheuring, S.; Muller, S. A.; Engel, A.; Muller, D. J. *Micron* **2002**, *33*, 385.

- (42) Kasas, S.; Thomson, N. H.; Smith, B. L.; Hansma, P. K.; Miklossy, J.; Hansma, H. G. *Int J Imag Syst Tech* **1997**, *8*, 151.
- (43) Ritort, F. *J Phys-Condens Mat* **2006**, *18*, R531.
- (44) Ikai, A.; Endo, I., Nagamune, T., Eds.; Springer Berlin / Heidelberg: 2010; Vol. 119, p 47.
- (45) Teichert, C.; Beinik, I.; Bhushan, B., Ed.; Springer Berlin Heidelberg: 2011, p 691.
- (46) Alegre-Cebollada, J.; Kosuri, P.; Rivas-Pardo, J. A.; Fernández, J. M. *Nat Chem* **2011**, *advance online publication*.
- (47) Gross, L.; Mohn, F.; Moll, N.; Liljeroth, P.; Meyer, G. *Science* **2009**, *325*, 1110.
- (48) Gross, L.; Mohn, F.; Moll, N.; Meyer, G.; Ebel, R.; Abdel-Mageed, W. M.; Jaspars, M. *Nature Chemistry* **2010**, *2*, 821.
- (49) Falvo, M. R.; Taylor II, R. M.; Helser, A.; Chi, V.; Brooks Jr, F. P.; Washburn, S.; Superfine, R. *Nature* **1999**, *397*, 236.
- (50) Bockrath, M.; Liang, W.; Bozovic, D.; Hafner, J. H.; Lieber, C. M.; Tinkham, M.; Park, H. *Science* **2001**, *291*, 283.
- (51) Postma, H. W. C.; de Jonge, M.; Yao, Z.; Dekker, C. *Phys Rev B* **2000**, *62*, R10653.
- (52) Avouris, P.; Hertel, T.; Martel, R.; Schmidt, T.; Shea, H. R.; Walkup, R. E. *Applied Surface Science* **1999**, *141*, 201.
- (53) Bozovic, D. *Appl. Phys. Lett.* **2001**, *78*, 3693.
- (54) Roschier, L. *Appl. Phys. Lett.* **1999**, *75*, 728.
- (55) Thelander, C. *Appl. Phys. Lett.* **2001**, *79*, 2106.
- (56) Postma, H. W. C.; Teepen, T.; Yao, Z.; Grifoni, M.; Dekker, C. *Science* **2001**, *293*, 76.
- (57) Bachtold, A.; Fuhrer, M. S.; Plyasunov, S.; Forero, M.; Anderson, E. H.; Zettl, A.; McEuen, P. L. *Phys Rev Lett* **2000**, *84*, 6082.
- (58) Tans, S. J.; Dekker, C. *Nature* **2000**, *404*, 834.
- (59) Park, J. *Appl. Phys. Lett.* **2002**, *80*, 4446.
- (60) Clausen-Schaumann, H.; Seitz, M.; Krautbauer, R.; Gaub, H. E. *Curr Opin Chem Biol* **2000**, *4*, 524.
- (61) Alexander, S.; Hellemans, L.; Marti, O.; Schneir, J.; Elings, V.; Hansma, P. K.; Longmire, M.; Gurley, J. *J Appl Phys* **1989**, *65*, 164.

- (62) Drake, A. D.; Leiner, D. C. *Rev Sci Instrum* **1984**, *55*, 162.
- (63) Rugar, D.; Mamin, H. J.; Guethner, P. *Applied Physics Letters* **1989**, *55*, 2588.
- (64) Bruland, K. J.; Garbini, J. L.; Dougherty, W. M.; Chao, S. H.; Jensen, S. E.; Sidles, J. A. *Rev Sci Instrum* **1999**, *70*, 3542.
- (65) Neubauer, G.; Cohen, S. R.; McClelland, G. M.; Horne, D.; Mate, C. M. *Rev Sci Instrum* **1990**, *61*, 2296.
- (66) Rugar, D.; Mamin, H. J.; Guethner, P.; Lambert, S. E.; Stern, J. E.; McFadyen, I.; Yogi, T. *J Appl Phys* **1990**, *68*, 1169.
- (67) Rensen, W. H. J.; van Hulst, N. F.; Ruiter, A. G. T.; West, P. E. *Applied Physics Letters* **1999**, *75*, 1640.
- (68) Meyer, G.; Amer, N. M. *Applied Physics Letters* **1988**, *53*, 1045.
- (69) Harley, J. A.; Kenny, T. W. *Applied Physics Letters* **1999**, *75*, 289.
- (70) Murdfield, T.; Fischer, U. C.; Fuchs, H.; Volk, R.; Michels, A.; Meinen, F.; Beckman, E. *J Vac Sci Technol B* **1996**, *14*, 877.
- (71) Neuman, K. C.; Nagy, A. *Nat Methods* **2008**, *5*, 491.
- (72) Halvorsen, K.; Wong, W. P. *Biophys J* **2010**, *98*, L53.
- (73) Frei, M.; Aradhya, S. V.; Koentopp, M.; Hybertsen, M. S.; Venkataraman, L. *Nano Lett* **2011**, *11*, 1518.
- (74) Olesen, L.; Laegsgaard, E.; Stensgaard, I.; Besenbacher, F.; Schiotz, J.; Stoltze, P.; Jacobsen, K. W.; Norskov, J. K. *Phys Rev Lett* **1995**, *74*, 2147.
- (75) Olesen, L.; Laegsgaard, E.; Stensgaard, I.; Besenbacher, F.; Schiotz, J.; Stoltze, P.; Jacobsen, K. W.; Norskov, J. K. *Phys Rev Lett* **1994**, *72*, 2251.
- (76) Kamenetska, M.; Quek, S. Y.; Whalley, A. C.; Steigerwald, M. L.; Choi, H. J.; Louie, S. G.; Nuckolls, C.; Hybertsen, M. S.; Neaton, J. B.; Venkataraman, L. *J Am Chem Soc* **2010**, *132*, 6817.
- (77) Quek, S. Y.; Kamenetska, M.; Steigerwald, M. L.; Choi, H. J.; Louie, S. G.; Hybertsen, M. S.; Neaton, J. B.; Venkataraman, L. *Nat Nano* **2009**, *4*, 230.
- (78) Ulman, A. *Chemical Reviews* **1996**, *96*, 1533.
- (79) Venkataraman, L.; Klare, J. E.; Tam, I. W.; Nuckolls, C.; Hybertsen, M. S.; Steigerwald, M. L. *Nano Lett* **2006**, *6*, 458.

- (80) Houck, A. A.; Labaziewicz, J.; Chan, E. K.; Folk, J. A.; Chuang, I. L. *Nano Lett* **2005**, *5*, 1685.
- (81) Sondag-Huethorst, J. A. M.; Schonenberger, C.; Fokkink, L. G. J. *The Journal of Physical Chemistry* **1994**, *98*, 6826.
- (82) Krüger, D.; Fuchs, H.; Rousseau, R.; Marx, D.; Parrinello, M. *Phys Rev Lett* **2002**, *89*, 186402.
- (83) WaveMetrics; [www.wavemetrics.com](http://www.wavemetrics.com); 2011.
- (84) Saulson, P. R. *Phys Rev D* **1990**, *42*, 2437.
- (85) Fukuma, T.; Kimura, M.; Kobayashi, K.; Matsushige, K.; Yamada, H. *Rev Sci Instrum* **2005**, *76*.
- (86) Nanosensors [www.nanosensors.com](http://www.nanosensors.com).
- (87) BudgetSensors [www.budgetsensors.com](http://www.budgetsensors.com).
- (88) Hutter, J. L.; Bechhoefer, J. *Rev Sci Instrum* **1993**, *64*, 1868.
- (89) Burnham, N. A.; Chen, X.; Hodges, C. S.; Matei, G. A.; Thoreson, E. J.; Roberts, C. J.; Davies, M. C.; Tendler, S. J. B. *Nanotechnology* **2003**, *14*, 1.
- (90) Myhra, S.; Gibson, C. T.; Watson, G. S. *Scanning* **1997**, *19*, 564.
- (91) Sader, J. E.; Chon, J. W. M.; Mulvaney, P. *Rev Sci Instrum* **1999**, *70*, 3967.
- (92) Sader, J. E.; Larson, I.; Mulvaney, P.; White, L. R. *Rev Sci Instrum* **1995**, *66*, 3789.
- (93) Cleveland, J. P.; Manne, S.; Bocek, D.; Hansma, P. K. *Rev Sci Instrum* **1993**, *64*, 403.
- (94) Tortonese, M.; Kirk, M. *Characterization of application-specific probes for SPMs*; SPIE, 1997; Vol. 3009.
- (95) Butt, H. J.; Heim, L. O.; Kappl, M. *Langmuir* **2004**, *20*, 2760.
- (96) Hutter, J. L. *Langmuir* **2005**, *21*, 2630.
- (97) Landman, U.; Barnett, R. N.; Luedtke, W. D. *Zeitschrift fuer Physik D: Atoms, Molecules and Clusters* **1997**, *40*, 282.
- (98) Landman, U.; Luedtke, W. D.; Barnett, R. N. *NATO ASI Series, Series E: Applied Sciences* **1997**, *340*, 109.
- (99) Sorensen, M. R.; Brandbyge, M.; Jacobsen, K. W. *Phys Rev B* **1998**, *57*, 3283.
- (100) Kizuka, T.; Fujisawa, S. *Memoirs of the Institute of Scientific and Industrial Research, Osaka University* **2000**, *57*, 240.

- (101) Marszalek, P. E.; Greenleaf, W. J.; Li, H. B.; Oberhauser, A. F.; Fernandez, J. M. *P Natl Acad Sci USA* **2000**, *97*, 6282.
- (102) da Silva, E. Z.; da Silva, A. J. R.; Fazzio, A. *Phys. Rev. Lett.* **2001**, *87*, 256102/1.
- (103) Da Silva, E. Z.; Da Silva, A. J. R.; Fazzio, A. *Comput. Mater. Sci.* **2004**, *30*, 73.
- (104) Chen, D. L.; Chen, T. C. *Nanotechnology* **2005**, *16*, 2972.
- (105) Pauly, F.; Dreher, M.; Viljas, J. K.; Hafer, M.; Cuevas, J. C.; Nielaba, P. *Phys Rev B* **2006**, *74*.
- (106) Heidelberg, A.; Ngo, L. T.; Wu, B.; Phillips, M. A.; Sharma, S.; Kamins, T. I.; Sader, J. E.; Boland, J. J. *Nano Lett* **2006**, *6*, 1101.
- (107) Pu, Q.; Leng, Y. S.; Tsetseris, L.; Park, H. S.; Pantelides, S. T.; Cummings, P. T. *J Chem Phys* **2007**, *126*.
- (108) Kizuka, T. *Phys Rev B* **2008**, *77*.
- (109) Liu, S. S.; Wen, Y. H.; Zhu, Z. Z. *Chinese Phys B* **2008**, *17*, 2621.
- (110) Tavazza, F.; Smith, D. T.; Levine, L. E.; Pratt, J. R.; Chaka, A. M. *Phys Rev Lett* **2011**, *107*.
- (111) Agrait, N.; Rodrigo, J. G.; Vieira, S. *Phys Rev B* **1993**, *47*, 12345.
- (112) Agrait, N.; Rubio, G.; Vieira, S. *Langmuir* **1996**, *12*, 4505.
- (113) Rubio, G.; Agrait, N.; Vieira, S. *Phys. Rev. Lett.* **1996**, *76*, 2302.
- (114) Untiedt, C.; Rubio, G.; Vieira, S.; Agrait, N. *Phys Rev B* **1997**, *56*, 2154.
- (115) Rubio-Bollinger, G.; Bahn, S. R.; Agrait, N.; Jacobsen, K. W.; Vieira, S. *Phys Rev Lett* **2001**, *87*02.
- (116) Jarvis, S. P.; Lantz, M. A.; Ogiso, H.; Tokumoto, H.; Durig, U. *Applied Physics Letters* **1999**, *75*, 3132.
- (117) Venkataraman, L.; Klare, J. E.; Nuckolls, C.; Hybertsen, M. S.; Steigerwald, M. L. *Nature* **2006**, *442*, 904.
- (118) Park, Y. S.; Whalley, A. C.; Kamenetska, M.; Steigerwald, M. L.; Hybertsen, M. S.; Nuckolls, C.; Venkataraman, L. *J Am Chem Soc* **2007**, *129*, 15768.
- (119) Huang, Z.; Chen, F.; Bennett, P. A.; Tao, N. *J Am Chem Soc* **2007**, *129*, 13225.
- (120) Quek, S. Y.; Venkataraman, L.; Choi, H. J.; Louie, S. G.; Hybertsen, M. S.; Neaton, J. B. *Nano Lett* **2007**, *7*, 3477.

- (121) Quinn, J. R.; Foss, F. W., Jr.; Venkataraman, L.; Hybertsen, M. S.; Breslow, R. *J Am Chem Soc* **2007**, *129*, 6714.
- (122) Lortscher, E.; Weber, H. B.; Riel, H. *Phys Rev Lett* **2007**, *98*.
- (123) Venkataraman, L.; Park, Y. S.; Whalley, A. C.; Nuckolls, C.; Hybertsen, M. S.; Steigerwald, M. L. *Nano Lett* **2007**, *7*, 502.
- (124) Kamenetska, M.; Koentopp, M.; Whalley, A. C.; Park, Y. S.; Steigerwald, M. L.; Nuckolls, C.; Hybertsen, M. S.; Venkataraman, L. *Phys Rev Lett* **2009**, *102*.
- (125) Park, Y. S.; Widawsky, J. R.; Kamenetska, M.; Steigerwald, M. L.; Hybertsen, M. S.; Nuckolls, C.; Venkataraman, L. *J Am Chem Soc* **2009**, *131*, 10820.
- (126) Widawsky, J. R.; Kamenetska, M.; Klare, J.; Nuckolls, C.; Steigerwald, M. L.; Hybertsen, M. S.; Venkataraman, L. *Nanotechnology* **2009**, *20*.
- (127) Diez-Perez, I.; Hihath, J.; Lee, Y.; Yu, L. P.; Adamska, L.; Kozhushner, M. A.; Oleynik, I. I.; Tao, N. J. *Nature Chemistry* **2009**, *1*, 635.
- (128) Chen, F.; Tao, N. J. *Accounts Chem Res* **2009**, *42*, 429.
- (129) Parameswaran, R.; Widawsky, J. R.; Vazquez, H.; Park, Y. S.; Boardman, B. M.; Nuckolls, C.; Steigerwald, M. L.; Hybertsen, M. S.; Venkataraman, L. *J Phys Chem Lett* **2010**, *1*, 2114.
- (130) Schneebeli, S.; Kamenetska, M.; Foss, F.; Vazquez, H.; Skouta, R.; Hybertsen, M.; Venkataraman, L.; Breslow, R. *Org Lett* **2010**, *12*, 4114.
- (131) Mishchenko, A.; Vonlanthen, D.; Meded, V.; Burkle, M.; Li, C.; Pobelov, I. V.; Bagrets, A.; Viljas, J. K.; Pauly, F.; Evers, F.; Mayor, M.; Wandlowski, T. *Nano Lett* **2010**, *10*, 156.
- (132) Cheng, Z. L.; Skouta, R.; Vazquez, H.; Widawsky, J. R.; Schneebeli, S.; Chen, W.; Hybertsen, M. S.; Breslow, R.; Venkataraman, L. *Nat Nanotechnol* **2011**.
- (133) Sacha, G. M.; Sahagun, E.; Saenz, J. J. *J Appl Phys* **2007**, *101*.
- (134) Joachim, C.; Ratner, M. A. *Proceedings of the National Academy of Sciences of the United States of America* **2005**, *102*, 8801.
- (135) Reichert, J.; Ochs, R.; Beckmann, D.; Weber, H. B.; Mayor, M.; von Lohneysen, H. *Phys. Rev. Lett.* **2002**, *88*, 176804.
- (136) Xu, B. Q.; Tao, N. J. J. *Science* **2003**, *301*, 1221.
- (137) Venkataraman, L.; Klare, J. E.; Nuckolls, C.; Hybertsen, M. S.; Steigerwald, M. L. *Nature* **2006**, *442*, 904.

- (138) Baheti, K.; Malen, J. A.; Doak, P.; Reddy, P.; Jang, S. Y.; Tilley, T. D.; Majumdar, A.; Segalman, R. A. *Nano Lett.* **2008**, *8*, 715.
- (139) Reddy, P.; Jang, S. Y.; Segalman, R. A.; Majumdar, A. *Science* **2007**, *315*, 1568.
- (140) Grandbois, M.; Beyer, M.; Rief, M.; Clausen-Schaumann, H.; Gaub, H. E. *Science* **1999**, *283*, 1727.
- (141) Xu, B. Q.; Xiao, X. Y.; Tao, N. J. *J. Am. Chem. Soc.* **2003**, *125*, 16164.
- (142) Venkataraman, L.; Klare, J. E.; Tam, I. W.; Nuckolls, C.; Hybertsen, M. S.; Steigerwald, M. L. *Nano Lett.* **2006**, *6*, 458
- (143) Park, Y. S.; Whalley, A. C.; Kamenetska, M.; Steigerwald, M. L.; Hybertsen, M. S.; Nuckolls, C.; Venkataraman, L. *J. Am. Chem. Soc.* **2007**, *129*, 15768.
- (144) Kamenetska, M.; Koentopp, M.; Whalley, A.; Park, Y. S.; Steigerwald, M.; Nuckolls, C.; Hybertsen, M.; Venkataraman, L. *Phys. Rev. Lett.* **2009**, *102*, 126803.
- (145) Paulsson, M.; Krag, C.; Frederiksen, T.; Brandbyge, M. *Nano Lett.* **2009**, *9*, 117.
- (146) Qi, Y. H.; Qin, J. Y.; Zhang, G. L.; Zhang, T. *J. Am. Chem. Soc.* **2009**, *131*, 16418.
- (147) Kresse, G.; Furthmuller, J. *Phys. Rev. B* **1996**, *54*, 11169.
- (148) Kresse, G.; Joubert, D. *Phys. Rev. B* **1999**, *59*, 1758.
- (149) Blochl, P. E. *Phys. Rev. B* **1994**, *50*, 17953.
- (150) Perdew, J. P.; Burke, K.; Ernzerhof, M. *Phys. Rev. Lett.* **1996**, *77*, 3865.
- (151) Lambropoulos, N. A.; Reimers, J. R.; Hush, N. S. *J. Chem. Phys.* **2002**, *116*, 10277.
- (152) Bilic, A.; Reimers, J. R.; Hush, N. S. *J. Chem. Phys.* **2005**, *122*, 094708.
- (153) Bilic, A.; Reimers, J. R.; Hush, N. S. *J. Phys. Chem. B* **2002**, *106*, 6740.
- (154) Stadler, R.; Thygesen, K. S.; Jacobsen, K. W. *Phys. Rev. B* **2005**, *72*, 241401.
- (155) Blyholder, G. *J. Phys. Chem.* **1964**, *68*, 2772.
- (156) Gajdos, M.; Eichler, A.; Hafner, J. *Journal of Physics-Condensed Matter* **2004**, *16*, 1141.
- (157) Kamenetska, M.; Quek, S. Y.; Whalley, A. C.; Steigerwald, M. L.; Choi, H. J.; Louie, S. G.; Nuckolls, C.; Hybertsen, M. S.; Neaton, J. B.; Venkataraman, L. *J. Am. Chem. Soc.* **2010**, *132*, 6817.

- (158) Frei, M.; Aradhya, S. V.; Koentopp, M.; Hybertsen, M. S.; Venkataraman, L. *Nano Lett.* **2011**, *11*, 1518.
- (159) Parameswaran, R.; Widawsky, J. R.; Vazquez, H.; Park, Y. S.; Boardman, B. M.; Nuckolls, C.; Steigerwald, M. L.; Hybertsen, M. S.; Venkataraman, L. *J. Phys. Chem. Lett.* **2010**, *1*, 2114.
- (160) Rubio-Bollinger, G.; Bahn, S. R.; Agrait, N.; Jacobsen, K. W.; Vieira, S. *Phys. Rev. Lett.* **2001**, *87*, 026101.
- (161) Tavazza, F.; Levine, L. E.; Chaka, A. M. *J. App. Phys.* **2009**, *106*, 043522.
- (162) Ulrich, J.; Esrail, D.; Pontius, W.; Venkataraman, L.; Millar, D.; Doerrer, L. H. *J. Phys. Chem. B* **2006**, *110*, 2462.
- (163) Arroyo, C. R.; Leary, E.; Castellanos-Gómez, A. s.; Rubio-Bollinger, G.; González, M. T.; Agrait, N. s. *J. Am. Chem. Soc.* **2011**, *133*, 14313.
- (164) Basch, H.; Cohen, R.; Ratner, M. A. *Nano Lett.* **2005**, *5*, 1668.
- (165) Hu, Y.; Zhu, Y.; Gao, H.; Guo, H. *Phys Rev Lett* **2005**, *95*, 156803.
- (166) Kruger, D.; Fuchs, H.; Rousseau, R.; Marx, D.; Parrinello, M. *Phys. Rev. Lett.* **2002**, *89*, 186402.
- (167) Paulsson, M.; Krag, C.; Frederiksen, T.; Brandbyge, M. *Nano Lett.* **2008**, *9*, 117.
- (168) Qi, Y.; Qin, J.; Zhang, G.; Zhang, T. *J Am Chem Soc* **2009**, *131*, 16418.
- (169) Li, Z. L.; Zhang, G. P.; Wang, C. K. *J Phys Chem C* **2011**, *115*, 15586.
- (170) Krans, J. M.; Muller, C. J.; Yanson, I. K.; Govaert, T. C. M.; Hesper, R.; Vanruitenbeek, J. M. *Phys Rev B* **1993**, *48*, 14721.
- (171) Krans, J. M.; van Ruitenbeek, J. M.; Fisun, V. V.; Yanson, I. K.; de Jongh, L. J. *Nature* **1995**, *375*, 767.
- (172) Scheer, E.; Agrait, N.; Cuevas, J. C.; Yeyati, A. L.; Ludoph, B.; Martin-Rodero, A.; Bollinger, G. R.; van Ruitenbeek, J. M.; Urbina, C. *Nature* **1998**, *394*, 154.
- (173) Bahn, S. R.; Jacobsen, K. W. *Phys Rev Lett* **2001**, *87*.
- (174) Oshima, H.; Miyano, K. *Applied Physics Letters* **1998**, *73*, 2203.
- (175) Ludoph, B.; van der Post, N.; Bratus', E. N.; Bezuglyi, E. V.; Shumeiko, V. S.; Wendin, G.; van Ruitenbeek, J. M. *Phys Rev B* **2000**, *61*, 8561.
- (176) Costa-Krämer, J. L. *Phys Rev B* **1997**, *55*, R4875.
- (177) Muller, C. J.; Krans, J. M.; Todorov, T. N.; Reed, M. A. *Phys Rev B* **1996**, *53*, 1022.

- (178) Shu, C.; Li, C. Z.; He, H. X.; Bogozi, A.; Bunch, J. S.; Tao, N. J. *Phys Rev Lett* **2000**, *84*, 5196.
- (179) Costa-Krämer, J. L.; García, N.; García-Mochales, P.; Serena, P. A.; Marqués, M. I.; Correia, A. *Phys Rev B* **1997**, *55*, 5416.
- (180) Rodrigues, V.; Bettini, J.; Rocha, A. R.; Rego, L. G. C.; Ugarte, D. *Phys Rev B* **2002**, *65*.
- (181) Smit, R. H. M.; Untiedt, C.; Yanson, A. I.; van Ruitenbeek, J. M. *Phys Rev Lett* **2001**, *87*, 266102.
- (182) Ludoph, B.; Ruitenbeek, J. M. v. *Phys Rev B* **2000**, *61*, 2273.
- (183) Kaneko, S.; Nakazumi, T.; Kiguchi, M. *J Phys Chem Lett* **2010**, *1*, 3520.
- (184) Hansen, K.; Lægsgaard, E.; Stensgaard, I.; Besenbacher, F. *Phys Rev B* **1997**, *56*, 2208.
- (185) Ko, C.-H.; Huang, M.-J.; Fu, M.-D.; Chen, C.-h. *J Am Chem Soc* **2009**, *132*, 756.
- (186) Csonka, S.; Halbritter, A.; Mihály, G.; Shklyarevskii, O. I.; Speller, S.; van Kempen, H. *Phys Rev Lett* **2004**, *93*, 016802.
- (187) Matsuda, T.; Kizuka, T. *Japanese Journal of Applied Physics Part 1-Regular Papers Brief Communications & Review Papers* **2007**, *46*, 4370.
- (188) Kiguchi, M.; Murakoshi, K. *Applied Physics Letters* **2006**, *88*, 253112.
- (189) Zhou, X.-S.; Wei, Y.-M.; Liu, L.; Chen, Z.-B.; Tang, J.; Mao, B.-W. *J Am Chem Soc* **2008**, *130*, 13228.
- (190) Rodrigues, V.; Bettini, J.; Silva, P. C.; Ugarte, D. *Phys Rev Lett* **2003**, *91*, 096801.
- (191) den Boer, D.; Shklyarevskii, O. I.; Coenen, M. J. J.; van der Maas, M.; Peters, T. P. J.; Elemans, J. A. A. W.; Speller, S. *The Journal of Physical Chemistry C* **2011**, *115*, 8295.
- (192) Thijssen, W. H. A.; Marjenburgh, D.; Bremmer, R. H.; van Ruitenbeek, J. M. *Phys Rev Lett* **2006**, *96*, 026806.
- (193) Thijssen, W. H. A.; Strange, M.; Brugh, J. M. J. a. d.; Ruitenbeek, J. M. v. *New Journal of Physics* **2008**, *10*, 033005.
- (194) Strange, M.; Thygesen, K. S.; Sethna, J. P.; Jacobsen, K. W. *Phys Rev Lett* **2008**, *101*, 096804.
- (195) Çakır, D.; Gülseren, O. *Phys Rev B* **2011**, *84*, 085450.
- (196) Schmidt, M.; Cahuzac, P.; Brechignac, C.; Cheng, H.-P. *The Journal of Chemical Physics* **2003**, *118*, 10956.

- (197) Bonini, N.; Kokalj, A.; Dal Corso, A.; de Gironcoli, S.; Baroni, S. *Phys Rev B* **2004**, *69*, 195401.
- (198) Vattuone, L.; Burghaus, U.; Savio, L.; Rocca, M.; Costantini, G.; Mongeot, F. B. d.; Boragno, C.; Rusponi, S.; Valbusa, U. *The Journal of Chemical Physics* **2001**, *115*, 3346.
- (199) Zhou, J.; Li, Z.-H.; Wang, W.-N.; Fan, K.-N. *Chem Phys Lett* **2006**, *421*, 448.
- (200) Halbritter, A.; Makk, P.; Mackowiak, S.; Csonka, S.; Wawrzyniak, M.; Martinek, J. *Phys Rev Lett* **2010**, *105*.
- (201) Klavsyuk, A.; Kolesnikov, S.; Smelova, E.; Saletsky, A. *Jetp Lett+* **2010**, *91*, 158.
- (202) Enomoto, A.; Kurokawa, S.; Sakai, A. *Phys Rev B* **2002**, *65*.
- (203) Gemming, S.; Seifert, G.; Schreiber, M. *Phys Rev B* **2004**, *69*, 245410.
- (204) Enomoto, A.; Kurokawa, S.; Sakai, A. *Phys Rev B* **2002**, *65*, 125410.
- (205) Fujii, A.; Ochi, R.; Kurokawa, S.; Sakai, A. *Applied Surface Science* **2004**, *228*, 207.
- (206) Heemskerk, J. W. T.; Noat, Y.; Bakker, D. J.; van Ruitenbeek, J. M.; Thijssse, B. J.; Klaver, P. *Phys Rev B* **2003**, *67*, 115416.
- (207) Smith, D. T.; Pratt, J. R.; Howard, L. P. *Rev Sci Instrum* **2009**, *80*, 035105.